Technische Universität München
Fakultät für Physik

Investigation of MHD Instabilities in Conventional and Advanced Tokamak Scenarios on ASDEX Upgrade

Valentin Igochine

Vollständiger Abdruck der von der Fakultät für Physik
der Technischen Universität München
zur Erlangung des akademischen Grades eines
Doktors der Naturwissenschaften (Dr.rer.nat.)
genehmigten Dissertation.

Vorsitzender:	Univ.-Prof. Dr. R. L. Gross
Prüfer der Dissertation:	1. Hon.-Prof. Dr. R. Wilhelm
	2. Univ.-Prof. Dr. M. Lindner

Die Dissertation wurde am 7.10.2002 bei der
Technischen Universität München eingereicht und
durch die Fakultät für Physik am 6.12.2002 angenommen.

Abstract

A new combined method for an investigation of the MHD activities in fusion experiments has been developed. The main advantages of this approach are the simultaneous use of several diagnostics (magnetic probes, soft X-ray cameras, electron cyclotron emission and motional Stark effect diagnostics) and the possibility for a direct comparison of theory predictions with the experimental observations. This method has been implemented into the MHD Interpretation Code (MHD-IC) and allows to investigate complicated mode structures which are not resolved by the available tools (tomography etc.). The code simulates experimental observations related to a given plasma perturbation for the diagnostics mentioned above, accounting for real plasma geometry and for measured plasma parameters. Then the calculated values are compared with the corresponding experimental data. The method has been successfully applied to different types of MHD instabilities on ASDEX Upgrade.

For example, the investigation of fishbone activities in the conventional scenario shows that the displacement eigenfunction is an ideal $(1,1)$ kink mode which get a resistive character for $\beta_N \geqslant 1.8$.

The main analysis efforts however were focused on more demanding examples due to the more complicated mode structure in advanced tokamak scenarios. As an example, in this case the displacement eigenfunction for double tearing modes (DTM) was obtained using MHD-IC code. The growth rate of the DTM calculated from the displacement eigenfunction agrees well with numerical MHD simulations and the experiment. The time evolution of a MHD instabilities which accompanies the formation of internal transport barriers was investigated as well. It shows the behavior of two coupled $(2,1)$ modes. Furthermore, the MHD activity causing a disruption was investigated in typical reversed shear discharges on ASDEX Upgrade. The main reason for the disruptions is an external mode or an internal $(3,1)$ tearing mode.

In addition, the structure and the position of the observed MHD phenomena are applied to improve the equilibrium reconstruction. This betterment is especially important in the plasma core region where the large error bars of the MSE measurements do not allow for an accurate determination of the q-profile.

Contents

Chapter 1

Introduction

1.1 General Introduction

The controlled nuclear fusion of deuterium (D) and tritium (T) atoms in a plasma promises an almost inexhaustible source of energy. It will also ensure higher environmental safety compared to nuclear fission. When the $D-T$ plasma is heated to thermonuclear conditions, an "ignition" can be maintained in the plasma (when the fusion born particles provide enough heat to compensate for the heat losses). However, even for this most favorable fusion reaction

$$D + T \rightarrow^4 He\,(3.5MeV) + n\,(14.1MeV)\,, \tag{1.1}$$

this plasma must be heated to a very high temperature $T \sim 20keV$ (230 million K) and must be confined for a long enough time to satisfy the Lawson criterion [1]:

$$n\tau_{E\_conf} \gtrsim 1.5 \cdot 10^{20} m^{-3} s\ , \tag{1.2}$$

where τ_{E_conf} determines the energy confinement time (the ratio of the energy stored in the plasma to the heat loss rate), and n is the plasma density.

In the future, further increasing of the plasma parameters might even give the opportunity to achieve necessary conditions for more preferable $D-D$ and $D-^3He$ reactions, which would be characterized by very small neutron flux and avoid many problems with tritium handling.

During last fifty years many different approaches were investigated in order to maintain the thermonuclear reaction. Among them, the most advanced concept towards the achievement of the required fusion reactor parameters

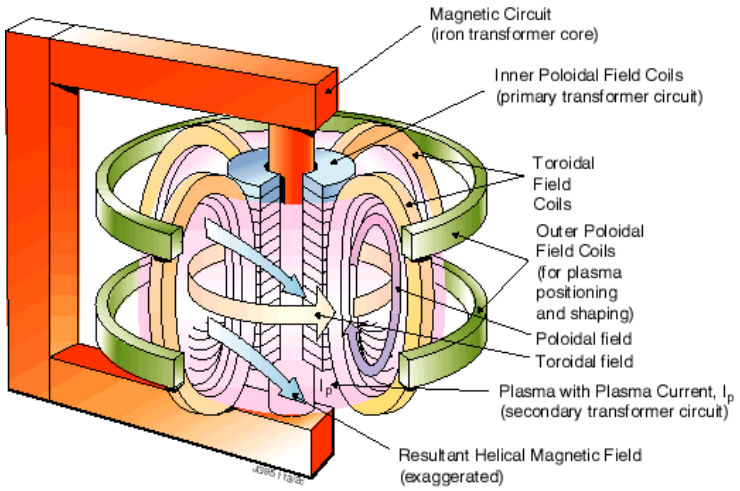

Figure 1.1: Principle scheme of a tokamak. The plasma is the second winding of the transformer. The plasma current is produced by induction.

is a so-called tokamak configuration[1]. This approach was proposed by the Russian physicists Tamm and Sakharov [2]. The tokamak is a toroidal system which confines the plasma by a magnetic field [3]. The main magnetic field is the toroidal field B_ϕ. However, this field alone does not allow the confinement of the plasma and an additional poloidal magnetic field B_θ is necessary for an equilibrium which has the plasma pressure balanced by the magnetic forces. This additional field is produced by a large toroidal current in the plasma and by outer poloidal field coils (see Fig.1.1). The combination of the toroidal field B_ϕ and the poloidal field B_θ results in magnetic field lines with helical trajectories around the torus lying on so-called magnetic surfaces. That way, the hot charged particles are confined and cannot travel in radial direction along magnetic field lines. An external energy source generates initial current in the primary winding of a transformer and the toroidal plasma current is produced by induction. Thus, the plasma itself is the secondary winding of the transformer (see Fig.1.1). As an example, the cross-section of the ASDEX Upgrade tokamak is shown in Fig.1.2[2]. A lot of additional magnetic coils help to variate shape of the plasma and to control

[1] From the Russian toroidalnaia kamera s magnitnoi katushkoi (toroidal chamber with magnetic coils)

[2] Main plasma parameters of the ASDEX Upgrade tokamak are given in appendix A.

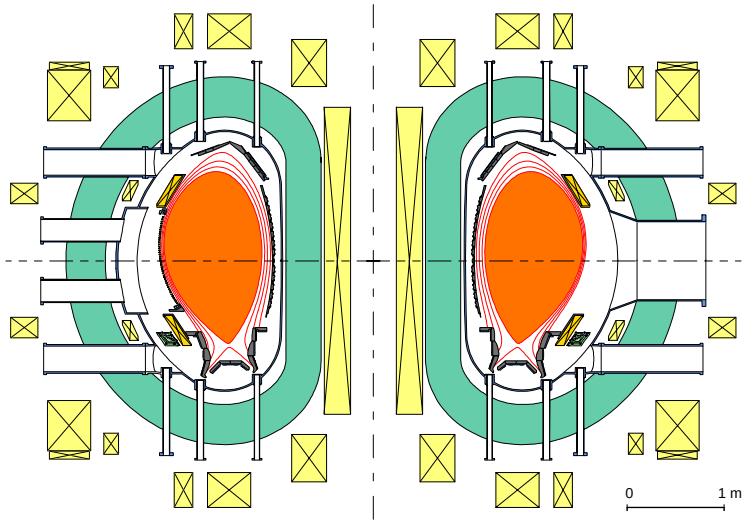

Figure 1.2: Cross-section of ASDEX Upgrade tokamak.

its behaviour during tokamak operations.

At the beginning of a discharge the tokamak plasma is heated by ohmic dissipation of the plasma current but this heat is not enough for the typical fusion parameters described above. Thus, additional heating schemes such as the injection of high energy neutral beams or launching electromagnetic waves into the plasma are applied in fusion experiments [3]. Once ignited the nuclear reaction in the plasma would be completely self-heating through the fusion-born α-particles[3].

Unfortunately, different types of instabilities appear in the plasma. These instabilities strongly reduce plasma parameters and may even lead to disruption (dramatic event in which the plasma confinement is suddenly destroyed). The investigation of the instabilities is therefore of crucial importance and will be the subject of this thesis.

[3]Nuclei of ^4He atom with energy $3.52MeV$

1.2 Magneto-hydro-dynamics

A magnetically confined plasma can be described as a conductive fluid. The typical fluid approximation is based on the assumption that the system is locally close to the thermodynamic equilibrium, which requires a certain rate of collisions and dissipation. For that case, the mean free path λ should be shorter compared with typical gradient scales, $\lambda \left| \bigtriangledown f \right| \ll f$ [4]. The mean free path in hot plasmas becomes very long, but at the same time in a magnetized plasma gradients parallel to the fields are getting very weak, and the fluid description can be applied. For perpendicular directions, the mean free path is about the gyroradius ρ ($\rho = v_\perp/\omega_c$, where ω_c is the cyclotron frequency and $v_\perp$ is the thermal velocity perpendicular to the magnetic field), which is typically very small and the condition is also fulfilled. Consequently, the fluid description can be applied to the plasma.

Magneto-hydro-dynamics (MHD) implies magnetic fluid dynamics and applies to investigate macroscopic dynamics of the plasma. It is a model system designed to deal with an electrically neutral fluid which nevertheless consists of moving charged particles, and reacts to magnetic fields. The MHD model is a combination of Maxwell's equations with the equations of gas dynamics and equations describing the interaction of the conductive fluid with the magnetic fields (Newton's equation of motion for a fluid element).

The result system of the resistive MHD equations together with the adiabatic equation [4, 5]:

$$\frac{d\rho}{dt} = -\rho\vec{\nabla}\cdot\vec{v} \qquad \text{(mass conservation)} \tag{1.3}$$

$$\rho\frac{d\vec{v}}{dt} = \vec{j}\times\vec{B} - \nabla p \qquad \text{(momentum equation)} \tag{1.4}$$

$$\vec{j} = \vec{\nabla}\times\vec{B}/\mu_0 \qquad \text{(Ampere's law)} \tag{1.5}$$

$$\frac{\partial\vec{B}}{\partial t} = -\vec{\nabla}\times\vec{E} \qquad \text{(Faraday's law)} \tag{1.6}$$

$$\vec{E} + \vec{v}\times\vec{B} = \eta\vec{j} \qquad \text{(Ohm's law)} \tag{1.7}$$

$$\vec{\nabla}\cdot\vec{B} = 0 \qquad \text{(absence of magnetic charges)} \tag{1.8}$$

$$\frac{dp}{dt} = -\gamma p\vec{\nabla}\cdot\vec{v} \qquad \text{(adiabatic equation)} \tag{1.9}$$

These equations are solved to investigate a plasma equilibrium and the stability of this equilibrium to perturbations. A possible way is to solve these equations directly and this possibility is for example implemented in the XTOR code [6, 7]. Another approach is a linear analysis which simplifies these equations by the assumption of a perturbation to be much smaller compared to the corresponding equilibrium quantity (e.g., CASTOR code[4]).

1.3 Energy principle

Besides solving the Eqs.(1.3 - 1.8) directly, another useful approach for a stability analysis is the energy principle. The energy principle of ideal MHD is based on the idea that an equilibrium is unstable if any perturbation of the equilibrium lowers the potential energy. It describes so-called *ideal modes* (*resistive modes* appear when the resistivity η becomes important in the equations). The potential energy change due to an arbitrary displacement $\vec{\xi}$ can be calculated using Eqs.(1.3 - 1.8) and the linear approximation [3, 8].

The force arising from the displacement $\vec{\xi}$ follows from the momentum equation:

$$\vec{F}\left(\vec{\xi}\right) = \rho\frac{\partial^2\vec{\xi}}{\partial t^2} = \vec{j}_1 \times \vec{B}_0 + \vec{j}_0 \times \vec{B}_1 - \nabla p_1.$$

Consequently, the energy change resulting from this displacement $\vec{\xi}(x)$ of the plasma is given by the integral

$$\begin{aligned} \delta W &= -\frac{1}{2}\int \vec{\xi}\cdot\vec{F}d\tau \qquad (1.10)\\ \delta W &< 0 \quad (unstable)\\ \delta W &> 0 \quad (stable) \end{aligned}$$

The plasma is *unstable* if δW is negative for any physically allowed $\vec{\xi}$, and the plasma is *stable* if δW is positive for all allowed $\vec{\xi}$.

Rewrite the equation (1.10) into a more convenient form with separated plasma and vacuum parts leads to [3]:

$$\delta W = \delta W_{vacuum} + \delta W_{plasma} \qquad (1.11)$$

$$\delta W_{vacuum} = \int_v ({B_v}^2/2\mu_0)d\tau \qquad (1.12)$$

[4]Brief description of these codes is done in Appendix C.

$$\delta W_{plasma} = \frac{1}{2}\int_{pl}(\gamma p_0(\vec{\nabla}\cdot\vec{\xi})^2 + \underline{(\vec{\xi}\cdot\nabla p_0)\vec{\nabla}\cdot\vec{\xi}} + \frac{{B_1}^2}{\mu_0} - \underline{\vec{j_0}\cdot(\vec{B_1}\times\vec{\xi})})d\tau \ , \quad (1.13)$$

where B_v is the vacuum magnetic field and the indexes (0/1) describe the equilibrium and the perturbed quantities respectively. There are only two terms which can be negative. These terms are underlined in Eq.1.13. Consequently, there are two different sources of the instabilities: one proportional to ∇p_0 and the other to j_0. The MHD instabilities in which the dominant destabilizing term is proportional to ∇p_0 are known as *pressure-driven modes*. The dominant driving source of a *current-driven mode* is proportional to j_0.

1.4 Two important parameters in MHD stability: q, β

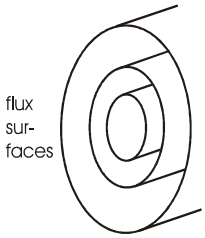

In a tokamak equilibrium the magnetic force balances the plasma pressure: $\vec{j}\times\vec{B} = \nabla p$, and this requirement constructs a set of nested magnetic surfaces on which $\vec{j}$ and $\vec{B}$ are constant. Each of these surfaces can be characterized by its own value of the magnetic flux and called flux surface [9, 10].

Using these surfaces we can introduce the *safety factor* q. This name is because of the role it plays in determining the stability. In general terms, greater stability corresponds to higher values of q. In an equilibrium configuration each magnetic field line has a value of q and follows a helical path around the torus on its own magnetic surface. The definition of the q-value for a field line is following:

$$q = \frac{\Delta\phi}{2\pi} \ ,$$

where $\Delta\phi$ is the toroidal angle at which the field line returns to the same position in the poloidal plane [3]. For instance, the "safety factor" equals to one corresponds to a magnetic surface with field lines joining up on itself after exactly one rotation around the torus. Magnetic surfaces with rational values of q are very important in stability analysis. If the field line joins up on itself exactly after n toroidal and m poloidal rotations around the torus, the safety factor reads

$$q = \frac{m}{n} \ , \quad (1.14)$$

where n and m are integers, perturbations are easily excited on these surfaces since the field lines do not cover these surfaces ergodically. These flux surfaces are called *resonant surfaces* and a standing wave with mode numbers (m, n) can occur.

Another parameter which has to be introduced is the plasma parameter β, which is defined by

$$\beta \equiv \frac{p}{B^2/2\mu_0} = \frac{\text{plasma pressure}}{\text{magnetic field pressure}} \ .$$

It is a measure of stability against pressure driven modes for a given magnetic field strength and also shows the efficiency of confinement of plasma pressure by the magnetic field [11].

1.5 Characteristics of MHD activities

MHD instabilities play two different roles in fusion experiments. On the one hand, their influence is negative and they limit the accessible operating regime and restrict the fusion output and minimum power plant size. On the other hand, these instabilities can be used to achieve quasistationary discharge conditions. For instance, they can limit the impurity accumulation in the plasma.

An MHD instability is characterized by:

- mode numbers (m, n)
- mode frequency (ω), growth rate (γ)
- radial structure of the eigenfunction (ξ)

The poloidal (m) and the toroidal (n) mode numbers determine the helicity of the instability. The frequency of the mode (ω) represents the rotation frequency of the instability. Growth and decay of the instability are characterized by the growth rate parameter (γ). The displacement eigenfunction (ξ) represents the shift of the magnetic field lines due to the MHD mode. This displacement depends on the type of the instability and varies across the plasma radius.

The MHD activities in tokamak usually have a helical structure around the torus as it is shown for a tearing mode in Fig.1.3 [12]. In this example,

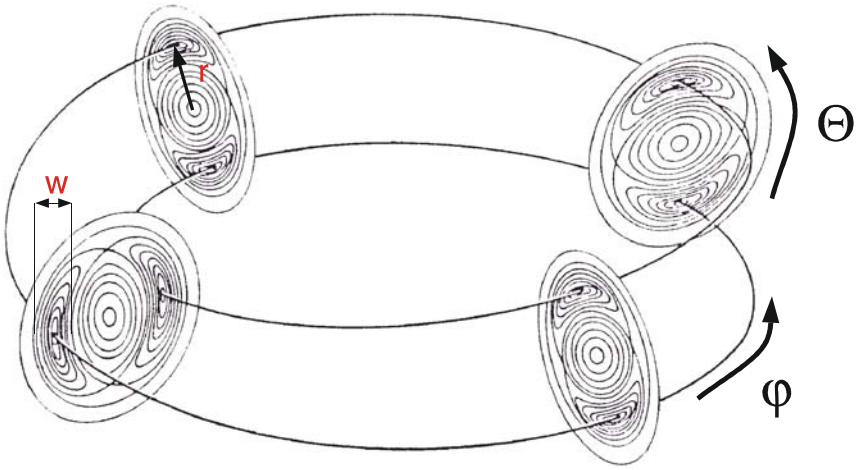

Figure 1.3: Example of a tearing mode spacial structure.

the finite resistivity of the plasma allows for the magnetic lines to reconnect and form islands. It is convenient to introduce for such type of instabilities an additional parameter: the island width (W). It describes the maximum width of the island structure.

To demonstrate different forms of MHD instabilities, the field perturbation due to a tearing mode and an ideal kink mode are shown in Fig.1.4 together with the radial component of the displacement eigenfunctions. It becomes obvious that for a resistive mode the island width W is simply the distance between the minimum and maximum value of ξ_0. On the other hand, the internal kink ($m = 1, n = 1$) mode is characterized by a rigid shift of the plasma inside the $q = 1$ surface and does not form an island. The displacement ξ_0 is a simple step function in this case. These two modes represent typical resistive (tearing mode) and ideal (kink mode) types of MHD activity. *Characteristic for a resistive instability is the change in sign of the displacement ξ_0, in contrast to an ideal instability.* Besides the different displacement eigenfunctions, resistive and ideal instabilities differ, e.g. in driving forces and growth times.

Using various diagnostics, all the above mentioned information characterizing an MHD instability can be gained. For instance, a tearing mode has a constant temperature inside the island which is observable by the temperature profile measurements. Due to the plasma rotation in the tokamak, the

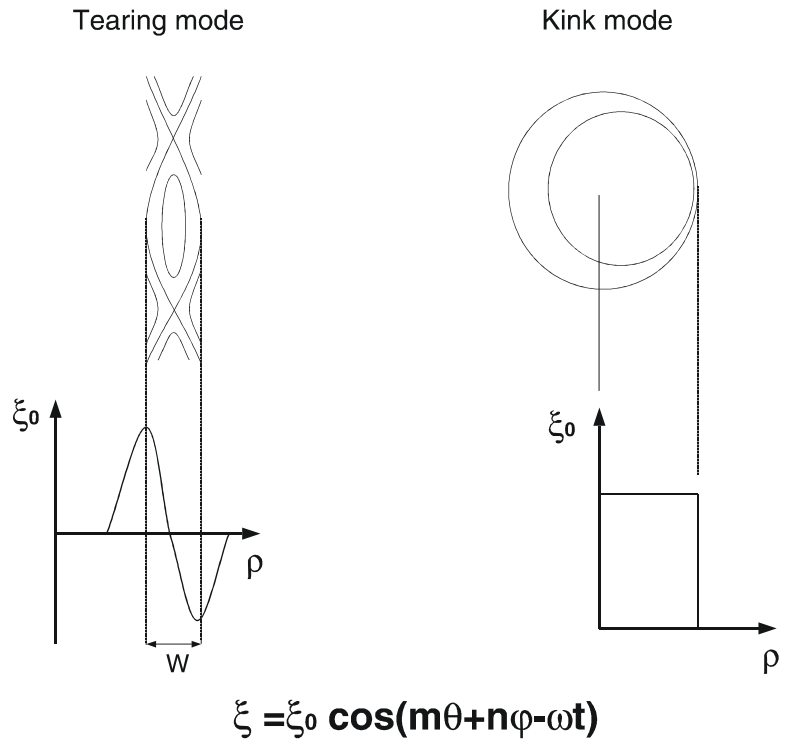

Figure 1.4: Examples of MHD instabilities. Sketch of the magnetic field surfaces in the vicinity of the resonant surface together with displacement eigenfunction for a tearing mode (left) and for an ideal $(1, 1)$ kink mode (right).

tearing mode moves and produces variations of the magnetic field which also can be detected by magnetic probes.

1.6 The aim of the work

As was mentioned above, the main aim of the fusion experiments is the plasma confinement which is strongly restricted by various MHD instabilities. For example, island formation in the plasma creates a heat bridge (since across the island temperature is constant), which leads to heat flow from the plasma center. This cooling process reduces the confinement and may even lead to disruption when the island becomes large. The kink mode, described in the previous section, may reduce β-value by ejection of fast ions from the plasma core. The external kink mode characterized by a large displacement on the plasma boundary also may lead to disruption. There is a wide variety of plasma instabilities which have different influence on the plasma. In order to obtain a good plasma confinement some of these instabilities should be avoided, the others can be controlled. Thus, it is of special importance to understand the reason for their appearence. This can be gained either directly from the spartial structure and time behavior of the instability or from a comparison of the mode structure with theory. As will be shown later, the MHD instabilities may have a rather complicated structure. The main aim of this work is to investigate these instabilities.

Unfortunately, the available tools (tomographic reconstruction etc.) often cannot resolve the mode structure, especially in complicated cases which frequently appear in advanced tokamak scenario. Thus, a new approach is required. For that purpose a method for a combined use of different experimental observations has been developed and implemented in a computational code. This method allows to handle these complicated cases. The code also provides a direct link between theory and experiment by simulating both, the experimental observable signals following from a given eigenfunction and vice versa, constructing an eigenfunction from different experimental diagnostics. This method was applied to investigate a wide range of plasma instabilities in advanced and conventional tokamak scenarios in ASDEX Upgrade tokamak.

This work is organized as follows. We begin with a brief overview of the diagnostic tools related to the identification of MHD activities (chapter 2), and describe then the applied methods of MHD analysis and modeling (chapter 3). After that, examples of investigations of MHD instabilities in

conventional and advanced tokamak scenarios on ASDEX Upgrade are given (chapters 4-6). At the end of this work we demonstrate additional benefits, which one can gain from the MHD analysis for the equilibrium reconstruction (chapter 7).

Chapter 2

Diagnostic tools for MHD activities

A variety of diagnostics is used in plasma physics to measure temperature, density, current profiles and other plasma parameters. Some of these methods can give information about plasma instabilities. This work will focus on four diagnostics, and especially on their simultaneous use to gain detailed information about the observed MHD instabilities. These are: magnetic measurements (Mirnov coils), soft X-ray cameras (SXR), electron cyclotron emission (ECE) and motional Stark effect (MSE). The ASDEX Upgrade tokamak is equipped with all of these diagnostics.

2.1 Magnetic measurements

From the beginning of tokamak researches small magnetic coils (Mirnov coils) have been widely used as a diagnostic method [13, 14, 15]. On ASDEX Upgrade the magnetic measurements consist of a set of 32 poloidal and 10 toroidal Mirnov coils to register $\dot{B}_\theta$ [16], and a set of poloidal and toroidal ballooning coils to detect $\dot{B}_R$. Using these coils, plasma perturbations can be detected at the plasma edge even if their amplitude is quite small. Experimental observations show that the modes usually rotate in poloidal direction with time scales 10^3 times shorter than typical time scales for changes in the equilibrium magnetic field. Magnetic coils detect the time derivative of $\vec{B}$ and therefore the instabilities can be registered even when their magnetic perturbations are only 10^{-3} of the equilibrium magnetic field.

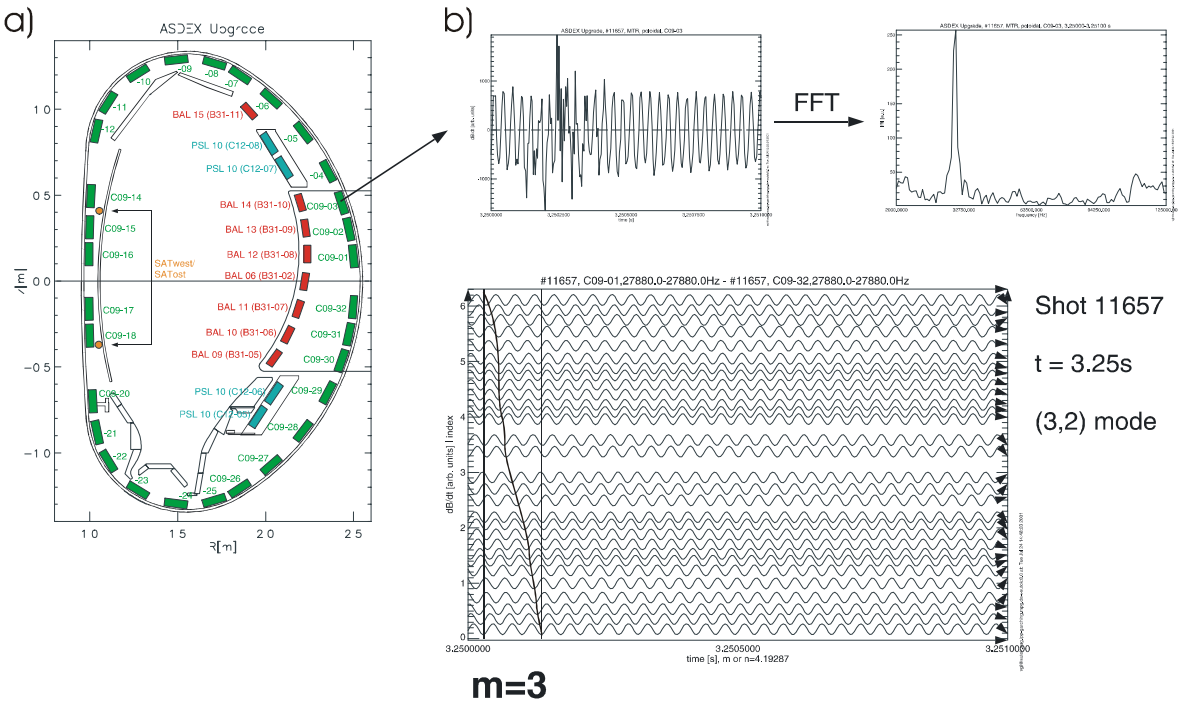

Figure 2.1: Determination of the poloidal mode number from the magnetic measurements. The raw data are analyzed with a fast Fourier transform. To extract the dominant mode number, the field perturbation due to the mode with the dominant frequency is plotted. Following the poloidal direction for a time point, one can find three maximums of the magnetic signal. (Number of the periods corresponds to the number of maximums for a time point.) Each maximum matches to an island. Consequently, poloidal mode number is the number of the periods ($m = 3$).

By making measurements at different poloidal and toroidal locations the structure of magnetic perturbations (m, n) can be determined as well as their amplitudes and frequencies. These measurements are routinely used on ASDEX Upgrade for identification of the poloidal and toroidal mode numbers and the frequencies of MHD modes.

The location of the magnetic coils on ASDEX Upgrade in a poloidal cross-section is shown in Fig.2.1a. Fig.2.1b shows the usual analysis of the Mirnov measurements. The raw experimental data are analyzed with a Fast Fourier Transform (FFT). In many cases the spectral function shows only one dominant frequency. In order to find the dominate mode number, the field perturbation due to the mode with the dominant frequency is plotted, and the points of equal phase are connected each other (see Fig.2.1b). Following the poloidal direction for a time point, one can find three maxima of the magnetic signal. The poloidal mode number is simply the number of these maxima (or the number of the periods). In the example of Fig.2.1 it is a $m = 3$ mode. The same algorithm is applied to determine the toroidal mode number from the toroidal set of coils.

From magnetic measurements detected outside the plasma alone however neither the position of the mode nor the spatial mode structure can be resolved [17]. Even more difficult is the investigation of coupled modes, resonant at different magnetic surfaces. Magnetic perturbations fall off with distance as $B \sim r^{-(m+1)}$, where m is the poloidal mode number. Thus, a perturbation located in the plasma center has much smaller amplitude compared to a perturbation near the plasma edge. In case of two modes with the same helicity being resonant on different radii, no information about the inner mode can be gained from magnetic measurements at all, as its magnetic perturbation is completely screened by the outer resonant surface. Therefore, additional diagnostics are required for a detailed investigation of MHD activities.

2.2 Soft X-ray radiation

The soft X-ray radiation (SXR)[1] emitted by the plasma is a very good tool to study MHD activities in the plasma core [18]. ASDEX Upgrade is equipped

[1]The radiation between $100eV$ and $10keV$ is called Soft X-ray radiation (SXR). On the high-energy side it has X-ray radiation (between $1keV$ to $100keV$). On the low-energy side it is bordered by vacuum ultraviolet radiation (between $6eV$ and $1keV$).

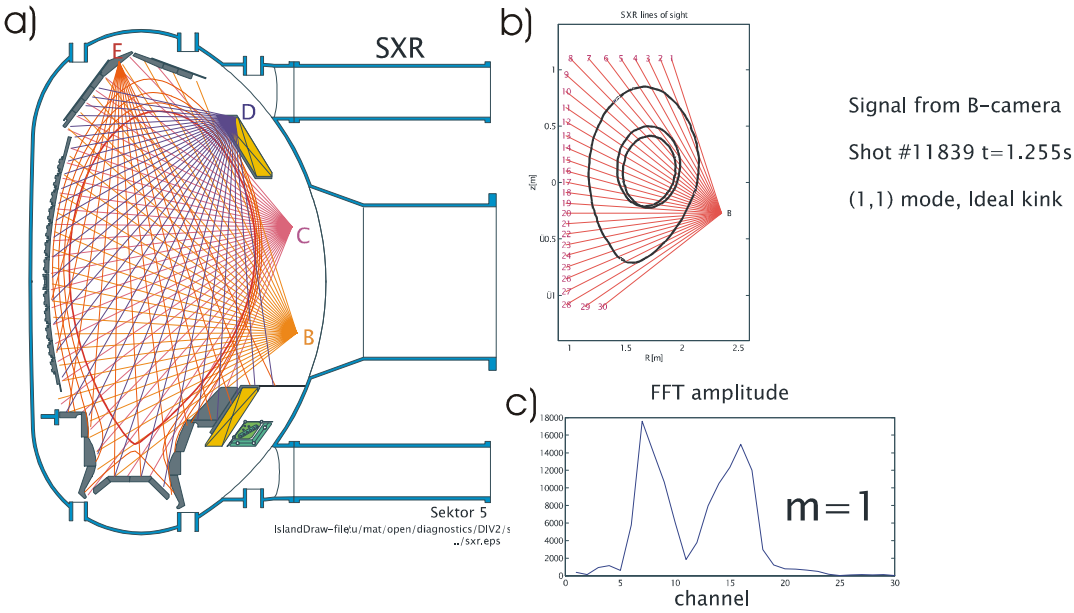

Figure 2.2: Position of the SXR cameras on ASDEX Upgrade (a). Determination of the poloidal mode number. The B-camera lines of sights of ASDEX Upgrade are plotted together with an ideal kink mode structure and the plasma boundary (b). The FFT transformation is applied to the raw data from the B-camera. In this case, the spectral function has only one dominant frequency, and the FFT amplitude for this frequency has one global minimum. This minimum indicates an $m = 1$ structure.

with five pinhole SXR cameras with 124 chords [19]. The positions of the cameras B, C, D, and F on ASDEX Upgrade are shown in Fig.2.2a. These lines of sight cover the whole plasma volume. This diagnostic provides information about the poloidal mode numbers, the mode frequency, and allows to perform a tomographic reconstruction [20, 21].

It should be mentioned, however, that the tomographic reconstruction using the SXR data has some limits and cannot always give a picture of the plasma instabilities with sufficient quality. For the investigation of complex mode structures (high poloidal mode number, coupled mode activity) the spatial resolution can be too poor due to the low number of detectors[2].

[2]Restricted space limits the number of the detectors. For instance, in the medical

By using SXR signals from one of the cameras, the poloidal mode number can be determined. An example of this analysis is shown in Fig.2.2. In Fig.2.2b the B-camera lines of sights are plotted together with an ideal kink mode structure and the plasma boundary. The FFT transformation is applied to the raw data. In our case, the spectral function has only one dominant frequency and the FFT amplitude for this frequency has one global minimum (Fig.2.2c). This minimum indicates an $m = 1$ structure. In the same way, two global minima correspond to $m = 2$, and so on. Unfortunately, this simple analysis does not work in case of several modes activity or more complicated mode structures. A more detailed analysis is required in this case.

2.3 Electron cyclotron emission

As was described before, plasma confinement in tokamaks is ensured by magnetic fields. Since the plasma consists of charge particles (electrons and ions), they gyrate around magnetic field lines. As a consequence of this motion electrons and ions emit electromagnetic radiation at the cyclotron resonance frequency $\omega_c = qB_{total}/m$, were B_{total} is the total magnetic field, q is the charge of a particle and m is the particle mass. This radiation emitted by electrons can be used to determine the electron temperature of the plasma with very high spatial and time resolution [23].

Under tokamak conditions, the plasma is usually optically thick for all frequencies resonant inside the plasma torus and practically all radiation is absorbed by the cyclotron resonance in a single pass of the wave through the plasma. In this case the plasma emits as a black-body radiator (Kirchhoff's law) and the radiation intensity is simply related to the electron temperature [3].

In a tokamak, the major field component is the toroidal field generated by external coils and depends on the major radius R as $B_{tor}(R) \sim 1/R$. Since the magnetic field is inhomogeneous, the spectral resolution of electron emission measurements translates into spatial resolution and outputs radial profiles of T_e along one radial line of sight. This radiometry of electron cyclotron emission (ECE) thus produces local measurements of the temperature inside the plasma which is advantageous compared to integral measurements by magnetic coils and SXR cameras.

tomography some 10^5 chords are available [22].

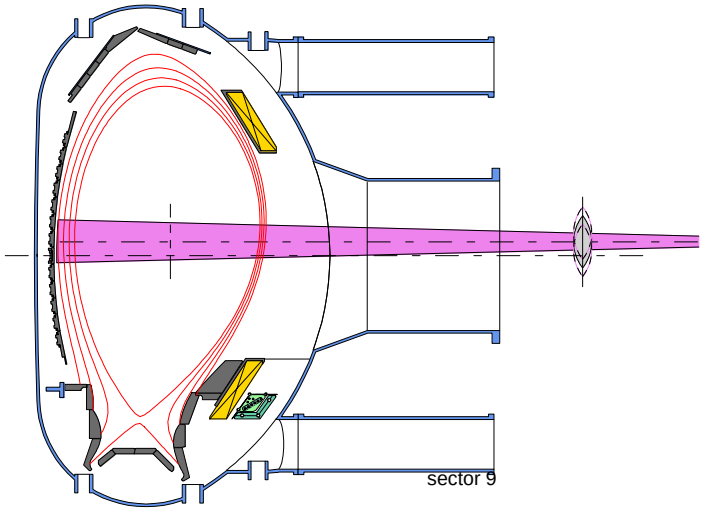

Figure 2.3: Position of the ECE diagnostic on ASDEX Upgrade tokamak.

Several different detectors are installed at ASDEX Upgrade to measure the ECE radiation. These detectors have different regions of applicability and different time resolution. Fast ECE channels give the electron temperature profile with high time resolution ($\Delta t \leqslant 32kHz$). It permits to measure changes in the electron temperature profile owing to the plasma instabilities. The cut-off density limit however restricts this method [24]. The lines of sight of the ECE diagnostic on ASDEX Upgrade is shown in Fig.2.3.

2.4 Motional Stark effect

The current profile in the plasma is determined by the Motional Stark Effect (MSE) diagnostic. This diagnostic is used to measure the local value of $\vec{B}$ and exploits the motional linear Stark effect. An injection beam of neutral hydrogen atoms is the base for this diagnostic. During injection of the atoms with velocity $\vec{v}$, an electric field in their own stationary frame given by the Lorentz field $\vec{E}_L = \vec{v} \times \vec{B}$ is appeared. This field splits spectral lines into π and σ components which is considerably larger than the Zeeman splitting in the magnetic field for this case [3]. From this splitting, it is possible to

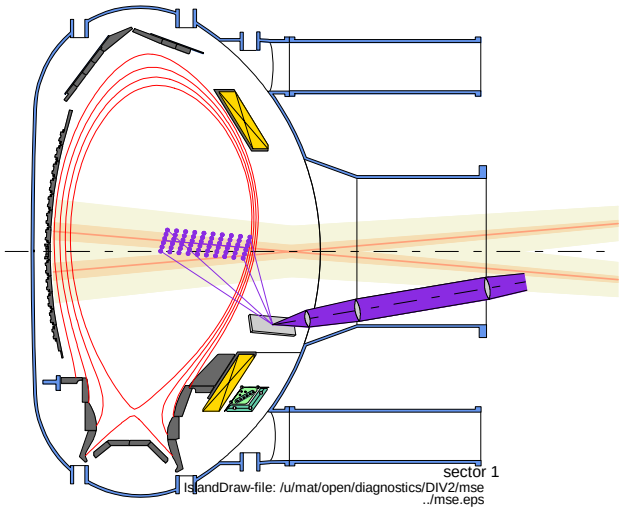

Figure 2.4: Position of the motional Stark effect diagnostic on the ASDEX Upgrade tokamak. The vertical lines show the positions of the measurement points.

identify the small poloidal component of the magnetic field and reconstruct the current profile inside the plasma.

The diagnostic on the ASDEX Upgrade tokamak has 10 spatial channels, covering about half of the plasma cross-section (see Fig.2.4) [25]. One of the $2.5MW$ heating beams is used for MSE measurements in the ASDEX Upgrade. The polarization direction of the σ-component of the Doppler-shifted and Stark-splitted deuterium Balmer-α beam emission is measured with a time resolution of $3ms$ [26]. Various calibration technique are used for this diagnostic and various effects, e.g. Faraday rotation should be taken into account (for the ASDEX Upgrade MSE diagnostic the Faraday rotation varies from 0.5 to $1.3deg/T$). These effects were included in the equilibrium reconstruction code CLISTE (CompLete Interpretive Suite for Tokamak Equilibria) allowing to determine an equilibrium with a reliable current profile [27, 28].

The equilibrium reconstruction based on the MSE measurements provides information on the location of the rational q values in the plasma. This information is limited however by the relatively large error bars especially

in the plasma center. The region of the MSE measurements on ASDEX Upgrade is approximately between $\rho_{tor} = 0.2$ and $\rho_{tor} = 0.8$.

2.5 Conclusions

The overview of the diagnostics shows that there is no universal tool for an investigation of the observed MHD instabilities. The diagnostics mentioned above give different information from different plasma regions and sometimes overlap each other. Since the existing tools are not sufficient to analyse the MHD instabilities in detail, a new approach is necessary. From this overview follows that an accumulation of all information from the diagnostics is the most natural way to increase our knowledge about the MHD activities.

On the other hand, a theoretical investigation of MHD activities provide additional information. As the complicated geometry excludes the use of simple theoretical models, complex computer codes have been developed. These codes are working for the real experimental geometry. They either start from a linearization of Eqs.(1.3 - 1.8) (e.g., the CASTOR code [29]) or even solve the full time dependent equations (e.g., the XTOR code [6, 7]). The results of these codes can be used for example to predict the form of displacement or the influence of these instabilities on the background plasma.

In the next chapter, we describe the new approach which has been developed to overcome these difficulties with investigation of complicated MHD structures. This approach accumulates experimental information from the diagnostics described above (Mirnov coils, SXR, ECE, MSE) and uses also information from computer simulations (XTOR, CASTOR). This allows to construct a link between the experimentally observed MHD instabilities and the corresponding theoretical predictions. This approach has been implemented in the "MHD Interpretation Code" (MHD-IC). The code allows to investigate the MHD instabilities even in case of weak MHD activity or complicated mode structure.

Chapter 3

The MHD Interpretation Code

3.1 Introduction

The MHD Interpretation Code (MHD-IC) simulates experimental observations related to a given plasma perturbation for the diagnostics mentioned above, accounting for real plasma geometry and for measured plasma parameters.

The starting point of the simulations is the expected structure of an instability inside the plasma. As was described before, a saturated instability is characterized by its poloidal (m) and toroidal (n) mode numbers, the frequency of the mode rotation (ω), and the radial component of the displacement eigenfunction (ξ_0). These three parameters can be determined from the experiment (magnetic measurements, SXR), and perturbations may be written in the following form:

$$\xi = \xi_0(r) \cdot \cos(m\Theta + n\varphi - \omega t) \tag{3.1}$$

were Θ and φ are the poloidal and toroidal angle respectively. The initial guess for the form of the radial component $\xi_0(r)$[1] results from numerical simulations performed using the XTOR code [30, 6], or from theoretical models. The XTOR code[2] allows for full 3-D nonlinear MHD calculations in toroidal geometry which gives all plasma parameters in each point inside plasma. The resulting perturbations are decomposed into Fourier components. Using

[1] In all equations the plasma radius is normalized to 1. All distances are also given in this unit if it is not specified otherwise.

[2] Brief description of the XTOR code is done in Appendix C.

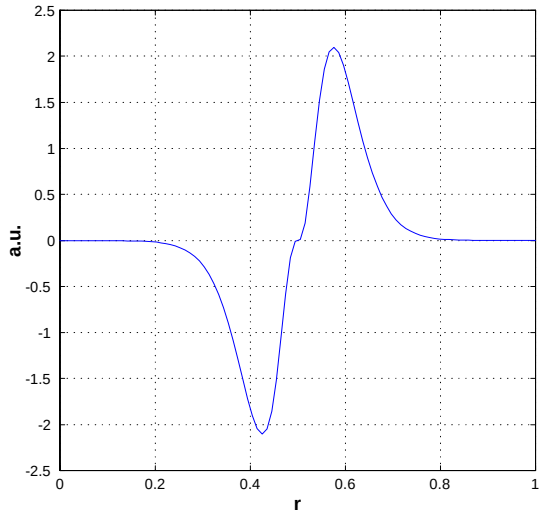

Figure 3.1: Parametrized function describing the magnetic perturbation due to a tearing mode.

only the strongest Fourier component of the eigenfunction, an initial guess is found for the radial profile of the displacement eigenfunction ξ_0. For practical reasons, not the eigenfunction itself but a parameterized form is used in the code, such that only the parameters have to be varied to adjust the eigenfunction to the measurements. For instance, for a single tearing mode the radial profile $\xi_0(r)$ of the perturbation from XTOR is parameterized by the functional form:

$$\xi_0(r,a,b,c,d,r_{res}) = \begin{cases} (r-r_{res})^b \cdot exp(-(\frac{|r-r_{res}|}{a})^c) & r < r_{res} \\ (r-r_{res})^b \cdot exp(-(\frac{|r-r_{res}|}{a})^c) \cdot d & r > r_{res} \end{cases} \tag{3.2}$$

where a corresponds to the island width (W), b determines the behaviour of the function inside the island, c describes the decay of the perturbation outside the island, d shows the relative amplitude of the two peaks, and r_{res} is the position of the resonant surface. In Fig.3.1 this function is plotted for the parameters $a = 0.06, b = 3, c = 1, d = 1, r_{res} = 0.5, W = 0.12$.

One should note that this special form of ξ_0 is only one of the possible variants. When necessary, additional parameters were introduced to obtain a flexible analytical function representing the XTOR results or other theoretical results. Specifically, for double tearing modes an addition parameter

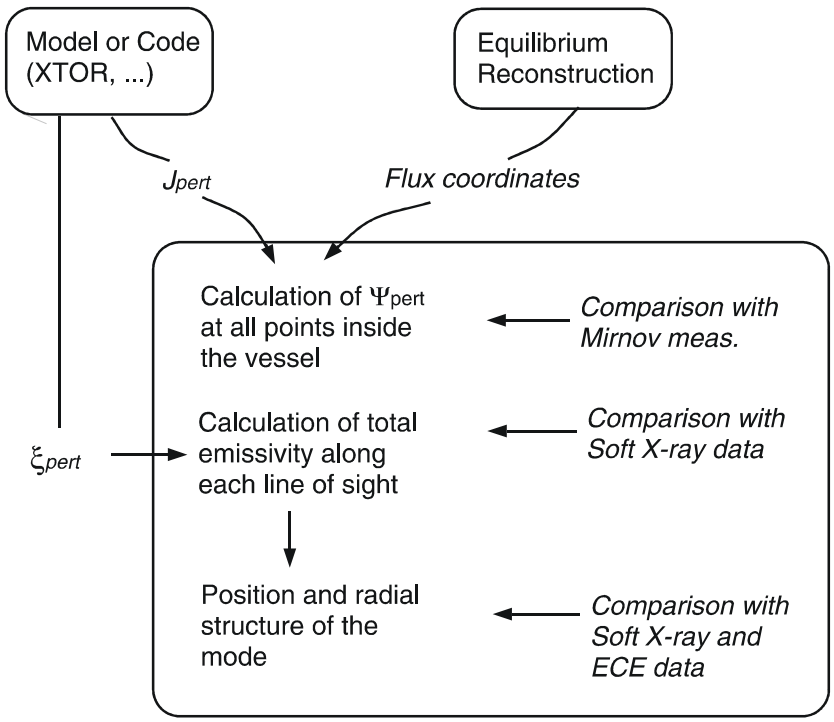

Figure 3.2: Structure of MHD Interpretation Code.

is introduced to represent the amount of coupling of the modes. In principle, any other parametrized function can be used for the perturbation as well. In order to simulate magnetic measurements, a similar approach as for ξ_0 is used to get the initial values for the current perturbations $J_{pert}(r)$.

A scheme of how the code works is shown in Fig.3.2. There are two branches of calculations inside the code. In the first part of the code, the perturbed magnetic field is calculated from the perturbation current $J_{pert}(r)$ at each point inside the ASDEX Upgrade vessel. It gives the possibility to compare phase and amplitude of the magnetic perturbation resulting from the calculation directly with the magnetic measurements.

In the second part, the emissivity along each line of sight $I(N,t)$ is calculated and compared with the corresponding values measured by the SXR

cameras. During this calculation the temperature profile along the ECE line of sight is calculated as well and compared with the experimental one.

For all calculations an equilibrium reconstruction including MSE data is used [27, 31]. The results of the MHD activity analysis regarding the rational surfaces are then applied to improve the equilibrium reconstruction. The whole analysis is then repeated in an iterative manner.

3.2 Magnetic measurements

The magnetic measurements register the time derivative of the magnetic field $\vec{B}$. Since the equilibrium current changes very slowly compared to the mode rotation velocity, the Mirnov coils in general detect only perturbation currents. As the equilibrium currents do not play an important role, the plasma will be represented here only by the perturbation currents. This part of the MHD-IC code is based on Mirnov Interpretation Code (MIC) which was designed for interpretation of the Mirnov measurements (M.Schittenchelm, M.Maraschek, H.Zohm [16, 32]).

Assuming Cartesian coordinates (R, z, φ) where R is the major radius, z represents the vertical coordinate, and φ corresponds to the toroidal angle, the perturbation field can be derived then from the poloidal flux Ψ

$$\vec{B_p} = \frac{1}{R}\nabla\Psi \times \vec{e_\varphi} \ . \tag{3.3}$$

Substituting the magnetic field from (3.3) in Ampere's law (3.4), and taking into account only the toroidal components of perturbation currents ($\partial/\partial\varphi = 0$), Ampere's law (3.4) can be simplified to a 2-D differential equation (3.6), which is solved in real experimental geometry [3].

$$\mu_0 J_\varphi = -\frac{1}{R}\Delta^*\Psi \ , \tag{3.4}$$

$$\text{were } \Delta^*\Psi \equiv R^2\nabla\cdot(\frac{\nabla\Psi}{R^2}) = R\frac{\partial}{\partial R}(\frac{1}{R}\frac{\partial\Psi}{\partial R}) + \frac{\partial^2\Psi}{\partial Z^2} \ . \tag{3.5}$$

$$-(\frac{\partial}{\partial R}\frac{1}{R}\frac{\partial}{\partial R}+\frac{\partial}{\partial z}\frac{1}{R}\frac{\partial}{\partial z})\Psi(R,z) = \mu_0 J_\varphi(R,z) \tag{3.6}$$

[3] The PLTMG solver for partial differential equations with finite element grid method is used in the calculations [33].

In the following, the vacuum vessel is considered as a perfect conductor for frequencies higher than $1kHz$. This is confirmed by Mirnov measurements at the same location inside and outside the vessel wall.

There are however additional metallic structures inside the vacuum vessel (Passive Stabilization Loop (PSL) and support structures). Induction currents appear in these elements and influence the resulting magnetic field. These currents are taken into account in a self consistent way.

Finally, the variation of the distance between neighboring flux surfaces should also be considered. Due to variations of the equilibrium magnetic field the cross-section of a tube between the neighboring surfaces is changed, but the current flowing in the tube does not change. Thus, the surface current inside the tube varies $j_{tube} \sim 1/RB_\Theta$ because of this geometric effect. For our 2-D problem only the toroidal component of the current is important and the coefficient becomes $j_{tube} \sim \left(\sqrt{\mid \vec{B} \mid^2 - B_\Theta^2}\right) / (RB_\Theta)$ [16].

In the MIC code the radial profile of the perturbation current for MHD modes has been assumed to be a constant over the region close to the corresponding rational surface. This approximation however, is quite inaccurate. To demonstrate the difference between this assumption and the shape of a real perturbation current, the simple case of a tearing mode in cylindrical geometry will be considered. Assuming the perturbation flux at the plasma edge being the same, the perturbation fluxes using a step function for the current at the resonant surface and the solution of the tearing mode equation in cylindrical geometry have been evaluated. As shown in Fig.3.3 the resulting fluxes and the perturbation currents have significant differences. Moreover, this simple assumption for the perturbation current can describe only stable tearing mode[4]. It becomes obvious that for a given magnetic perturbation as measured by the Mirnov coils, the real plasma perturbations would be underestimated by only using a constant current density at the rational surface. For a more accurate treatment of the magnetic perturbation within the plasma, an arbitrary current profile is allowed in the MHD-IC code.

The real plasma shape in tokamaks has much more complicated form than a simple cylindrical model (e.g. see Fig.1.2). To describe this real plasma equilibrium it is convenient to use coordinates defined by the field itself. In this coordinates each field line will be straight and the plasma cross-section will have a circular form[34]. It is so-called *flux coordinates* (ρ, θ), where ρ

[4]Detailed calculations are presented in appendix B.

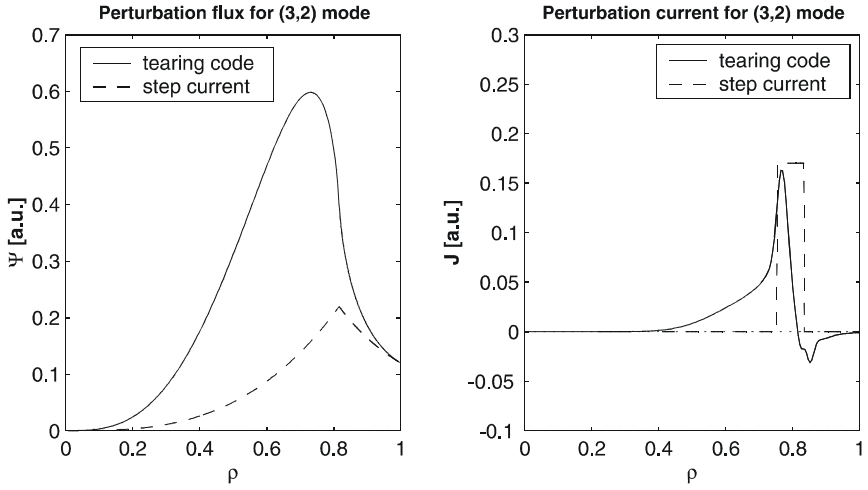

Figure 3.3: Perturbation fluxes and perturbation currents for a $(3, 2)$ mode resulting from the tearing mode equation (solid curves) and from a "step function" assumption (dashed curves). One can see significant difference between these approaches ($r_{res} = 0.81$).

is the radial coordinate and θ is the angle in the flux coordinates. In our calculations, we use for the radial coordinate either the normalized poloidal flux radius ρ_{pol} or the normalized toroidal flux radius ρ_{tor}, which defined as

$$\rho_{pol} = \sqrt{\frac{\Psi - \Psi_a}{\Psi_s - \Psi_a}} \quad \text{and} \quad \rho_{tor} = \sqrt{\frac{\Phi - \Phi_a}{\Phi_s - \Phi_a}} \ ,$$

where Ψ is the poloidal flux, Φ is the toroidal flux, index s refers to the separatrix, index a to the magnetic axis. These coordinates are normalized such that $\rho = 0$ on the magnetic axis and $\rho = 1$ on the plasma boundary. Evaluation of the poloidal angle θ for the flux coordinates is described in Ref.[32].

The detailed shape of the current perturbation $J_{pert}(\rho)$ starts from a parametrized component of XTOR code results as described before. For a single tearing mode the following parametrization is used

$$J_{pert}(\rho) = \begin{cases} J_{\max} \cdot ((\rho - \rho_1)/(\rho_2 - \rho_1))^{\alpha_1} & \rho_1 < \rho < \rho_2 \\ (J_{\max} - J_{\min}) \cdot (\rho - \rho_2)/(\rho_2 - \rho_3) + J_{\max} & \rho_2 \leqslant \rho \leqslant \rho_3 \\ J_{\min} \cdot (1 - (\rho - \rho_3)/(\rho_4 - \rho_3))^{\alpha_2} & \rho_3 < \rho < \rho_4 \end{cases} \quad (3.7)$$

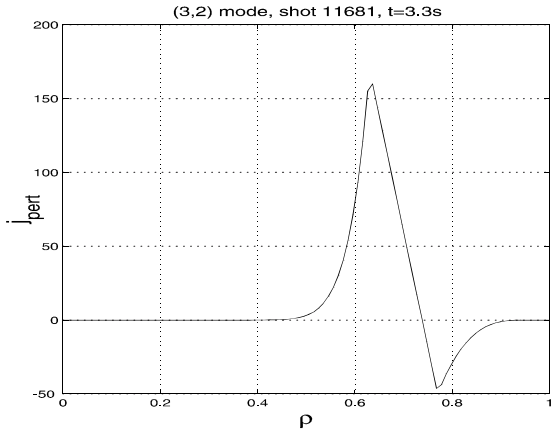

Figure 3.4: Perturbation current profile for $(3, 2)$ mode, #11681, t=3.3s.

where $\rho_2 = \rho_{res} - W/2$ and $\rho_3 = \rho_{res} + W/2$. To exclude all geometrical effects, the initial perturbation current $J_{pert}(\rho)$ is defined in the flux coordinates (ρ, θ) and then transformed into Cartesian coordinates (R, z) using equilibrium reconstruction.

As an example we consider a (3,2) tearing mode. The position of the mode was found from ECE measurements. The shape of the perturbation current profile $J_{pert}(\rho)$ was varied to obtain the best agreement with magnetic measurements. The best fit for the perturbation current is shown in Fig.3.4 ($J_{\max} = 170$, $J_{\min} = -50$, $\rho_{res} = 0.7$, $W = 0.14$, $\rho_1 = 0.3$, $\rho_4 = 0.95$, $\alpha_1 = 8$, $\alpha_2 = 3$). The resulting perturbation flux due to the (3,2) mode is shown in Fig.3.5. A comparison of the calculated amplitude and phase with magnetic measurements is shown in Fig.3.6. The distance between the minimum and the maximum value of the perturbation current is approximately the width of the islands (see Fig.3.4) [35]. This width derived from the magnetic measurements ($W \approx 7cm$) is in good agreement with the corresponding ECE measurements ($W \approx 6 - 7cm$).

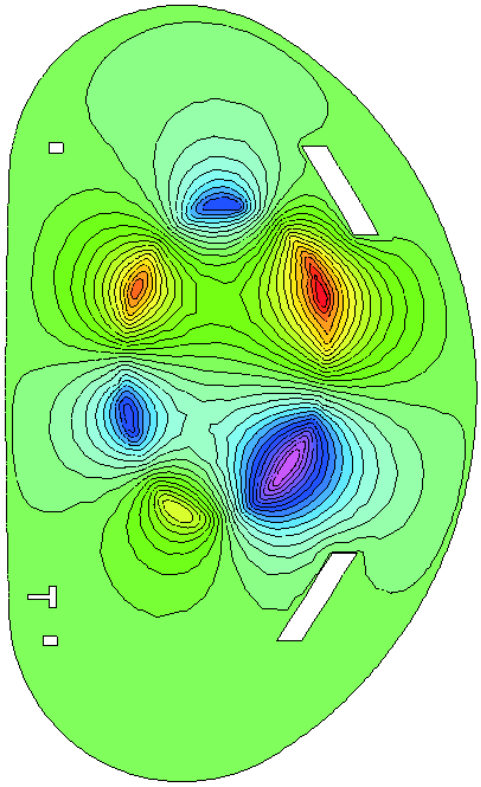

Figure 3.5: Calculation domain and perturbation flux for $(3, 2)$ mode (#11681, t=3.3).

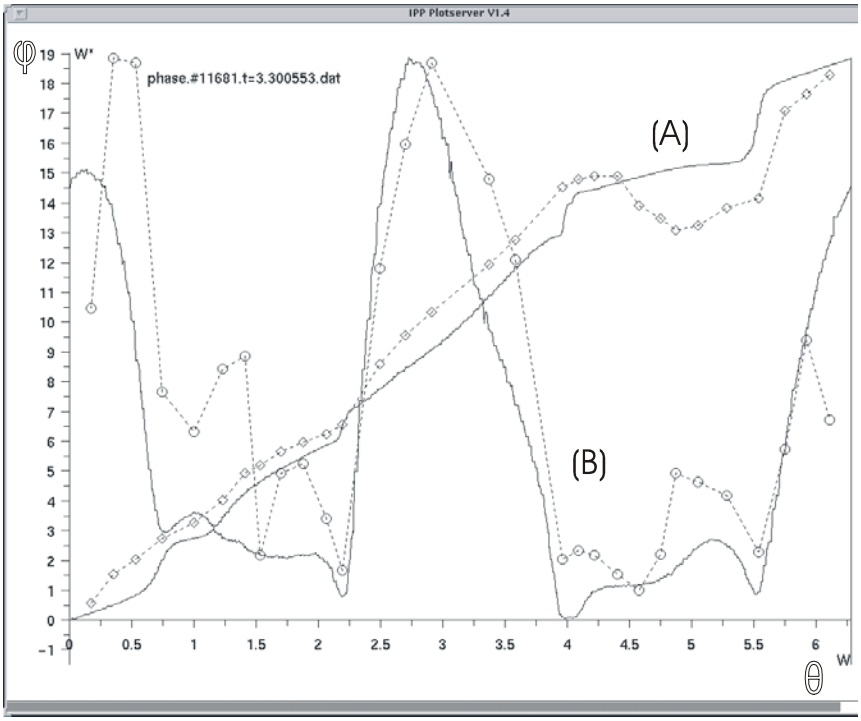

Figure 3.6: Phase (A) and amplitude (B) from calculation (solid lines) compared with experiment (dashed lines) depending on the poloidal angle Θ for the same discharge as in the previous two figures.

3.3 Soft X-ray measurements

Signals from soft X-ray (SXR) cameras and electron cyclotron emission (ECE) give information about the behaviour of MHD modes directly from plasma interior. Performing measurements along different lines of sight allows to determine the spatial behaviour and the amplitude of MHD activities inside the plasma.

The energy spectrum of SXR radiation consists of a continuum of free-free bremsstrahlung, free-bound recombination radiation, and bound-bound line radiation (only minor contribution) [36]. For a Maxwell's velocity distribution and assuming a hydrogen model for the impurity ions, the radiated power $d\varepsilon$ per unit volume in the photon energy interval dE reads

$$(\frac{d\varepsilon}{dE})_{ff} = \alpha n_e^2 Z_{eff} g_{ff}(T_e, E) \frac{\exp(-E/T_e)}{\sqrt{T_e}} \ , \tag{3.8}$$

where T_e is the electron temperature in $[keV]$, $n_e[10^{13} cm^{-3}]$ is the electron density, the effective charge is $Z_{eff} = \sum_i n_i {Z_i}^2 / n_e$, $\alpha = 3 \cdot 10^{11}$ is a constant, and $g_{ff}(T_e, E)$ corresponds to the temperature-averaged Gaunt factor. The intensity results from integration over the photon energy:

$$\varepsilon(r, \theta) = \int \varepsilon(E; r, \theta) f_{camera} f_{filter} dE \ . \tag{3.9}$$

Standard assumptions can be made to calculate the emissivity along a SXR line of sight. The line is divided into small pieces of length dl, and the plasma parameters are assumed to be uniform inside each piece (see Fig.3.7). The resulting emissivity ε_{total} is then simply the sum over the emissivities ε_k inside each element k, multiplied by the element's length dl

$$\varepsilon_{total} = \sum_k \varepsilon_k \cdot dl \ , \tag{3.10}$$

where

$$\varepsilon_k = G \cdot \frac{n_e^2}{\sqrt{T_e}} \cdot \sum_{i=1}^{N} f_{sum}(E_0 + i\Delta E) \cdot \exp(-\frac{(E_0 + i\Delta E)}{T_e}) \Delta E \ . \tag{3.11}$$

The integral in Eq.3.9 is substituted by a sum over the energy in Eq.3.11.

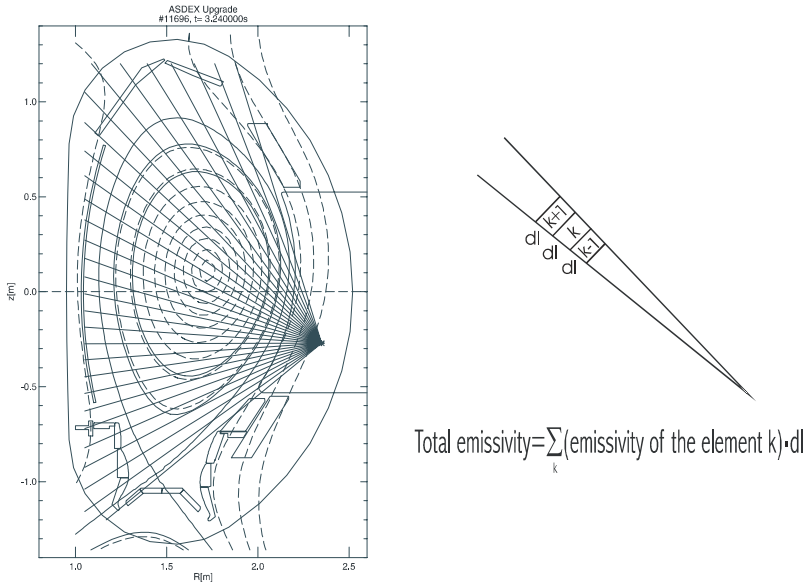

Figure 3.7: An example of the emissivity calculation for a line of sight.

In Eq.3.11, G represents a geometrical factor that describes the variation of the "effective" width of a pinhole for different detectors inside one camera [19]:

$$G = \frac{4\pi\Delta^2}{A_d A_p(\cos\alpha_i - \frac{b_3}{b_1}|\sin\alpha_i|)}\ , \tag{3.12}$$

$$A_d = d_1 d_2,\ A_p = b_1 b_2 \tag{3.13}$$

(d_1 - diode width; d_2 - diode length; b_1 - pinhole width; b_2 - pinhole length; b_3 - pinhole thickness; α_i - angle between the i^{th}-detector and the camera axis; Δ - focus length of pinhole camera).

The passivated ion-implanted silicon diodes are used in the SXR cameras on the ASDEX Upgrade. These diodes are manufactured from silicon and have an aluminum coating on the front side. These two substances make a $p-n$ transition. Photons enter in the detectors and generate electron-hole pairs by the photoelectric effect [19]. The geometrical parameters of the SXR system using in the MHD-IC code are presented in the table:

Camera	N	$R[m]$	$z[m]$	γ	δ	Δ	d_1	d_2	b_1	b_2
A^5	30	1.411	-1.075	79^o	2.15^o	122	2.6	20	2.6	28.04
B	30	2.351	-0.271	163^o	3.80^o	69.7	2.6	8.6	2.5	18
C	60	2.371	0.2526	187.5^o	1.86^o	141	2.6	20	2.5	35
D	30	2.020	0.875	-137^o	3.80^o	69.7	2.6	8.6	2.5	18
E	12	1.402	1.170	-85^o	3.80^o	69.7	2.6	8.6	2.5	18

N - number of the lines of sight

R, z - position of pinhole in mm

γ - angle of camera axis (middle of array of lines of sight) in deg .

δ - average distance between neighboring lines of sight in deg .

Δ - camera focus (distance between pinhole and detectors) in mm

d_1, d_2, b_1, b_2 - width (1) and length (2) of detector (d) and pinhole (b) in mm

Transmission parameters of the SXR system depending on the photon energy are collected in the $f_{sum}(E)$ coefficient.

$$f_{sum}(E) = T_{Be}(E) \cdot T_{Al}(E) \cdot T_{Si,dead}(E) \cdot (1 - T_{Si,absorb}(E)) \tag{3.14}$$

The ASDEX Upgrade SXR cameras have two different suites of beryllium filters. The first suite has a "Be" foil with a thickness of 100 μm and the second with 12 μm. The first coefficient in Eq.3.14 represents these beryllium filters. The second coefficient T_{Al} corresponds to aluminum coating of the SXR detectors ($0.2\mu m$). Then, there are coefficients for silicon "dead layer" ($0.2\mu m$) and silicon absorber region ($300\mu m$).

As was mentioned before, the MHD perturbation rotates with a frequency ω and thus $\xi \sim \cos(\omega t)$. During one period of the rotation, this behaviour can be represented as a simple phase shift of the perturbation and it reads

$$\xi \sim \cos\left(\frac{2\pi}{k} i\right), \; i = 1...k \; . \tag{3.15}$$

SXR signals $I(N,t)_{calc}$, were N is line number and t represents time, are calculated using the formulas (3.10 - 3.11, 3.15) for different phase angles of perturbations in order to simulate a poloidal rotation of the modes.

[5] This new camera was recently installed in ASDEX Upgrade (from discharge #14049). Before that time, the camera had been directed only at the divertor region.

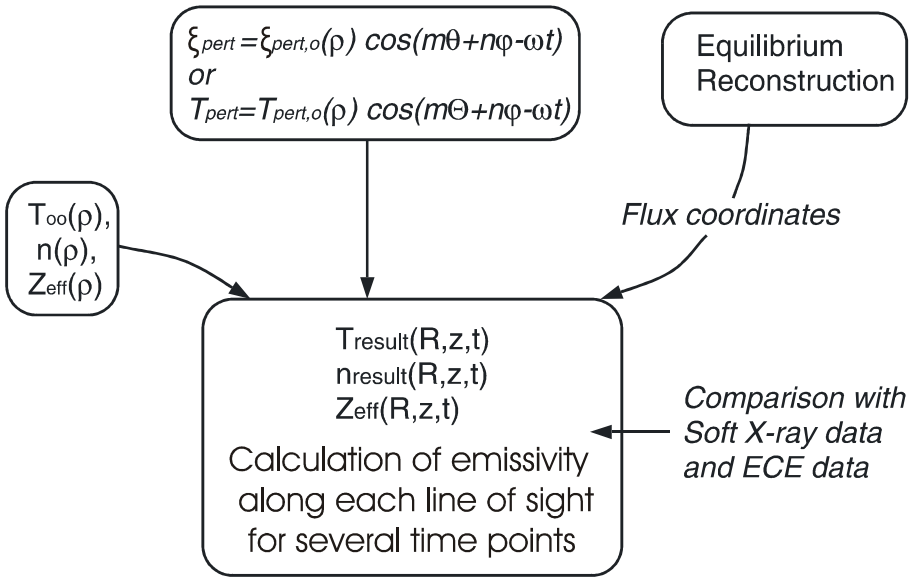

Figure 3.8: Scheme of the second part of MHD-IC code.

As the MHD activities correspond solely to relative changes of the signal, an absolute calibration of the SXR cameras is not important here. From Eq.3.8 it is obvious that the SXR signals are most sensitive to temperature perturbations T_{pert}. Changes of the Z_{eff} profile are not considered in the following, which is a good approximation for discharges without impurity accumulation[6].

The structure of the SXR and the ECE part of the MHD-IC code is shown in Fig.3.8. In this part the displacement eigenfunction or the temperature perturbation are used as input parameters to describe the MHD activity. As actually the temperature perturbation is required, the following relation between the displacement and the temperature perturbation is used [37]

$$\xi_{pert} = -\frac{T_{pert}}{\nabla T_{0,0}} \ . \tag{3.16}$$

For the equilibrium quantities $T_{0,0}, n_e, Z_{eff}$ the measured values are used. The perturbations are added onto the equilibrium parameters, by using the

[6]The Z_{eff} profile is inserted in the code in the same way as the others profiles and assumed to be a constant. It can be easily used for discharges with impurity puffing if it is necessary.

equilibrium reconstruction (including motional Stark effect measurements), transformed from the flux coordinates (ρ, θ) into the (R, z) plane. The coordinate transformation is the same as in the first part of the code. The resulting profiles $T(R, z, t)$, $n(R, z, t)$, $Z_{eff}(R, z, t)$ are then used to simulate the SXR emissivity along a line of sight.

The line of sight of the ECE measurements in ASDEX Upgrade is the horizontal line with $z = 0.1m$. This position usually corresponds to the position of the plasma center in the machine. During a discharge, the ECE measurements provide temperature values for a number of points inside the plasma along this line. In order to compare these ECE measurements with our model, the temperature profile along the ECE line of sight is calculated during the emissivity calculations in this part of the code. The displacement eigenfunction ξ_{pert} is also mapped onto the ECE line of sight. It allows to compare the displacement eigenfunction from calculation ξ_{pert} directly with the corresponding eigenfunction from experiment as will be shown below.

3.4 MHD activity analysis

3.4.1 Mirnov signals

An analysis of the MHD activity usually starts from the identification of the dominant frequencies and the determination of the mode numbers from magnetic measurements. The algorithm for the determination of the mode numbers was depicted in Fig.2.1. After that, phase and amplitude of the Mirnov signals are simulated and compared with experimental values as described in the previous section. The shape of the perturbation currents is varied to get the best possible agreement with experimental observations.

3.4.2 Soft X-ray signals

Comparison of the total SXR signals

First information about the MHD activity can be found directly from the total SXR signal. As an example, in Fig.3.9, the SXR signal of a discharge with a $(2, 1)$ mode is given.

The position of the camera lines of sight together with a $(2, 1)$ tearing mode structure are shown in Fig.3.9a. During the mode rotation, the SXR emissivity along the lines of sight $I(N, t)$ changes due to the temperature and

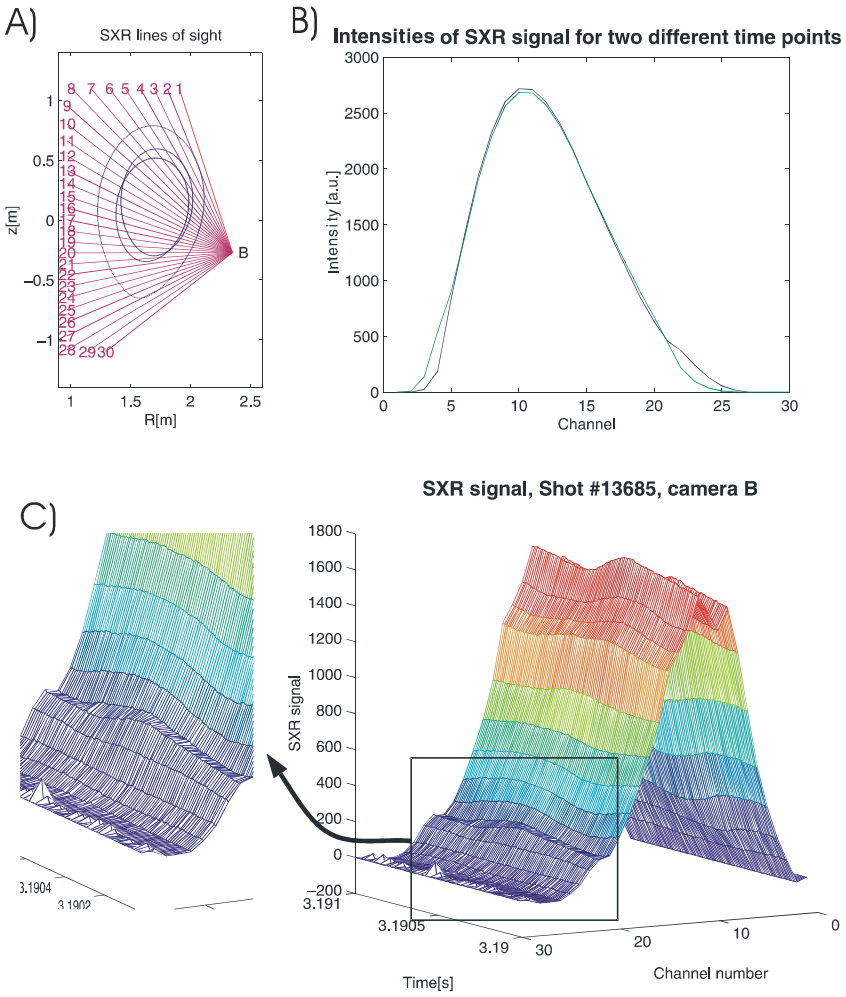

Figure 3.9: A) Position of SXR line of sight (B-camera on ASDEX Upgrade) together with a sketch of $(2, 1)$ magnetic islands. B) Intensities for two different position of the islands. C) Experimental SXR signal with 'wave'-like structure.

density flattening inside the islands. The intensities $I(N,t)$ for two different positions of the island are shown in Fig.3.9b. The rotating mode changes the profile of the function $I(N,t)$ close to the resonant surface. Looking at a time series of the SXR intensity one finds a "wave"-like structure in the mode position region Fig.3.9c. Moreover, it is possible to estimate the island width if the MHD activity is sufficiently strong.

A more detailed information can be gained if the perturbed part of the SXR signal is separated from the equilibrium background. Two different tools are implemented for this purpose in our analysis: Fast Fourier Transformation (FFT) and Singular Value Decomposition (SVD).

Fast Fourier transformation

A FFT algorithm is applied to separate the perturbed part of the SXR signal from the total signal $I(N,t)$ [38]. This method allows to make spectral analysis using discrete base of data points. The one-dimensional FFT of a sequence of n values $x_i, j = 0, 1, ..., n-1$, is defined as

$$\hat{x}_k = \frac{1}{\sqrt{n}} \sum_{j=0}^{n-1} x_i \exp\left(-\frac{2\pi i j k}{n}\right) \tag{3.17}$$

for $k = 0, 1, ..., n-1$. The original values x_i and the transformed values $\hat{x}_k$ are, in general, complex.

The FFT transformation is applied for calculated $I(N,t)_{calc}$ and measured $I(N,t)_{exp}$ signals. Then, calculated and measured FFT amplitude and phase are compared to determine shape and position of the displacement eigenfunction of the observed MHD activity. It will be shown later that the FFT amplitude is very sensitive to the form of the displacement eigenfunction.

Singular value decomposition

Singular Value Decomposition (SVD) analysis allows to separate experimental signals on spatial and time elements [39, 40]. For this analysis, measured data are collected in a $(n \times m)$ matrix $\mathbf{X}$ with $m \leqslant n$:

$$\mathbf{X} = (x_{ij}) \ ,$$

where $x_{i,j}$ has $i = 1, ..., n$ time points and $j = 1, ..., m$ spatial points. Then, the SVD algorithm decomposes $\mathbf{X}$ in the following form

$$\mathbf{X} = \mathbf{U}^T \mathbf{S} \mathbf{V} \tag{3.18}$$

into an orthogonal $(n \times n)$ matrix $\mathbf{U}$, a diagonal $(n \times m)$ matrix $\mathbf{S}$, and an orthogonal $(m \times m)$ matrix $\mathbf{V}$. From algebraic analysis it follows that $\mathbf{U}\mathbf{U}^T = 1$, $\mathbf{V}\mathbf{V}^T = 1$, and $\mathbf{S}$ is diagonal matrix with non-negative diagonal elements s_i [41]. Moreover, eigenvalues of $\mathbf{S}$ have a strict descending order

$$s_1 \geqslant s_2 \geqslant ... \geqslant s_m \geqslant 0 \ . \tag{3.19}$$

The s_i are called the *singular values* of $\mathbf{X}$. From this hierarchy of the singular values it follows that the first singular value gives the strongest component of the signal (unperturbed part), the second value corresponds to the strongest perturbation component and so on. At the same time, the temporal and spatial SVD eigenvectors create a new orthogonal coordinate system.

Filtering of the signal is then a simple reconstruction of the signals with only the p largest singular values

$$\hat{x}_{ij} = \sum_{k=1}^{p} u_{ki} s_k v_{kj} \ .$$

As a measure of the quality of the reconstructed signal $\hat{x}_{ij}$, the following parameter can be introduced [21]:

$$\sigma = \sum_{k=1}^{p} s_k^2 / \sum_{k=1}^{m} s_k^2 \ .$$

This value represents the relative quality of our approximation using only the first p components.

The SVD algorithm separates the space and time dependent components of the perturbations from the total signal. Since the frequency of the mode rotation can easily be determined from experiment (Mirnov coils, SXR) most interesting for the analysis are the spatial components. The first spatial component corresponds to the unperturbed part of the signal, the unperturbed equilibrium. The second and the third components correspond to the strongest MHD activity. These two component are most interesting for the MHD analysis and describe the MHD activity with sufficient quality. Only in case of several modes with different rotation frequencies further components are required. The singular value decomposition for the calculated signal $I(N,t)_{calc}$ and for the experimental signal $I(N,t)_{exp}$ are performed in the code. Comparing the spatial SVD eigenvectors from theory and experiment,

the best fit for the displacement eigenfunction is found. This fitting procedure should be done simultaneously with fitting of the FFT amplitude.

It is important to note that the sign of an SVD eigenvector depends on actual SVD algorithm. Thus, only the shape of the eigenvector should be compare with the corresponding experimental eigenvectors.

Accuracy of the SXR data analysis

The FFT and SVD techniques are flexible enough to obtain information about week MHD activity even if this activity only slightly changes the total signal $I(N,t)_{exp}$. This is an advantage of the code compared to tomographic reconstructions. The other advantage is the possibility to increase the spatial resolution. For standard tomographic methods, a low number of SXR detectors and errors in absolute values of the emissivity lead to error bars in the radial direction of about $\Delta\rho \simeq 0.14 - 0.16(6 - 8cm)$ [42, 43]. Special methods of the tomography adapted to the condition in fusion plasma, for instance differential rotation tomography method, can increase the resolution in radial direction to $\Delta\rho \simeq 0.1(5 - 6cm)$ [20, 44, 45]. On the other hand, applying a combination of the FFT and the SVD technique and by using several SXR cameras simultaneously, the error bars can be reduced to $\Delta\rho \simeq 0.05(2 - 3cm)$, which is already close to the width of the lines of sights. Changes of perturbations with smaller amplitudes do not affect the result and cannot be resolved with the current SXR system on ASDEX Upgrade. One should note however that FFT and SVD technique cannot give any information about the absolute value of ξ, a comparison of $I(N,t)_{calc}$ and $I(N,t)_{exp}$ would be required for that. Since for our analysis only the relative SXR signals are interesting, the problems with the absolute calibration, which are rather complicated, are not important for here.

3.4.3 Electron cyclotron emission signals

The result of ECE measurements is the temperature profile $T_e(R,z;t)_{exp}$ along the ECE line of sight. This temperature profile is compared with the calculated profile from MHD-IC code $T_e(R,z;t)_{calc}$. The distance between neighboring measurements of the temperature profile $T_e(R,z;t)_{exp}$ depends on the discharge conditions (usually about $0.5cm$).

From the fast ECE channels it is also possible to calculate the displacement eigenfunction directly from the measured time dependent temperature

profile

$$\xi_{ece} = \frac{T_e(t) - \langle T_e \rangle_t}{\nabla \langle T_e \rangle_t} \tag{3.20}$$

and to compare it with ξ_{pert} from the code input. It gives an independent comparison of SXR and ECE data. Unfortunately, the fast ECE measurements usually do not exist for the whole plasma region due to the restrictions mentioned in the description of the ECE diagnostic.

3.4.4 Limits of the method

There are several limits of the method which should be taken into consideration. Firstly, error bars of the diagnostics restrict the accuracy of the analysis. These errors have minimum possible values when all channels of the diagnostics are used. This however is usually not the case, e.g. SXR cameras have more lines of sight then the usual number of the amplifier channels. In addition to these limits, we restrict our calculations by using only the strongest Fourier components of the perturbations. This approximation is valid only when toroidal coupling to higher m-modes is not important to measured signals. Implementation of the toroidal coupling in the code is under development right now.

3.4.5 Conclusion

The MHD-IC code allows to perform an analysis of MHD activities using all available experimental information related to these instabilities. The method substantially increases the accuracy compared to a tomographic reconstruction technique and simplifies the identification of the modes. These features are especially important for the identification of a complicated mode structure.

Such an analysis of MHD activity using the MHD-IC code is demonstrated for different kinds of MHD activities in the next chapters.

The installation procedure and input parameters of the MHD-IC code are described in the Appendix D.

Chapter 4

Tokamak scenarios

There are two concepts in tokamak researches which should lead to a working fusion power plant. The first concept called *"conventional tokamak scenario"* extrapolates experimental results from existing tokamaks. In this scenario the plasma current, necessary for heating, and confinement, is driven inductively. Thus, the central solenoid together with the nuclear shielding of the toroidal field coils determine the scale of the machine which is rather large. Moreover, steady state operation is not possible for this type of the reactor and the machine has to operate in a pulsed mode. Consequently, an energy storage system is required to ensure continuous energy and the capital cost of a fusion power plant increases [46].

The other concept is the so-called *advanced tokamak scenarios*. This approach tries to operate the fusion tokamak in steady state [46]. Improved confinement for this type of operations reduces the necessary plasma current I_p for high fusion performance Q (Q = fusion power/ externally supplied plasma heating power). The main idea behind that is non inductive current drive with high bootstrap current fraction. The bootstrap current is proportional to the pressure gradient [3, 47]

$$j_b \sim -\sqrt{\epsilon}\frac{1}{B_\theta}\frac{\partial p}{\partial r} \ ,$$

where p represents the pressure, r is the radial coordinate, the local inverse aspect ratio is $\epsilon = r/R$, and B_θ is the poloidal magnetic field. From this equation follows that for a large bootstrap current fraction large values of the poloidal beta are necessary. Furthermore, the pressure gradient has its maximum value out of axis and the current profiles will be generally non-

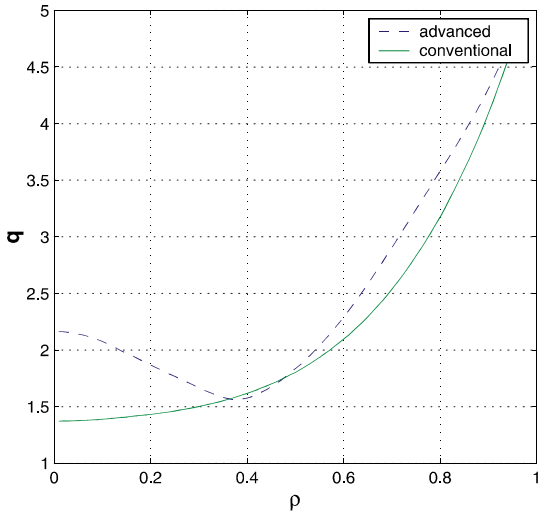

Figure 4.1: Examples of typical q-profiles in advanced and conventional tokamak scenarios.

monotonic. The non-monotonic current profiles lead to inverted safety factor profiles (see Fig.4.1). This q-profile has a minimal value out of axis. In the negative magnetic shear region, the toroidal drive of the modes responsible for turbulent transport is reduced. In addition, the reversed q-profiles allow to suppress turbulence in the plasma through sheared $\vec{E} \times \vec{B}$ rotation and create internal transport barriers (ITBs) [48, 49]. The other aspect of the advanced scenarios is a possibility to access second stability region with respect to the ideal ballooning modes [50]. The advanced tokamak operations are intensively studied on all main tokamaks [49, 51, 52, 53].

Various scenarios of advanced tokamak concepts have been investigated on ASDEX Upgrade. The current density was modified in order to achieve improved core confinement. The most promising concept was obtained during current ramp phase by applying NBI. This reversed shear scenario has $q_{\min} \geqslant 1.5$ and large bootstrap current fraction [54, 55, 56].

Experimental identification of the reversed q-profiles is difficult task. The motional Stark effect (MSE) diagnostic allows to reconstruct the current profile but has large error bars in the plasma core. Thus, in the experiments, it is difficult to identify that the q-profiles are really reversed. Analysis of MHD instabilities is usually used to overcome this problem. For instance, the

q-profile in Fig.4.1 has two $q = 2$ resonant surfaces and two mode with the same helicity may appear in this case. After identification of these modes, one can really be sure that the q-profile is reversed. At the same time, it is rather hard to find the inner mode using only available tools and there is a need for an interpretation code which can resolve such MHD activity. In chapter 7, we demonstrate that the MHD Interpretation Code is well fitted for this task.

The reversed q-profiles bring new MHD phenomena which are not observed in conventional scenarios. For example, existing of two rational surfaces with the same q-values described above may lead to appearance of a so-called double tearing mode (DTM), which consists of two coupled tearing modes. These new phenomena together with usual MHD instabilities have been observed in the advanced tokamak experiments on ASDEX Upgrade [57]. Most of them limit the plasma parameters, for instance the maximum achievable normalized plasma pressure $\beta_N = \beta_t / (I_p / aB_t)$, where $\beta_t = \langle p \rangle / (B_t^2 / (2\mu_0))$, a represents the minor radius, B_t is the toroidal magnetic field and $\langle p \rangle$ is the volume averaged plasma pressure. These instabilities either terminate the improved confinement or even lead to disruptions. Consequently, the investigation of these instabilities is a particular interest.

In the next chapters we investigate different MHD phenomena in the conventional and advanced tokamak scenarios on ASDEX Upgrade. As will be shown using MHD-IC code it is possible to find out the detailed structure of these phenomena.

Chapter 5

MHD activities in conventional scenarios

The conventional tokamak scenarios are characterized by inductive current drive and thus the current profile has the maximum of the current density in the plasma center. This leads to a monotonic q profile with continuously increasing q values as was shown in Fig.4.1. Consequently, for any two resonant surfaces in the plasma, the outer surface has always a higher value of q.

We begin our investigation with an ideal kink mode (in form of fishbone activity) which is quite easy to analyse as it has a large amplitude localized in the plasma core. Afterwards different types of fishbone activity on ASDEX Upgrade are investigated.

5.1 The kink mode

The internal kink mode is an usual type of MHD instabilities in ASDEX Upgrade discharges for conventional scenarios [58, 59]. This mode is often driven by fast particles, and thus appearing as fishbone oscillations. It is the form of experimental signals of these oscillations which has given the name fishbone to this instability (see Fig.5.1). In the next section, background of this mode and its effect on the plasma will be discussed in detail. Since the kink mode is easy to analyse as it has a large amplitude in the plasma core, we use it as first example for our analysis.

The helicity of the fishbone activity can easily be obtained from the mag-

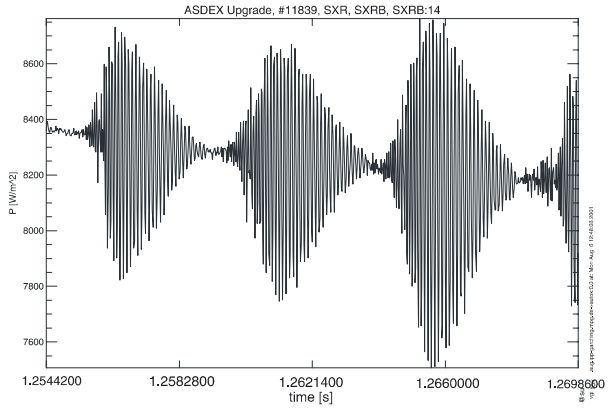

Figure 5.1: Internal $(1,1)$ kink mode in form of fishbone oscillations (discharge #11839, t=1.25s, SXR signal, "B"-camera, channel 14).

netic measurements to be $m = 1, n = 1$. Theory predicts a step function for the corresponding displacement eigenfunction [60, 61, 62], which is used as an initial guess for the displacement in the calculations here. The perturbation is parametrized in the following form:

$$\xi_{kink} = \begin{cases} \max(\xi_0(r,a,b,c,d)) & r < r_1 \\ \xi_0(r,a,b,c,d) & r \geqslant r_1 \end{cases} , \tag{5.1}$$

where ξ_0 is determined by Eq.3.2. Varying the form of the function ξ_{kink}, very good agreement could be obtained for the amplitude of fast Fourier transformation (FFT) and for the singular value decomposition components (SVD) between experiment and calculation (with the parameters $a = 0.02$, $b = 3$, $c = 1$, $d = 0$, $r_{res} = 0.45$, $r_1 = r_{res} - 0.6$ for Eq.(5.1)). These results are shown in Figs.5.2,5.3. It is important to note that the sign of an SVD component depends from the type of the SVD algorithm and only the shape should be compared with the experiment.

As was mentioned before, this ideal kink mode example is considered to be a good test for our method. In this case, the position of the mode r_{res} can be estimated directly from the raw SXR data. Central channels of the B-camera cross the $q = 1$ surface and show a signal similar to Fig.5.1. If one moves outside from the central channel, one can find that at some channel the fishbone activity vanishes. This line does not cross the rational surface anymore and the channel is tangential to a flux surface with a q value a little

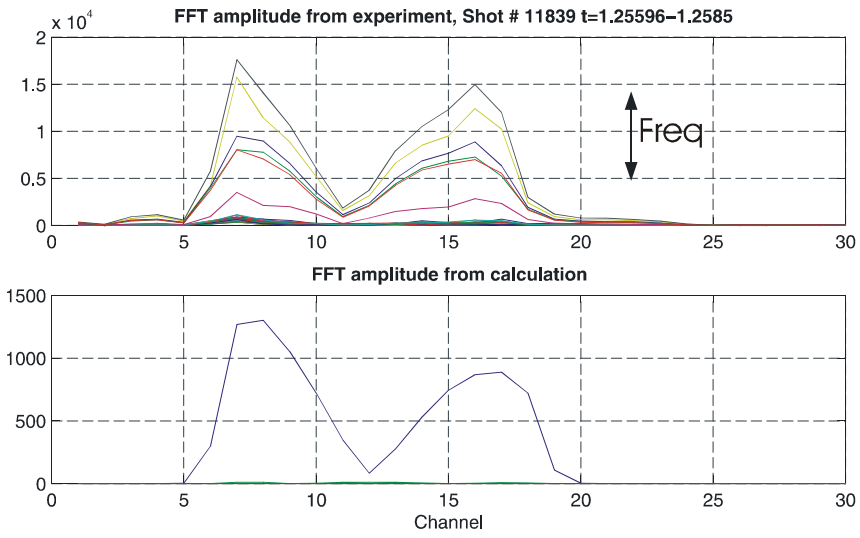

Figure 5.2: Comparison of the observed and calculated FFT amplitudes for the kink mode (Shot #11839, $t = 1.25s$). The FFT amplitudes of the experimental signal are shown for a number of frequencies.

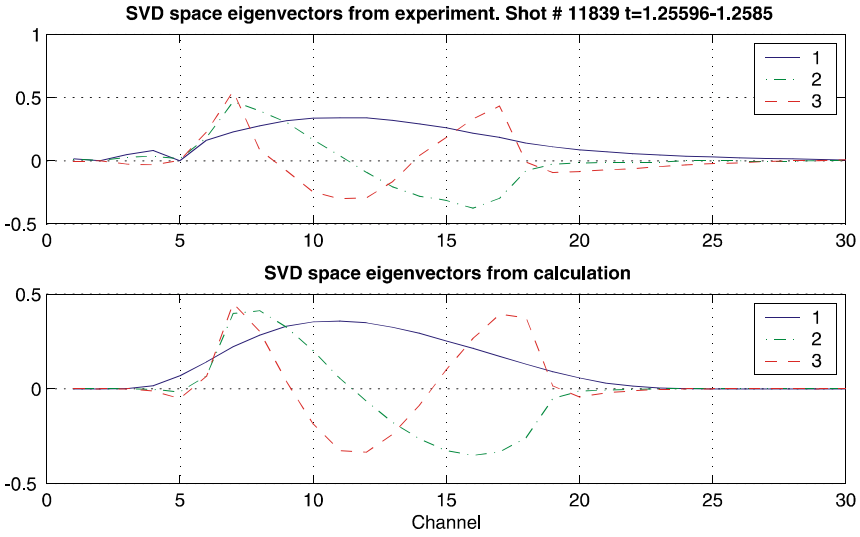

Figure 5.3: Comparison of the SVD eigenvectors for the $(1,1)$ kink mode (#11839, t=1.25s).

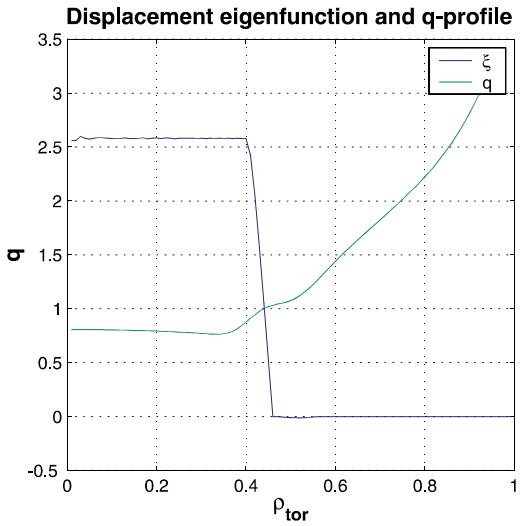

Figure 5.4: Displacement eigenfunction for the $(1, 1)$ kink mode and the q-profile derived from equilibrium reconstruction including MSE measurements (Shot #11839, t=1.25s).

higher then 1. This flux surface in our case has $\rho \approx 0.5$ and agrees well with the result of our analysis ($\rho = 0.45$).

The displacement eigenfunction from MHD-IC code for the parameters listed above is shown in Fig.5.4 together with the q-profile (with MSE). The resulting eigenfunction agrees very well with the position of the $q = 1$ surface from the equilibrium reconstruction as well as with the shape of that function resulting from XTOR (Fig.5.5). Consequently, there is good agreement between modelling and experimental observations, and thus the eigenfunction found from our analysis should be correct.

5.2 Fishbones for different types of neutral beam injection

It is of particular interest to investigate the fishbone instability in tokamak fusion research [59, 63, 64, 65]. Experiments have shown that neutral beam injection (NBI) can destabilize a mode with dominant toroidal and poloidal wave numbers $(m, n) = (1, 1)$. This is due to inverse Landau damping ef-

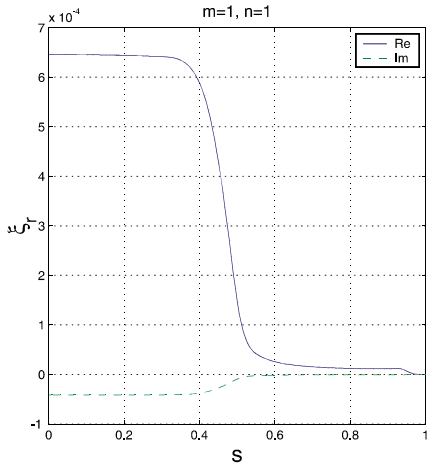

Figure 5.5: Dominant FFT $(m, n) = (1, 1)$ component ξ_r for a kink mode resulting from the XTOR code.

fect which lead to a growth in case of the fishbones. The resonance occurs between the toroidal wave velocity of the instability and the rotation of the trapped energetic particles from the injected beam. Thus, the existence of the trapped particle is necessary condition for the fishbones. A model of fishbones proposed by Chen et al.[66] shows that the particles trapped within the $q = 1$ radius can kinetically destabilize an internal kink mode with frequency

$$\omega \simeq \omega_p = \frac{E}{m_b r R \omega_0} \ ,$$

where ω_p is the precession frequency of the resonant beam ions, E corresponds to the energy of the ions, R is the major plasma radius, r is the minor plasma radius, $\omega_0 = eB/m_b$ describes the gyrofrequency, and m_b is the mass of the fast ions [58].

The most important effect of the fishbone instability on the plasma is the ejection of the resonant fast ions during the bursts. This is the reason why fishbones reduce the efficiency of the heating and can also limit the plasma parameter β of a discharge. Measurements on ASDEX Upgrade show the following maximal β-values for two different types of NBI: for the tangential injection $\beta_N \approx 2.3$ (#11652, $t = 3.49s$, radius of tangency $R_T = 0.93m$) , and in case of the radial injection $\beta_N \approx 1.6$ (#11654, $t = 3.56s$). Measurements

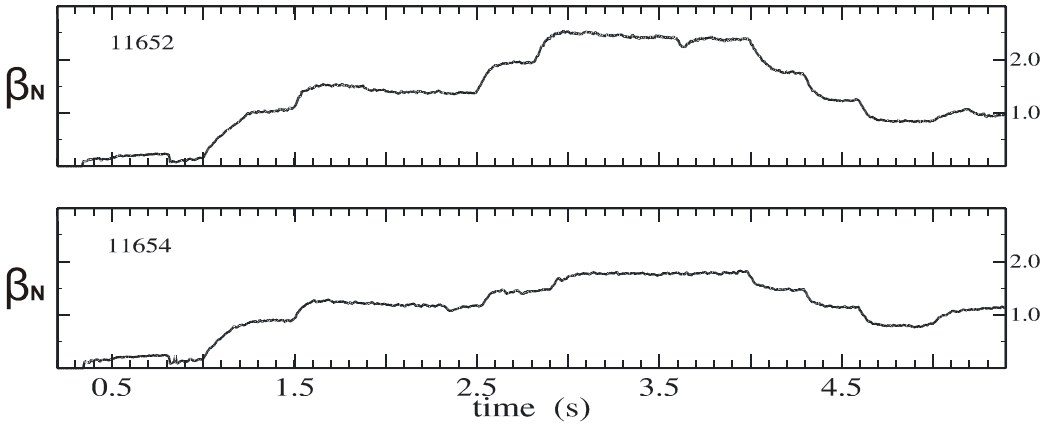

Figure 5.6: Normalized beta for radial (#11654) and tangential (#11652) injection cases.

of the normalized beta β_N for both discharges are shown in Fig.5.6. It is interesting to investigate the mode structure in these two cases.

The MHD analysis starts from the magnetic signals for radial (see Fig.5.7) and tangential (see Fig.5.8) injection cases. Both cases show a $(1,1)$ helicity of the MHD activity and are supposed to be similar to the internal kink mode. Thus, the parametrized function from the previous section (Eq.5.1) can be used here too. Varying the form of the eigenfunction, good agreement with the experiments was found. Optimized parameters for the displacement eigenfunction ξ_{kink} in case of the radial neutral beam injection are following: $a = 0.238$, $b = 1$, $c = 3$, $d = 0$, $r_{res} = 0.33$, $r_1 = r_{res} - 0.16$. For the tangential injection case the coefficients are different ($a = 0.129$, $b = 1$, $c = 3$, $d = 0.11$, $r_{res} = 0.30$, $r_1 = r_{res} - 0.09$). These eigenfunctions are shown in Fig.5.9.

Comparison of the FFT amplitudes and the SVD components with the corresponding experimental results for these eigenfunctions are presented in Figs.5.10 , 5.11 , 5.12 , and 5.13. One can see that the simulations fit well to the experimental curves. This means that our eigenfunctions describe all main features noticeable by the SXR diagnostic.

For the radial injection case our eigenfunction from the SXR data has an ideal kink mode character (rigid displacement of the plasma inside the $q = 1$ surface as was shown in Fig.1.4). The tangential injection case is more complicated. The main difference between these displacements is a small negative peak in the tangential injection case (see Fig.5.9). The existence

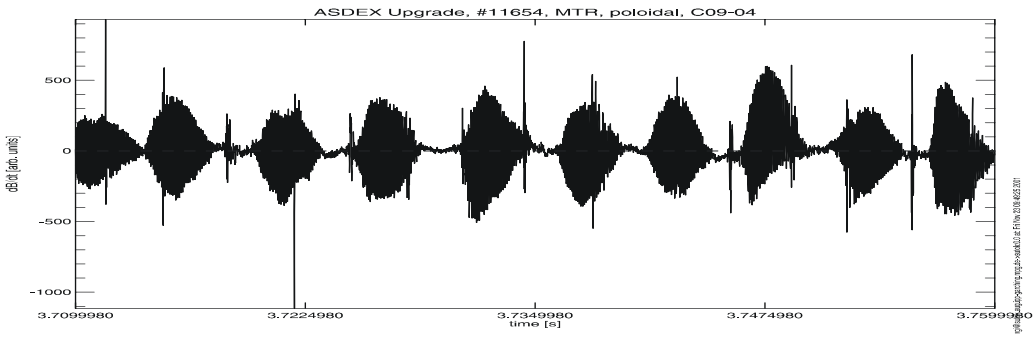

Figure 5.7: Magnetic signal of the fishbones in case of the radial injection (#11654).

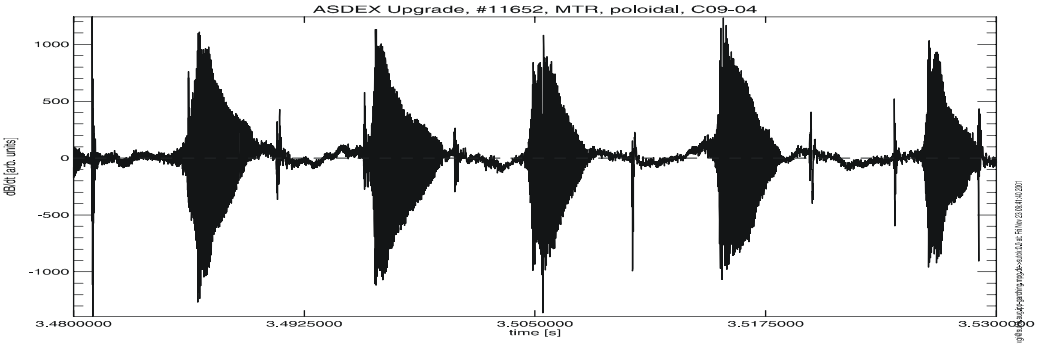

Figure 5.8: Magnetic signal of the fishbones in case of the tangential injection (#11652).

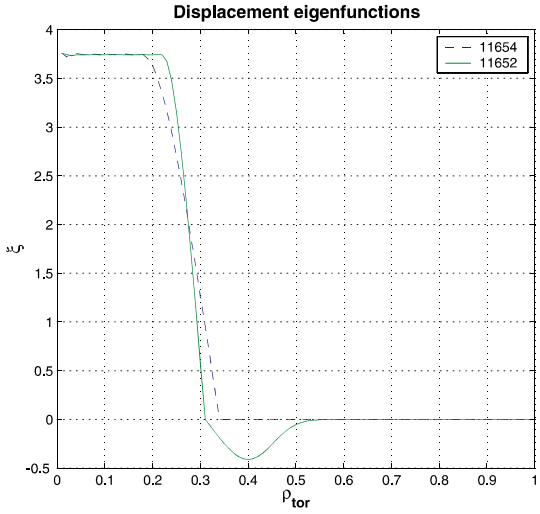

Figure 5.9: Forms of the displacement eigenfunction for the radial ($\#11654, t = 3.56s$) and toroidal ($\#11652, t = 3.49s$) injection cases.

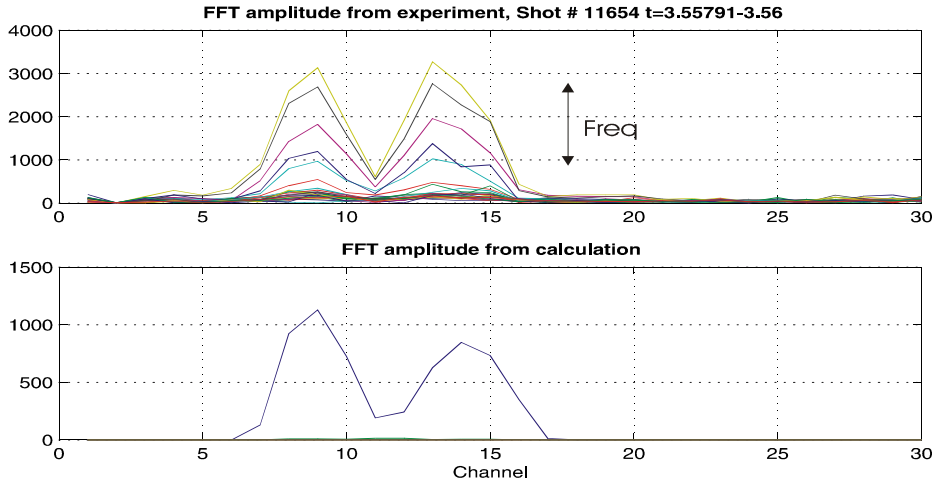

Figure 5.10: Comparison of the FFT amplitude for the radial injection case ($\#11654$).

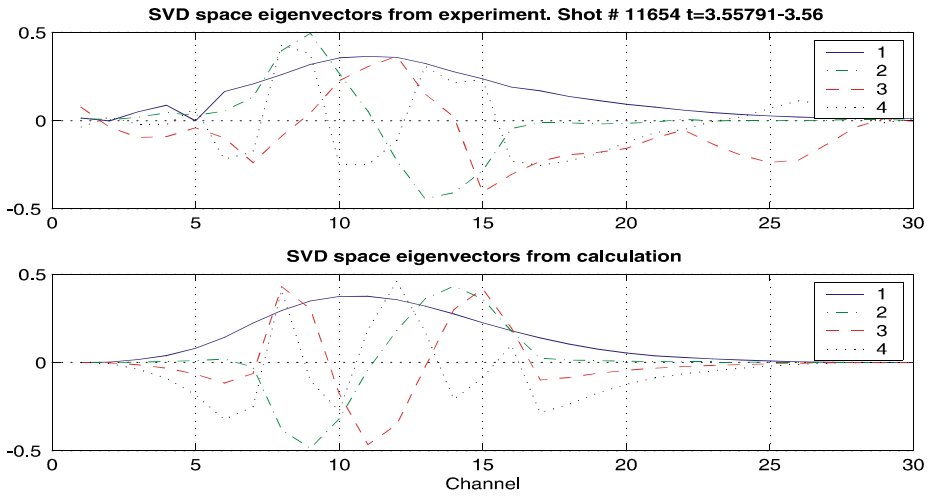

Figure 5.11: Comparison of the SVD components for the radial injection case (#11654).

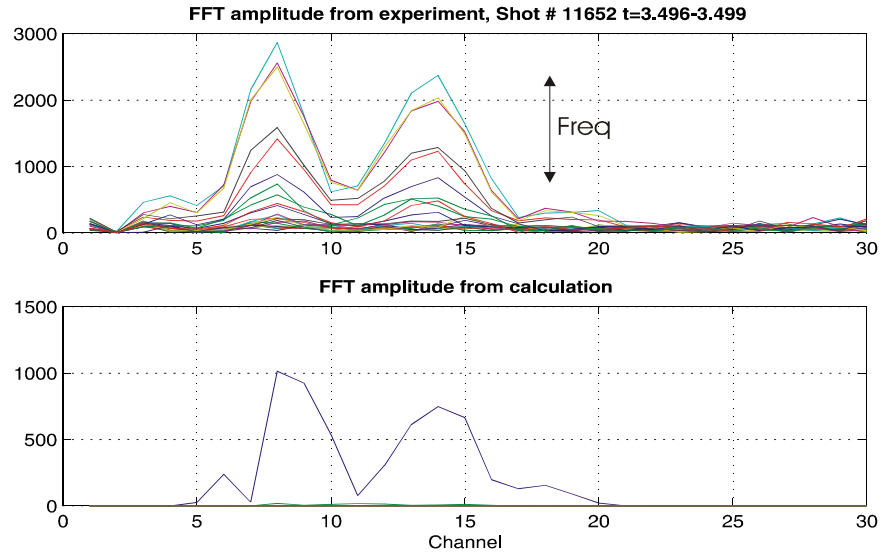

Figure 5.12: Comparison of the FFT amplitude for the tangential injection case (#11652).

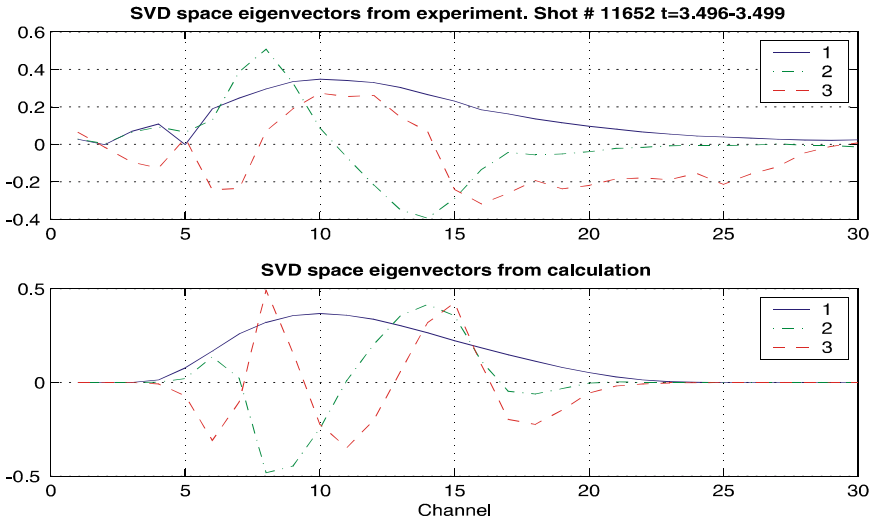

Figure 5.13: Comparison of the SVD components for the tangential injection case (#11652).

of this peak leads to changes of the FFT amplitude compared to the radial injection, and two additional small maximums appear on the curve in Fig.5.12. These, however, would also appear if the peak of the displacement had positive sign. The SXR data analysis cannot distinguish between these two cases. Thus, there are two different possibilities either the mode has resistive character and forms an island (negative peak), or the observation shows coupling to an additional mode (positive peak). To clarify the form of the eigenfunction, ECE measurements should be taken into consideration.

Displacement eigenfunctions from the ECE measurements are shown in Figs.5.14, 5.15. Both displacements are not symmetrical and have different characters on the low and high field sides. Thus, the ECE measurements demonstrate the coupling to higher m-numbers on the low field side of the torus for both cases of NBI. For the tangential injection case this coupling is higher due to higher β_N.This mode coupling is not observed by the SXR measurements. A possible explanation for this difference is that the observations were done by the B-camera directing at the plasma from the outer part of the torus (see Fig.2.2). The measurements from this position do not allow to test the ballooning character of the mode.

In order to proof the resistive character of the mode, one should plot the

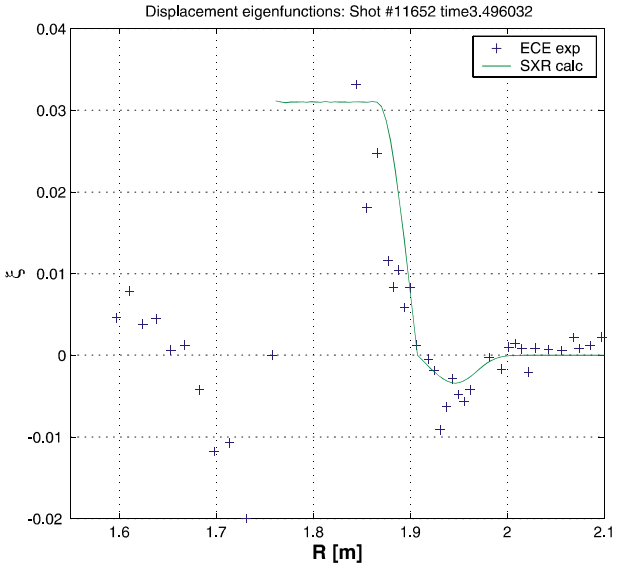

Figure 5.14: The displacement eigenfunction from ECE measurements together with the calculated one for the tangential NBI (#11652, t=3.5s).

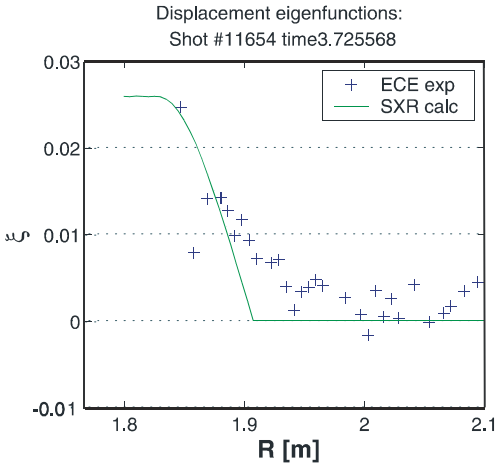

Figure 5.15: The displacement eigenfunction from ECE measurements together with the calculated one for the radial NBI (#11654, t=3.73s).

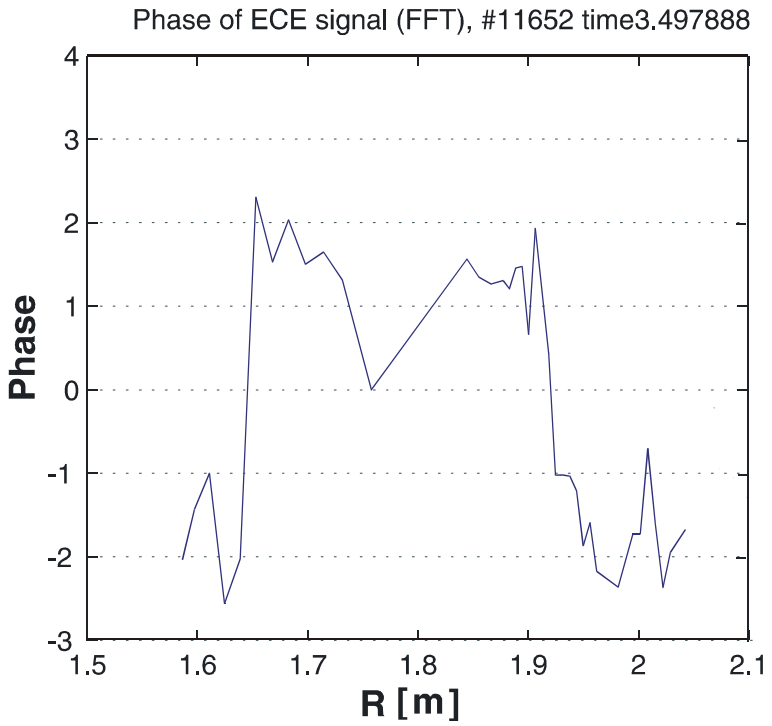

Figure 5.16: Phase jump of the ECE signal for the tangential injection case (#11652). Two phase jumps show position of the mode on the low field side ($R = 1.92m$) and on the high field side ($R = 1.64m$) of the torus.

FFT phase of the ECE signals at the mode frequency (a magnetic island would cause a jump of the FFT phase). The radial NBI case has no jumps (ideal character). The tangential NBI case has a resistive character (see Fig.5.16). Two phase jumps show position of the mode on the low field side ($R = 1.92m$) and on the high field side ($R = 1.64m$) of the torus.

In addition it is interesting to model the Mirnov measurements. The modeling of these measurements was done using parametrized expression for perturbation current (Eq.3.7) and applying the measured $(1, 1)$ helicity of the mode. Varying the form of the current J_{pert}, good agreement to the measured signals was obtained for the following parameters: $J_{\max} = 200$, $J_{\min} = -50$, $r_{res} = 0.3$, $W = 0.18$, $r_1 = 0$, $r_4 = 0.5$, $\alpha_1 = 2$, $\alpha_2 = 3$ (Fig.5.17). The observable amplitude of the perturbation from Mirnov measurements together with the corresponding calculations are plotted in Fig.5.18. The perturba-

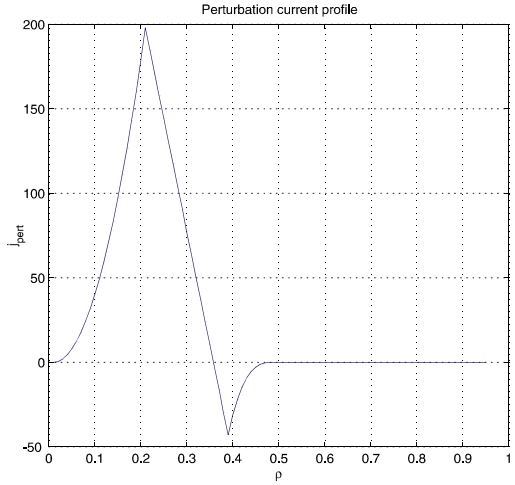

Figure 5.17: Dominant $(1,1)$ perturbation current component which is used to calculate the magnetic signal (see Fig.5.18) in the tangential NBI case $(\#11652, t = 3.5s)$.

tion current function J_{pert} shown in Fig.5.17 has a negative peak. This peak is an important part of the current which allows to include the influence of the plasma on the perturbation current. XTOR calculations also reproduce this behaviour of the perturbation current (see Fig.5.19). Consequently, assuming the correct form of the perturbation current we include influence of the plasma which is neglected in the MIC code (see Ref.[16]).

It is interesting to understand why the fishbones have different characters for tangential and radial NBI cases. Either the resistive character of the fishbones depends on the injection type or it is an influence of higher plasma β_N and therefore higher amplitude of perturbations in the discharge with tangential NBI. In order to check that, a fishbone burst for the tangential NBI case was analyzed for an earlier time point with $\beta_N \approx 1.4$. An ideal character of the mode for this time point was confirmed by the MHD analysis. Corresponding displacement eigenfunction and FFT amplitudes are shown in Figs.5.20-5.21. After analysis of several time points with different β_N parameter, it was found that the mode becomes resistive at the critical value of $\beta_{N,crit} \approx 1.7 - 1.8$.

Investigation of fishbones on ASDEX Upgrade by S.Günter et al.[59] shows that fishbones can give a much stronger effect on the plasma parame-

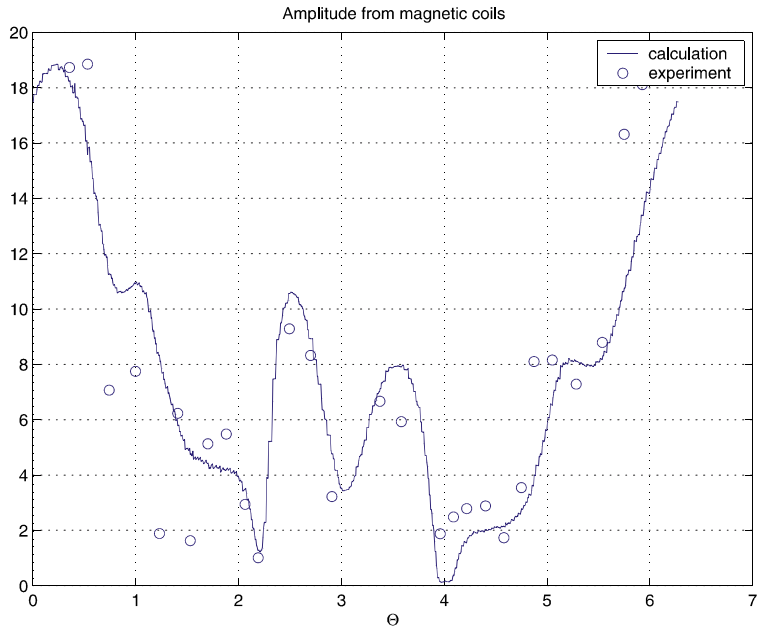

Figure 5.18: Amplitude from calculation (solid line) compared with magnetic signals from Mirnov coils (points) for the tangential NBI case ($\#11652, t = 3.5s$). The perturbation current for this case is shown in Fig.5.17.

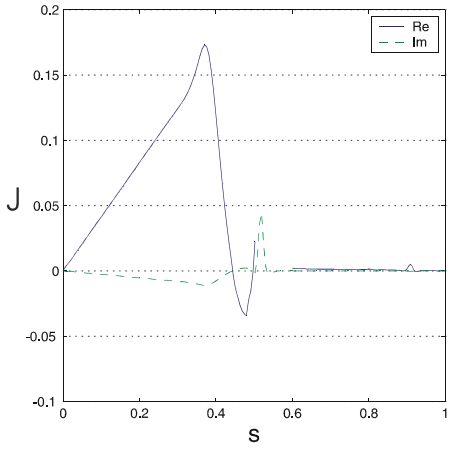

Figure 5.19: Profile of the perturbation current for dominant $(m, n) = (1, 1)$ component from the XTOR code.

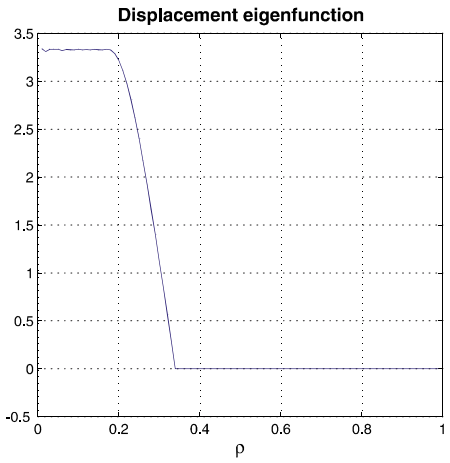

Figure 5.20: Displacement eigenfunction for the tangential NBI discharge ($\#11652, t = 2.46s$).

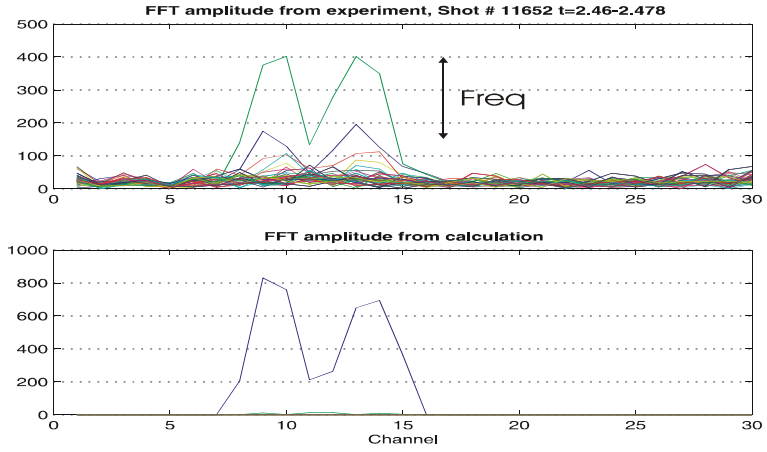

Figure 5.21: Comparison of the FFT amplitude for the tangential NBI case ($\#11652, t = 2.46s$).

ters than expected from an ideal instability. It was demonstrated from ECE measurements that the influence of a strong fishbone on the temperature profile is comparable with an effect of small sawtooth. Moreover, only the assumption of a resistive reconnection in the transport code ASTRA allows to explain the observed stationary current profiles with a central q values about unity in these discharges. Investigation of fishbones on JET also has shown the existence of the resistive fishbones [67].

In conclusion, from analysis of all available data related to the fishbones it follows that $(1,1)$ fishbones are coupled to the higher modes $(m,1)$ on the low field side of the torus (higher amplitude of the displacement eigenfunction) and the mode becomes resistive when $\beta_N \geqslant \beta_{N,crit} \approx 1.7 - 1.8$.

Chapter 6

MHD activities in advanced scenarios

The hollow plasma current profile which is characteristic for the advanced tokamak scenarios leads to flat or reversed q profiles as required for the formation of internal transport barrier (see Fig.4.1). These special form of the q-profiles gives rise to MHD phenomena not observed under conventional discharge conditions. These instabilities lead to significant limitations of the accessible operating regimes. The corresponding instabilities observed in ASDEX Upgrade reversed shear discharges will be investigated in this chapter. We start with a double tearing mode, then examine the time evolution of instabilities during the formation of internal transport barrier (ITB) and finally investigate MHD instabilities causing disruptions in this scenario.

6.1 Double tearing mode

The double tearing modes (DTMs) are characteristic MHD activities for reversed q-profiles in the advanced scenario. This mode can appear when two tearing modes with the same helicities (m, n) are coupled. The linear stability of double tearing modes has been previously studied [68, 69], as well as the non-linear stability [70, 71, 72, 73]. This mode was also found to be one of the possible type of MHD activity in advanced tokamak scenarios on ASDEX Upgrade [57, 74]. In this section we analyse in detail an observed DTM structure and estimate the growth rate of the mode.

A double tearing mode has two modes with the same helicity (same (m, n)

Figure 6.1: SXR signal from the B-camera for the $(2,1)$ double tearing mode (#12224, t=0.7s).

numbers), and thus the perturbation currents due to the inner mode are screened by the outer rational surface. In this case, a simulation of the magnetic measurements is not very helpful because of the screening effect of the outer surface. Thus, the magnetic measurements can be applied only to determine the helicity of the modes. Consequently, the interpretation of the SXR signals and the ECE signals is the only way to find the radial structure of this mode.

As an example we consider the mode activity in a reversed shear discharge of ASDEX Upgrade (#12224, t=0.7s), which will be shown to be a $(2,1)$ double tearing mode. The magnetic measurements show a $(2,1)$ mode activity. The SXR signal from the "B"-camera is shown in Fig.6.1. There is a "wave"-like structure close to the central region of the plasma which is very similar to that shown in Fig.3.9. This structure could correspond to an inner mode. A crude approximation for the position of an outer mode also can be found directly from Fig.6.1 and from the motional Stark effect measurements (MSE).

Theoretical investigations mentioned above predict the form of the dis-

placement eigenfunction using different assumptions and computational codes. Results from the XTOR give a shape of DTM displacement similar to the other calculations. This XTOR eigenfunction can be used as an initial guess for our calculations (see Fig.6.2). For a detailed investigation of the instability, the form of the perturbation ξ_{DTM} can be parameterized by the following function:

$$\xi_{DTM} = \begin{cases} \xi_0(r,a,b,c_1,d_1) & r < r_1 \\ g \cdot \xi_0(r,a,b,c_2,d_3) - \xi_0(r,a,b,c_2,d_3) & r_1 \leqslant r \leqslant r_2 \\ -\xi_0(r,a,b,c_1,d_2) & r > r_2 \end{cases} \quad (6.1)$$

$$r_1 = r_{res,1} + W/2, r_2 = r_{res,2} - W/2 \quad (6.2)$$

Varying the shape of the function, the best fit for experimental values was found for the following parameters: $a = 0.0345$, $b = 1$, $c_1 = 5$, $c_2 = 0.75$, $d_1 = 2$, $d_2 = 0.5$, $d_3 = 1$, $g = 2$, $r_{res,1} = 0.13$, $r_{res,2} = 0.47$, $W = 0.05$. Comparisons of the FFT amplitudes and the SVD components for this eigenfunction are shown in Figs.6.3 and 6.4 respectively.

The ξ_{DTM} function for this case together with q-profiles are given in Fig.6.5. From the shape of ξ_{DTM} it is clear that the investigated MHD activity is a $(2,1)$ double tearing mode with strong coupling between the two rational surfaces. The position of the outer mode from our analysis is in good agreement with the outer $q = 2$ surface according to the equilibrium reconstruction. For the inner mode no information can be gained from the MSE measurements. Fig.6.5 shows two q-profiles, which are both not in contradiction to the MSE measurements. Due to the reduced accuracy of the MSE measurements in the plasma center, it is not clear, whether an inner $q = 2$ surface exists at all.

ECE measurements are available over a large region of the plasma radius for this discharge (but do not include the inner mode). Thus, the radial displacement ξ_{ece} can be found from the temperature perturbation according to Eq.3.20. These measurements verify a strong coupling between the modes. The shape of ξ_{ece} is in quite good agreement with the calculated ξ_{DTM} from MHD-IC code (see Fig.6.6). Consequently *the MHD-IC code result agrees good with all available information about the plasma instability and the equilibrium reconstruction of the plasma.*

The calculated SXR signal from the code are quite sensitive to the actual shape of the eigenfunction, and thus a good agreement between measurements and calculated signals can only be obtained for a good fit to the

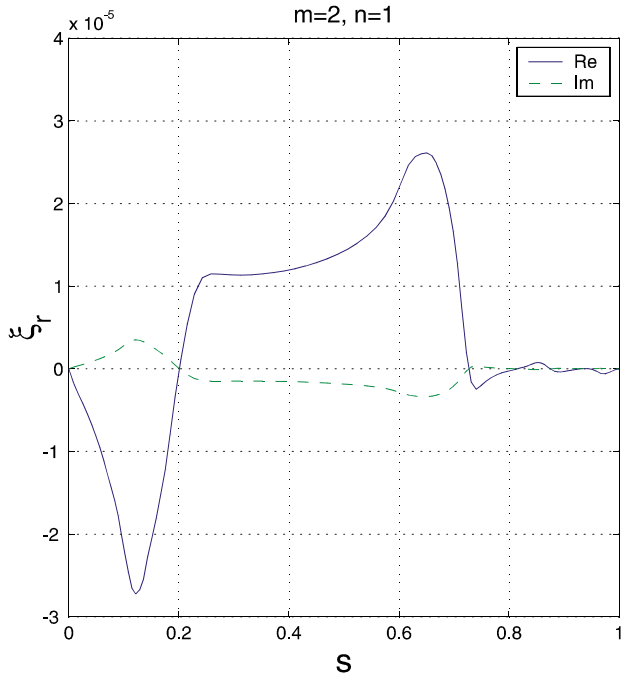

Figure 6.2: Dominant $(m, n) = (2, 1)$ component ξ_r for a double tearing mode resulting from the XTOR code.

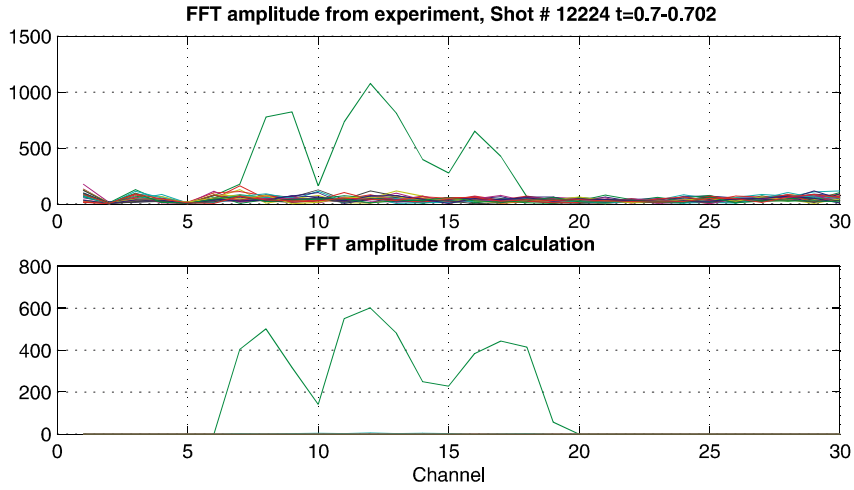

Figure 6.3: FFT amplitude for the same double tearing mode (see Fig.6.1).

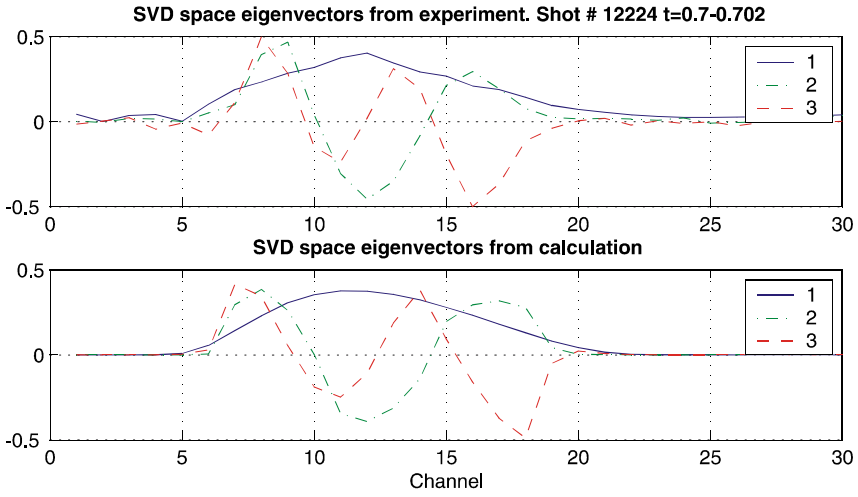

Figure 6.4: SVD eigenvectors for the double tearing mode (#12224, t=0.7).

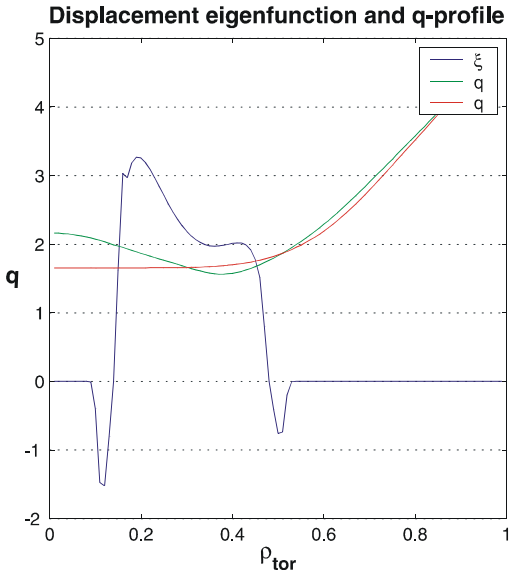

Figure 6.5: Displacement eigenfunction for the $(2,1)$ double tearing mode ($\#12224, t = 0.7s$) and two q-profiles resulting from the equilibrium reconstruction including the MSE measurements. Within the error bars, without considering the MHD activity, one cannot distinguish between these two profiles. On the other hand, including the MHD information improves the equilibrium reconstruction.

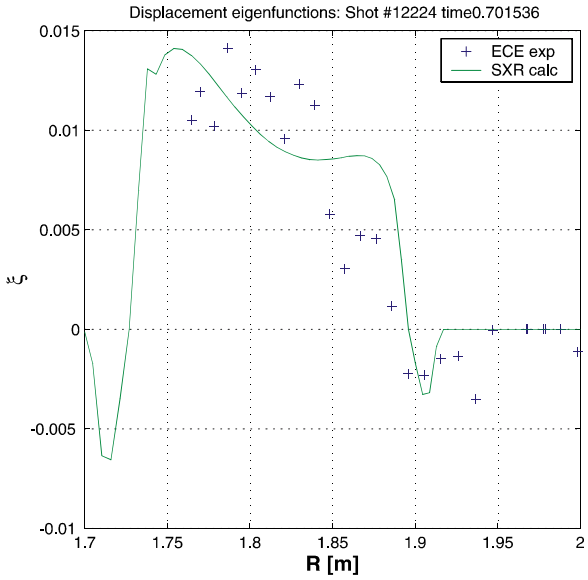

Figure 6.6: The displacement eigenfunction from ECE measurements together with the calculated one (#12224, t=0.7s).

actual eigenfunction. To proof this, we choose an eigenfunction with only a weak coupling between the resonant surfaces (Fig.6.7) and again perform the analysis for the same discharge (Figs.6.8 and 6.9).

It becomes obvious that for this profile of ξ the calculation results are in contradiction to the experiment. Thus, *the code results are very sensitive to the form of the displacement eigenfunction* ξ.

The double tearing mode example shows that a reconstruction of the displacement eigenfunction in complicated cases requires all experimental information. In our case magnetic measurements determine the helicity of the mode, SXR data are used to find the shape of the displacement, ECE data provide the absolute value of the displacement and MSE measurements give a first approximation for the outer mode position.

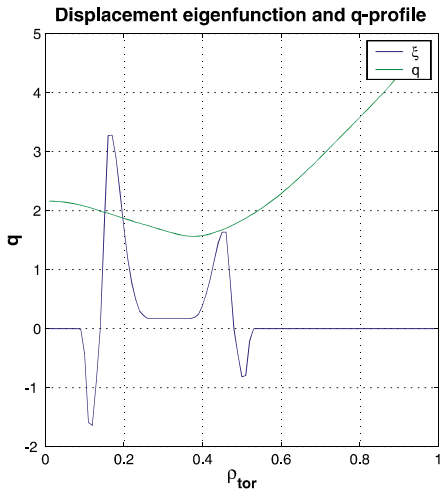

Figure 6.7: Displacement eigenfunction in case of weak coupling between the resonant surfaces together with the measured q-profile (MSE).

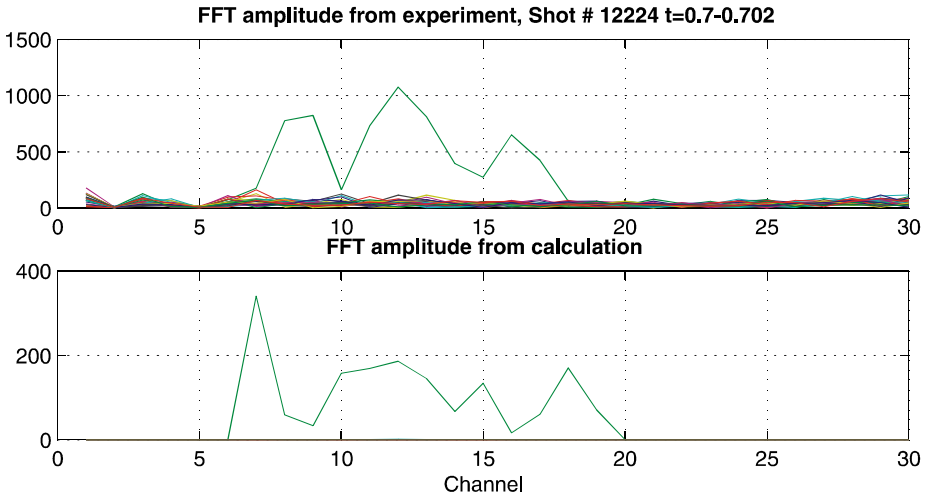

Figure 6.8: FFT amplitude calculated for the weak coupling case together with the FFT of the measured SXR signal.

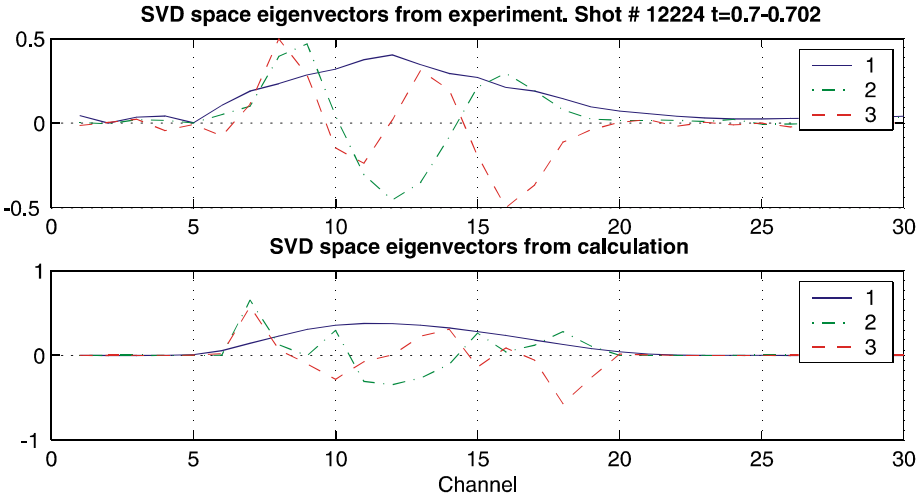

Figure 6.9: SVD eigenvectors for the weak coupling case together with experimental ones.

6.1.1 Determination of "delta prime" parameters of the double tearing mode

As was noted before, tearing modes change the magnetic topology in the plasma and form islands. A so-called Δ' formalism was developed to describe tearing mode behaviour [75, 76]. This formalism allows to determine the stability of a given current profile to tearing modes without solving the resistive MHD equations (1.3 - 1.8). This approach solves a differential equation for the perturbation flux function ψ in the "outer region" (in this region resistivity and inertia are negligible and the perturbed plasma is in force equilibrium) and matches the solution through the "resistive layer" where the resistivity becomes important. The discontinuity across this "resistive layer" determines the stability of the mode and is defined as:

$$\Delta' = \frac{\psi'(r_s + \varepsilon) - \psi'(r_s + \varepsilon)}{\psi\,(r_s)} \qquad \varepsilon \to 0\ ,$$

where r_s is resonant surface. For finite island size, the perturbed flux ψ assumes to be a constant inside the island and the discontinuity is taken between the inner and the outer island edges. The discontinuity Δ' depends on the island width W and generally decreases as the island width grows.

Calculation of Δ' is a difficult task in practice due to inaccuracy of the measured current profile. Stability corresponds to $\Delta' \leqslant 0$. Instability occurs for $\Delta' > 0$ and the island growth can be estimated using Rutherford's equation

$$\frac{dW}{dt} = 1.22\frac{\eta}{\mu}\Delta'(W) \ ,$$

where η is the plasma resistivity and μ is the magnetic permeability. This Δ' parameter is calculated below for the double tearing mode (DTM) from the displacement eigenfunction ξ_{DTM}.

In case of two rational surfaces, the Δ' formalism has been developed in Ref [68, 69, 77]. There are three different "outer" regions inside the plasma: Region I: $0 < r < r_1$; Region II: $r_1 < r < r_2$; Region III: $r_2 < r < r_{wall}$ where r_1 and r_2 are the inner and outer rational surfaces, respectively. Then, the tearing mode equation is solved in these three regions:

$$\left[\frac{\partial^2}{\partial r^2} + \frac{1}{r}\frac{\partial}{\partial r} - \frac{m^2}{r^2} - \frac{(\partial J_0/\partial r)}{(\partial \psi_0/\partial r)}\right]\psi_{m,n} = 0 \ ;$$

$\psi_{m,n}$ corresponds to the perturbed helical flux function, J_0 is the equilibrium plasma current and ψ_0 describes the equilibrium helical flux function defined as

$$\psi_0(r) = B_0/R_0 \int_0^r (1/q(r) - n/m) r dr \ .$$

These tearing mode equations use the approximation relations for small islands. However, in Ref.[77] it was demonstrated that the approximation is quite good for island sizes up to $10 - 20\%$ of the minor plasma radius. Consequently, this model should be sufficient to describe the DTM in our case.

The basic functions can be assumed to be independent, but strongly coupled eigenmodes. Then, the growth of each of the modes (islands) is dependent on Δ'_1 and Δ'_2. These discontinuities are defined by following equations:

$$\begin{aligned} \Delta'_1 &= \left(\partial\psi_1^-/\partial r - \partial\psi_1^+/\partial r\right)/\psi_1 + \left(\partial\psi_2^+/\partial r\right)/\psi_1 \mid_{r=r_1} \\ \Delta'_2 &= \left(\partial\psi_2^-/\partial r - \partial\psi_2^+/\partial r\right)/\psi_2 + \left(\partial\psi_1^-/\partial r\right)/\psi_2 \mid_{r=r_2} \end{aligned} \qquad (6.3)$$

The superscripts $(+/-)$ correspond to the inner and outer edges of the islands. The indexes $(1/2)$ describe the inner and outer modes respectively.

To estimate these perturbation fluxes from the DTM displacement eigenfunctions the following equation is used [37]:

$$\psi(r) = \xi(r) B_\theta (1 - q(r)/q_{res}) \ , \tag{6.4}$$

where B_θ represents the poloidal component of the magnetic field and q_{res} is q-value at the resonant surfaces. Then, the flux derivative reads

$$\psi'(r) = \xi'(r) B_\theta (1 - q(r)/q_{res}) - \xi(r) B_\theta q'(r)/q_{res} \ . \tag{6.5}$$

The improved equilibrium reconstruction with two rational surfaces $q_{res} = 2$ (see Fig.6.5) is applied to evaluate the $q(r)$ profile and its derivative. Since Eq.(6.4) is valid only outside of the islands, the perturbation fluxes inside the island were evaluated as a simple averaging of the boundary fluxes:

$$\psi(r_{res}) = \frac{\psi(r_{res} - W/2) + \psi(r_{res} + W/2)}{2} \ .$$

The resulting values for the "delta prime" parameters are following:

$$\begin{aligned} \Delta'_1 &\approx 33 \div 55 \\ \Delta'_2 &\approx 6 \div 11 \\ r_1\Delta'_1 &\approx 5.0 \div 7.2 \text{ and } r_2\Delta'_2 \approx 3.0 \div 5.6 \end{aligned}$$

The last parameter $r_{res}\Delta' \approx 5$ is the same for both modes (inside the error bars of the measurements). This is reasonable as $r_{res}\Delta'$ determines the mode's growth, and the two modes grow together.

6.1.2 Growth rate of the double tearing mode

The "delta prime" parameter shows that the double tearing mode (DTM) is unstable ($\Delta' > 0$) and the mode has a positive growth rate. This growth rate was calculated by the linear MHD code CASTOR[1] for the real experimental geometry and the measured plasma parameters of the discharge ($\#12224, t = 0.7s$). Equilibrium was calculated using equilibrium code DIVA [78, 79]. The CASTOR calculation results give the following growth rate for the $(2,1)$ DTM: $\gamma = 3027s^{-1}$.

At the same time, the growth rate of the double tearing mode can be estimated directly from the "delta prime" parameter by assuming the linear

[1] A brief description of the CASTOR code is done in Appendix C.

MHD approximation for DTM. Hence, each of the modes should have the growth rate [68, 77]:

$$\gamma \approx 0.5\,(\Delta' a)^{4/5}\,(ka)^{2/5}\,\tau_A^{-2/5}\tau_R^{-3/5}\ , \tag{6.6}$$

where τ_A is the Alfvén time, τ_R is the resistive time, k is the wave vector. This limit of the linear MHD analysis treats the growth of these two tearing modes independently but at the same time they are coupled [68]. One should note however that this approximation is valid only if the mode growth is much slower than the flux diffusion time across the tearing layer (so called "constant ψ" approximation):

$$\gamma\tau_\Delta \ll 1\ .$$

The resistive current diffusion time for the tearing layer reads

$$\begin{aligned} \tau_\Delta &\equiv \tau_R x_T^2\ , \\ \text{where } x_T &\approx \left(\frac{\gamma\tau_A}{m^2 S}\right)^{1/4}\ , \end{aligned}$$

and the Lundquist number is $S \equiv \tau_R/\tau_A$.

Suppose the same values of the Alfvén time ($\tau_A = 0.266 \cdot 10^{-6} s$) and the resistive time ($\tau_R = 0.6995 s$) as in the CASTOR calculations, the following growth rates were found:

$$\begin{aligned} \gamma_1 &= 1.4 \cdot 10^3 \div 1.6 \cdot 10^3 s^{-1} \quad (\gamma_1\tau_\Delta \simeq 0.015 \ll 1) \\ \gamma_2 &= 3.2 \cdot 10^3 \div 5.6 \cdot 10^3 s^{-1} \quad (\gamma_2\tau_\Delta \simeq 0.006 \ll 1). \end{aligned}$$

These results are comparable with the CASTOR calculations ($\gamma = 3.0 \cdot 10^3 s^{-1}$) and agree well with the experimental growth rate ($\gamma \approx 1.8 \cdot 10^3 s^{-1}$) measured from the SXR signals and the magnetic measurements. In addition, the growth rate can be estimated from the linear scaling of DTMs [68]: $\gamma \approx S^{-1/3}\tau_A^{-1} \approx 3{\cdot}10^3 s^{-1} - 6{\cdot}10^3 s^{-1}$ (for the resistivity about $10^{-7} - 10^{-6} ohm{\cdot}m$), which coincides with other results.

It is interesting also to compare the form of the displacement eigenfunction from the MHD-IC code and from the CASTOR code. Unfortunately, the equilibrium code instead of the q-profile has the current profile as an input parameter. Thus, it is difficult to construct the q-profile in the CASTOR calculations with exactly the same positions of the $q = 2$ surfaces as was found

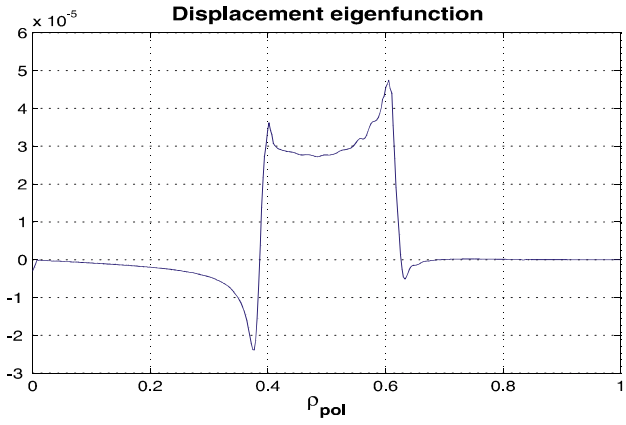

Figure 6.10: Dominant $(m, n) = (2, 1)$ component of the displacement eigenfunction from the CASTOR code. The calculation was done for the discharge #12224 conditions.

before. Nevertheless, the main features of the displacement eigenfunction remain the same (see Fig.6.10).

A determination of the growth rate from the displacement eigenfunction from the MHD-IC code with better accuracy is difficult due to the big error bars for the Δ' parameter, for the $q-$profile and especially for the derivatives $q'(\rho)$ and $\xi'(\rho)$. In addition, nonlinear affects also can play a role. However, the calculations demonstrate that a qualitative determination of the growth rate from experimentally observed displacement eigenfunction is possible even for complicated mode structures.

6.2 Evolution of MHD activities during internal transport barrier formation

It was found by S.Günter et al.[80] that in ASDEX Upgrade reversed shear discharges, the onset of internal transport barriers (ITBs) is typically accompanied by MHD activity. The observations show that an ITB onset usually occurs right after the first fishbone oscillations. This model states that the fishbone activity, located near the minimum q-value at its beginning, would trigger there the formation an ITB. Consequently, it is interesting to investigate the time behaviour of the displacement eigenfunction during an ITB

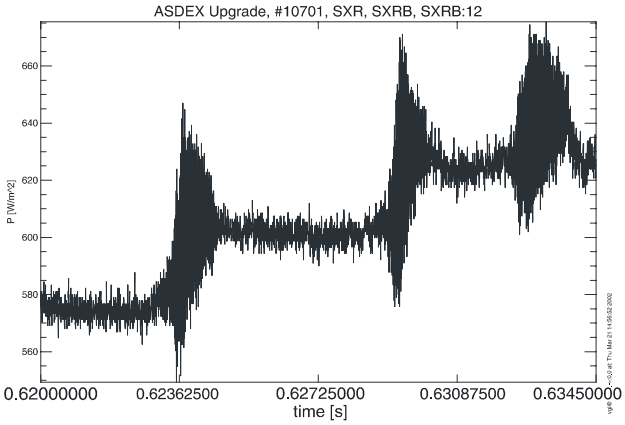

Figure 6.11: SXR signal during formation of internal transport barrier (#10701).

formation.

The instabilities during ITB formation are investigated below for the discharge #10701. Magnetic measurements observe a clear $(2, 1)$ structure of the mode. ECE and MSE measurements are not available for this discharge. The SXR signals increase after each fishbone oscillation during ITB formation (see Fig.6.11). An analysis of the SXR signals shows that the amplitude of the perturbation is small and it is not sufficiently large to determine an absolute value of the displacement. Nevertheless, the position of the modes and the shape of the displacement eigenfunction can be found with good accuracy using the FFT and the SVD technique from the SXR data.

To investigate the time evolution of the instability, corresponding displacement eigenfunctions were reconstructed for three different time points. The first point corresponds to a fishbone cycle at the beginning of ITB formation ($t_1 = 0.62s$), the second is in the middle of the process ($t_2 = 0.71s$), and the third one is at the end ($t_3 = 0.8s$). The resulting eigenfunctions in arbitrary units are shown in Fig.6.12.

Our analysis verifies a strong coupling between the modes, but the accuracy is not high enough to determine a resistive or an ideal character of the modes. One can see from Fig.6.12 that the distance between the modes grows during ITB formation. The inner resonant surface moves inwards and the outer surface goes outwards. Thus, our observations confirm this model.

It is interesting that in a similar discharge (#13149) MSE measurements

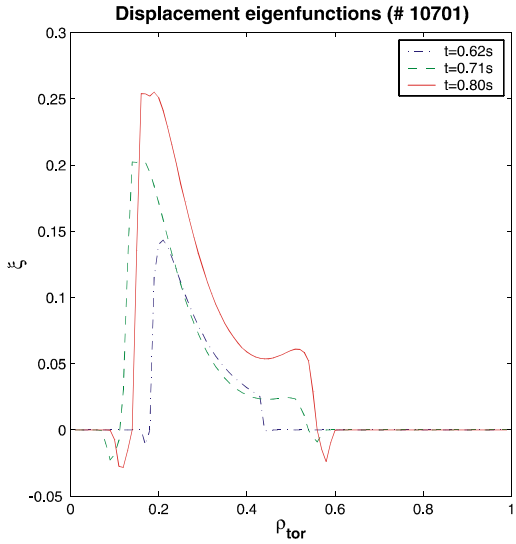

Figure 6.12: Time evolution of the displacement eigenfunction during internal transport barrier formation (#10701).

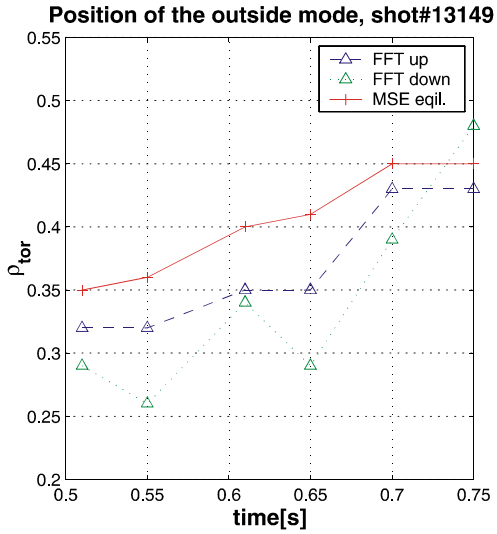

Figure 6.13: Position of the outer mode from FFT analysis ("FFT up" is from upper channels of B-camera and "FFT down" is from the down channels) and motional Stark effect (MSE) measurements.

confirm this behaviour of the resonant surfaces. Perturbations of SXR signals are even smaller for this discharge and only the position of the outer resonant surface can be estimated from SXR. These perturbations separated by the FFT transform and boundaries of the FFT amplitude gives the position of the outer surface (on lines of sights tangential to the outer resonant surface the FFT amplitude becomes zero). These data points together with the corresponding MSE measurements are shown in Fig.6.13. The behaviour of the outer mode is exactly the same as in the previous discharge.

6.3 Disruptions in discharges with internal transport barrier

"The tokamak disruption is a dramatic event in which the plasma confinement is suddenly destroyed. In a major disruption this is followed by a complete loss of the plasma current."[3] A typical disruption has the following steps: it begins from an initiating event (e.g. growth of MHD modes), this leads to a sudden thermal quench in which the plasma temperature drops down, and finally a current quench is occurred which completely destroys the plasma confinement [81, 82, 83]. The deatails of the disruption can be complicated, including nonlinear growth and coupling of several different MHD modes, but the main idea remains the same. Shrinking of the temperature profile (e.g. due to heat bridges across magnetic islands) leads to unstable current profiles which again drive instabilities [84]. These instabilities grow and influence on the temperature and current profiles. Finally, the plasma confinement is destroyed in a shot time and the plasma goes on the wall which produces large mechanical stresses and intense heat loads.

Since the first tokamak experiments, disruptions have limited stable tokamak operation. They also influence on tokamak's design which should not be destroyed by the large mechanical stresses and the heat loads. Only understanding of the basic disruption mechanisms allows to avoid these unfavorable events in the plasma. Thus, it is a particular interest to investigate reasons for disruptions in discharges with internal transport barrier (ITB) in advanced tokamak scenarios as for conventional scenarios they are already well investigated [85].

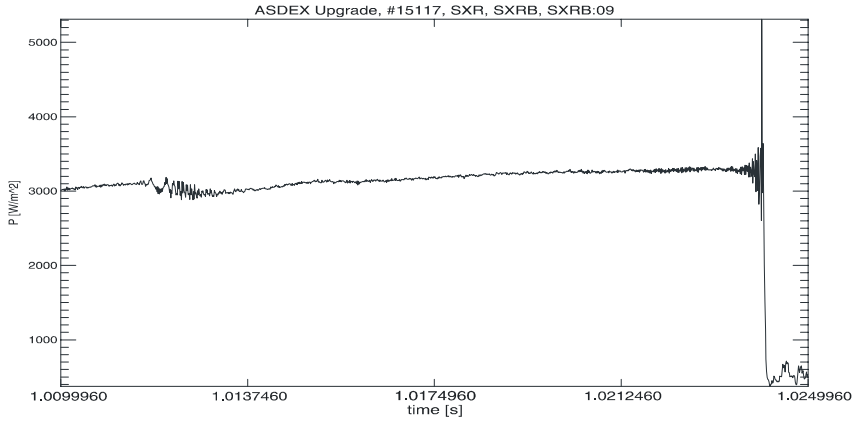

Figure 6.14: SXR signal from B-camera (#15117). Disruption corresponds to decrease of the signal ($t = 1.024s$).

6.3.1 Disruption due to external modes

As an example we investigate the disruption on ASDEX Upgrade in the ITB discharge #15117 ($t = 1.024s$). Fig.6.14 shows a time trace of the SXR signal for the B-camera. To understand the evolution of the plasma, the investigation of the MHD activities were done for two time points. The first time point corresponds to the MHD activity just before the disruption ($t = 1.01248s$) and the second time point during the disruption ($t = 1.024s$). The disruption occurs when $q_{95} \approx 4.08$.

At the first time point, SXR data show MHD activity in the plasma core inside $\rho_{tor} \approx 0.45$ (see Fig.6.15). Unfortunately, channel number 10 did not work during this discharge and the helicity of the mode is also undefined (no magnetic measurements). Thus, the form of the eigenfunction cannot be reconstructed by FFT and singular value decomposition technique and only the region of the activity have been found. The SXR cameras are more sensible to the core region of the plasma due to higher density and temperature in this region and cannot give adequate information about the plasma edge. The ECE measurements, on the other hand, often have density cutoff restriction in the plasma core and cannot resolve this region, but give unique information about other part of the plasma. The ECE measurements

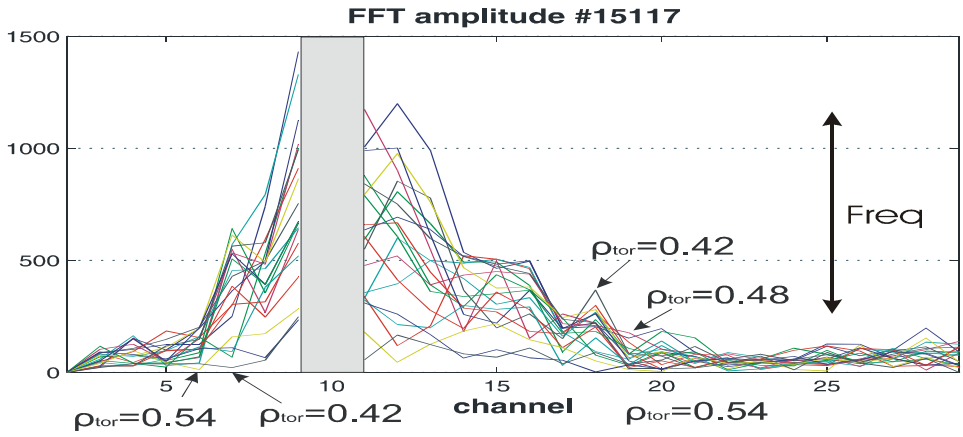

Figure 6.15: FFT amplitude for B-camera before the disruption (#15117, $t = 1.012s$). Channels 1 and 10 did not work during this discharge.

for this time point give a displacement eigenfunction of an external kink mode with a maximum amplitude on the plasma boundary of about $0.04m$ (see Fig.6.16). A coupling between the external kink mode and the MHD activity in the plasma core is not observed by our measurements.

Now we investigate the MHD activity during the disruption. The amplitude of the core activity becomes smaller since the FFT amplitude decreases at that time (see Fig.6.17). On the other hand, the amplitude of the external kink mode grows to $0.4m$. The displacement eigenfunction from ECE measurements during the disruption is shown in Fig.6.18. It is difficult to determine the exact amplitude of the displacement on the plasma boundary. Depending from the fitting procedure for $T_{0,0}$ in Eq.3.20, the amplitude of the displacement on the plasma boundary is varied between $0.3m$ and $0.5m$. This big amplitude of the external kink destroys the plasma confinement. Evolution of the temperature profile during the disruption (see Fig.6.19) shows the thermal quench which is typical for disruption events.

It was shown that the external kink mode causes the disruption in our case. This mode is the typical reason for disruptions in advanced scenario. On the other hand in a similar discharge (#15119) no disruption did occur, and only an internal collapse of the plasma happens. A possible explanation for that is the smaller value of $\beta_N \approx 1.9$ compared to the previous discharge #15117 with $\beta_N \approx 2.1$ (see Fig.6.20). Stability of external modes strongly

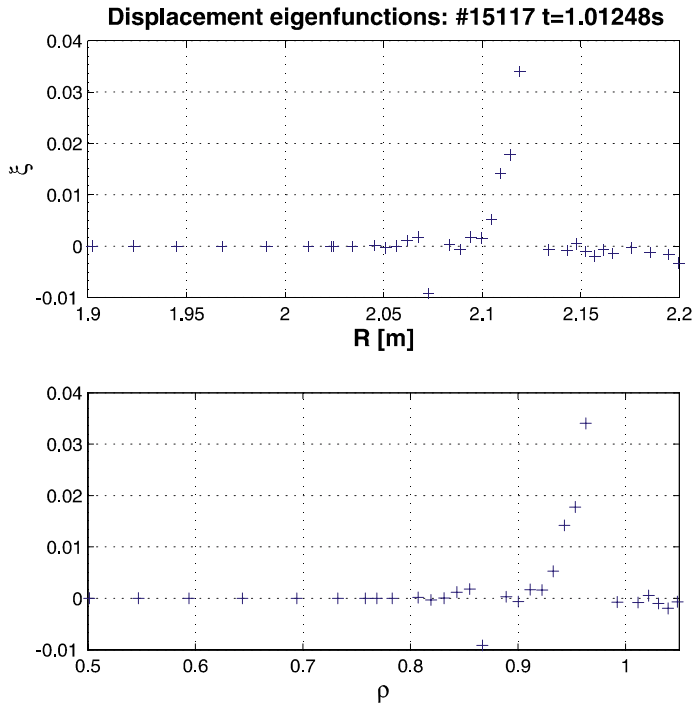

Figure 6.16: Displacement eigenfunction from ECE measurements ($\#15117, t = 1.01248s$).

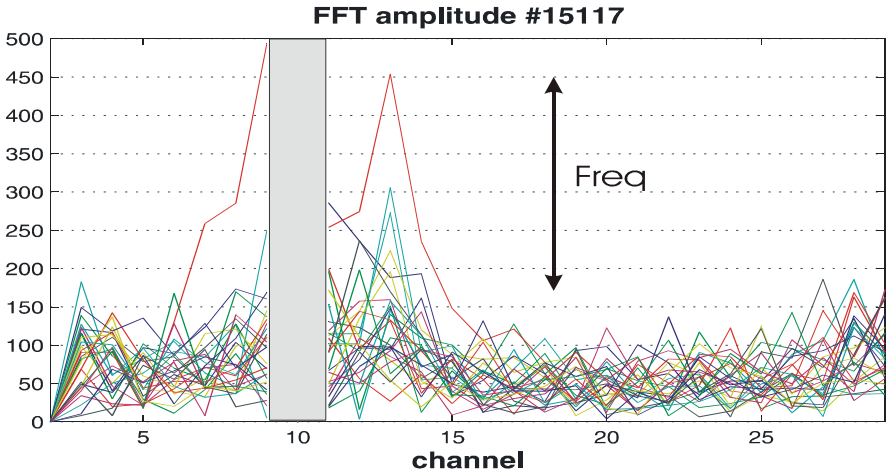

Figure 6.17: FFT amplitude for B-camera during the disruption ($\#15117, t = 1.024s$, Channel 10 don´t work).

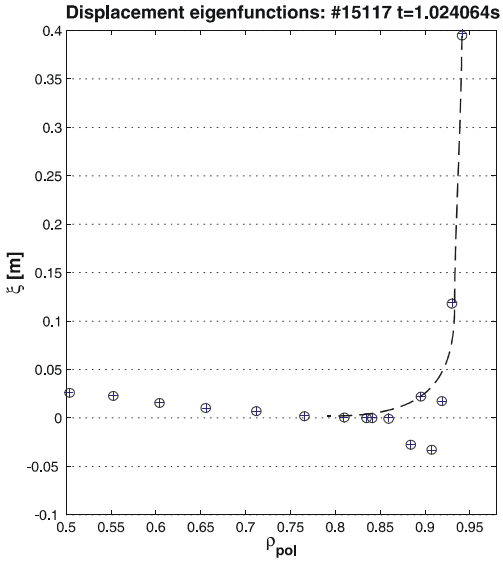

Figure 6.18: Displacement eigenfunction during the disruption $(\#15117, t = 1.024s, ECE)$.

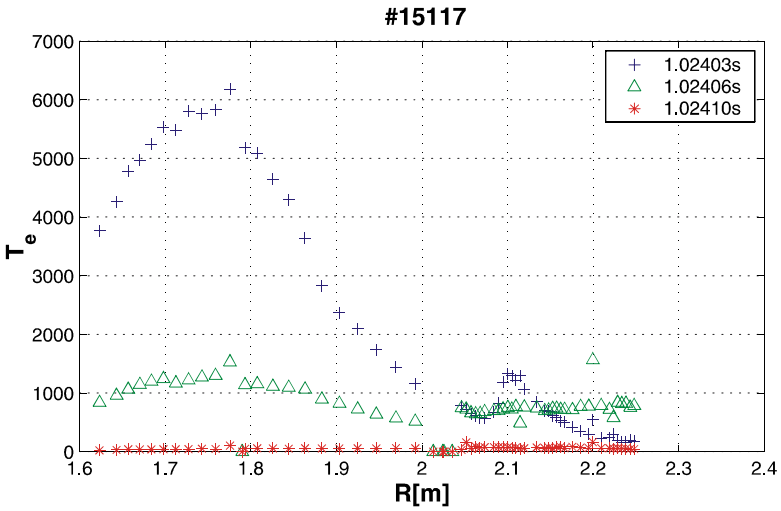

Figure 6.19: Temperature profile during the disruption for several time points (#15117, ECE).

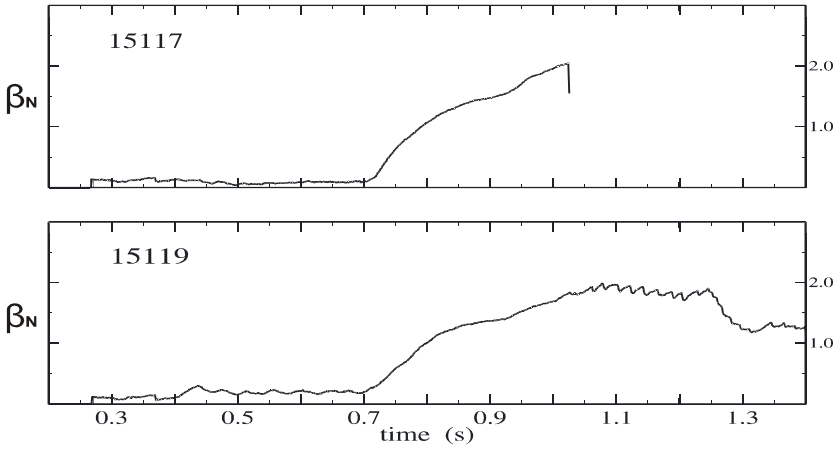

Figure 6.20: Normalize beta for discharges with disruption due to an external kink mode (#15117) and without (#15119).

depends on the plasma pressure, and higher β_N drives external kink mode unstable. Besides, the q-values at the plasma edge were also different for these discharges: $q_{95} \approx 4.4$ (#15119) and $q_{95} \approx 4.0$ (#15117). The higher value of the "safety factor" increases the magnetic shear, which leads to higher stability [86, 87]. Unfortunately, the quality of the MSE signals for these discharges is not sufficient to perform reconstructions of the q-profiles inside the plasma.

For an ideal external kink mode the growth time should be about the Alfvén time. This will be checked in the following: assuming exponential growth

$$\xi_{\max} = \xi_0 \cdot e^{\gamma_{\exp} \cdot \Delta t},$$

where $\xi_{\max}/\xi_0 \sim 40$ and $\Delta t \approx 3 \cdot 10^{-4} s$, then $\gamma_{\exp} = 14750 s^{-1}$. This experimental growth rate cannot be compared directly with the Alfvén time. In our discharge, β_N increases (see Fig.6.20) during the mode growth and influences on the growth rate of the mode [88]. Assuming continuous increase of β_N, $\beta_N = \beta_0 (1 + \gamma_h t)$, the experimental growth rate reads

$$\gamma_{\exp} \sim \left(\frac{2}{3}\right)^{2/3} \cdot \gamma_{mhd}^{2/3} \cdot \gamma_h^{1/3},$$

where γ_{mhd} is the growth rate of the mode without heating and γ_h is the heating rate (for this discharge $\gamma_h \approx 3.75 s^{-1}$). Consequently, the characteristic growth time of the mode τ ($\tau \approx 1/\gamma_{mhd} \approx 0.35 \cdot 10^{-7} s$) is about the Alfvén time ($\tau_A = a\sqrt{\mu_0 \rho}/B_\phi \approx 0.8 \cdot 10^{-7} s$). This fact demonstrates the ideal character of the instability.

An investigation of the reasons for disruptions in previous experiments on ASDEX Upgrade also show large amplitudes of external kink modes. Moreover, the ECE measurements detected a coupling of the external $(4, 1)$ kink mode to infernal $(2, 1)$ mode [74]. The resulting mode generally causes a disruption about $1ms$ after its onset due to the global character of the eigenfunction (see Fig.6.21). The stability analysis based on the equilibrium reconstruction using the MSE measurements, the kinetic pressure profiles and magnetic measurements lead to an eigenfunction which agrees very well with the corresponding displacement from ECE measurements. The other important difference is β_N-value (for discharge #12224, $\beta_N \approx 1.65 - 1.7$). The normalized beta is smaller for this cases. Consequently, the limiter discharge (#12224) has smaller stability compared to the separatrix discharges

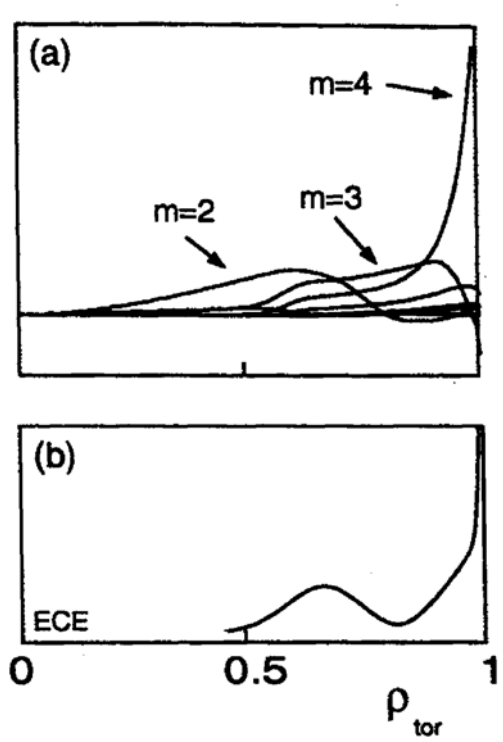

Figure 6.21: (a) Calculated and (b) measured (ECE) eigenfunctions for the mode activity causing the disruption in the discharge #12224 at about $1s$. The mode has a large amplitude at the plasma edge, indicating the coupling of the $(2,1)$ infernal mode to the $(4,1)$ external kink (this figure is from Ref.[74]).

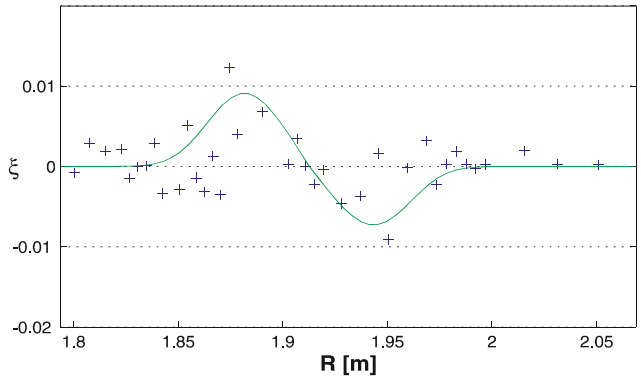

Figure 6.22: Displacement eigenfunction of an internal $(3,1)$ mode appears before the disruption (#15263, ECE measurements).

#15117 and #15119. This advantage of separatrix discharges compare to limiter discharges was also confirmed by CASTOR calculations in Ref.[89].

6.3.2 Disruption due to internal modes

The growth of an internal mode also may lead to disruption. An upper single null discharge #15263 is considered here. In this discharge a disruption occurs at about $1s$. Magnetic measurements detect $(3,1)$ mode activity before the disruption. This mode achieves an amplitude of about $1cm$ at the beginning (see Fig.6.22) and grows up to $5cm$ just before the disruption (see Fig.6.23). During the disruption, the amplitude of the displacement increases further and the form of the displacement is changed (see Fig.6.24). One peak of the displacement becomes much larger then the other. These changes are usual for non-linear evolution of tearing modes when the amplitude of its perturbation becomes large [90]. Nonlinear simulation of tearing modes in cylindrical geometry also verify this behaviour [35]. In our case, the displacement reaches a maximum amplitude up to $15cm - 20cm$ (about 30% of the minor plasma radius). This value is very big compared to typical internal modes with $max\,(\xi_0) \sim 3 - 5cm$ and brings to disruption by an upper vertical displacement of the plasma column (position of the plasma current was measured and shows the direction of the disruption). In the moment of the disruption the $(3,1)$ tearing mode grows to a large amplitude (see Figs.6.25, 6.24).

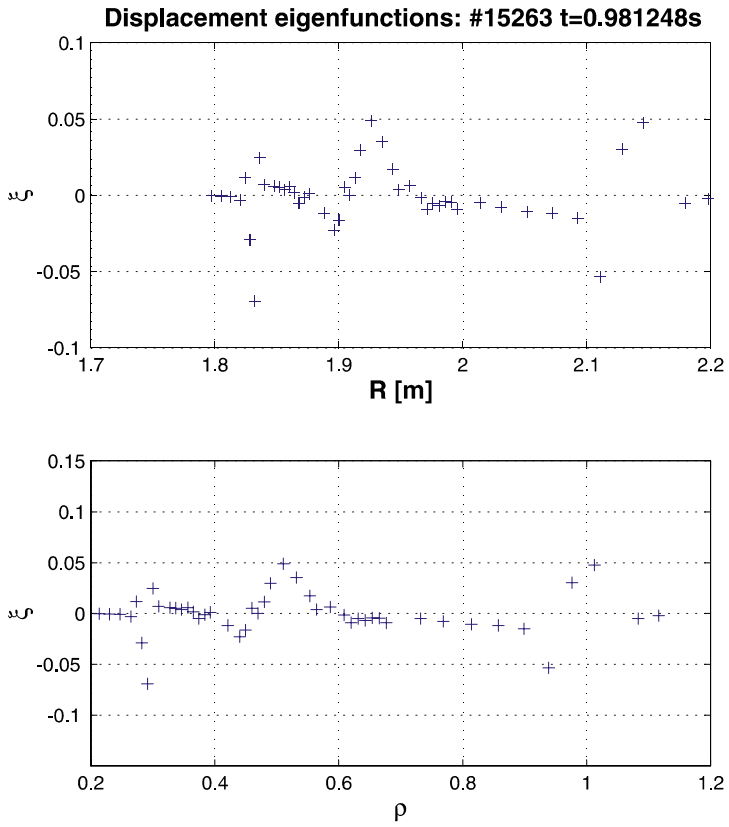

Figure 6.23: Displacement from ECE measurements just before the disruption (#15263). There is the well-marked $(3,1)$ mode at $\rho \approx 0.45 (R = 1.92m)$. Moreover, there is an inner $(3,1)$ mode at $\rho \approx 0.25\,(R = 1.83m)$. The both mode have resistive character which is confirmed by phase jumps of ECE.

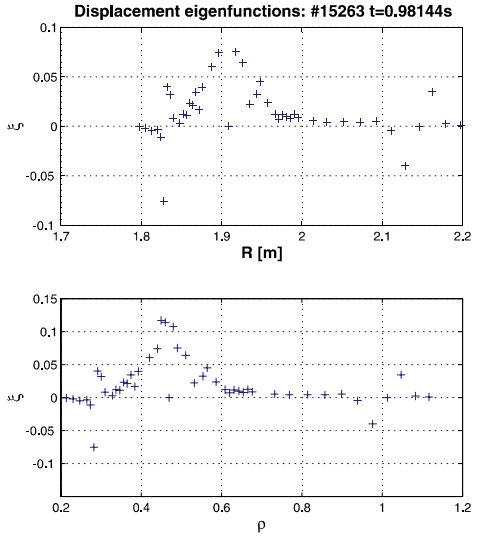

Figure 6.24: Displacement in the moment of the disruption measured by ECE (#15263).

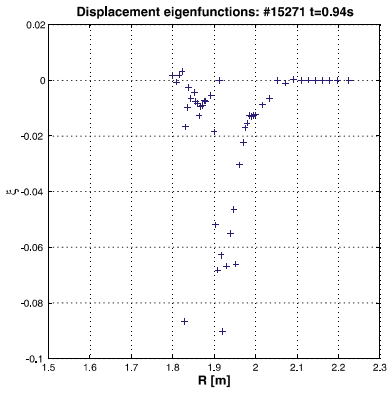

Figure 6.25: Displacement measured by ECE during the disruption (#15271).

It is interesting to note that the disruption due to the internal modes is much slower $t_{\#15263} \approx 1.2ms$ compared to the external mode disruption. This fact again demonstrates the resistive character of the $(3,1)$ mode.

Now we compare these discharges (#15271, #15263) with the previously described external kink mode case (#15117). The main difference between these two cases is the higher toroidal field B_ϕ, $B_{\phi(15271)} = 2.782[T]$ and $B_{\phi(15263)} = 2.788[T]$, for discharges with the (3.1) tearing mode compare to the external kink discharge: $B_{\phi(15117)} = 2.493[T]$. Since the q-value at the plasma edge depends from the toroidal field, $q_{95} \sim B_\phi/I_p$, and the plasma current I_p is practically the same, discharges #15271 and #15263 have larger q_{95} values compare to the external kink mode case (#15117). This would lead to higher values of the magnetic shear and can stabilize the external kink mode.

In addition, the MHD analysis also provides information about the shape of the q-profile just before the disruption. Since there is no $q = 2$ activity, the reversed shear q-profile should have $q_{\min}$ higher than 2. At the same time, there are two $q = 3$ surfaces at $\rho = 0.25$ and $\rho = 0.45$. These hints can be used for equilibrium reconstruction.

6.4 Possible improvements of the operation limits

In previous sections different types of MHD activity in advanced tokamak scenario were investigated. Thus, in order to extend the operation regime one should find a way to control these MHD instabilities. In general, investigations of ASDEX Upgrade reversed shear discharges have shown that the plasma confinement is limited by the following instabilities:

- Double tearing mode which appears due to coupling of two tearing modes with the same helicity
- Ideal external modes localized on the plasma boundary
- Internal $(3,1)$ tearing mode located on the middle of the plasma radius

In order to prevent the formation of the double tearing mode an optimized q profile has to avoid close double rational surfaces. Moreover, the shape of the q-profile should avoid the $(3,2)$ neoclassical tearing mode ($q_{\min} > 1.5$)

[74]. For these modification of the q-profile an active control of the current and pressure profiles is necessary. The ideal external kink can be stabilized by a conducting wall and a feedback system. At present, the wall is too far away from the plasma and cannot provide a sufficient stabilizing effect. All these possibilities to extend the operation limits are under discussion [74]. The internal $(3, 1)$ tearing mode appears as the reason for the disruptions in recent discharges with separatrix (Upper Single Null discharges). This mode has resistive character and is the subject of current investigations.

Chapter 7

MHD instabilities and equilibrium reconstruction

In this chapter we discuss additional benefits, which one can gain from the MHD analysis and note further steps in this direction.

An investigation of the MHD instabilities in the plasma is closely connected to the plasma equilibrium. The plasma equilibrium determines the shape of the q-profile. On the other hand, the MHD perturbations are easily excited only on the resonant surfaces ($q = m/n$) that are not covered ergodically by magnetic field lines. The analysis of the MHD phenomena using the MHD-IC code provides the displacement eigenfunction ξ and shows the position of rational surfaces in the plasma.

In a previous paper, the position of the $q = 1$ surface for the equilibrium reconstruction was obtained via detection of the $(1, 1)$ kink mode from SXR data [21, 91]. Our analysis is applied to improve the equilibrium reconstruction using arbitrary (m, n) mode structures. For instance, this improvement of the equilibrium reconstruction was shown for a double tearing mode in the previous chapter (see Fig.6.5). This betterment is especially important in the plasma core region where the large error bars of the MSE measurements do not allow for an accurate determination of the q-profile. Until now this type of analysis is the only opportunity to determine the position of the inner rational surface when ECE measurements do not exist in the core region due to the cut-off density restriction.

One typical example of the equilibrium reconstruction for the ITB discharge ($\#13149, t = 0.7s$) is shown in Fig.7.1. There are two different q-profiles in this figure. One is constructed using only the MSE measurements.

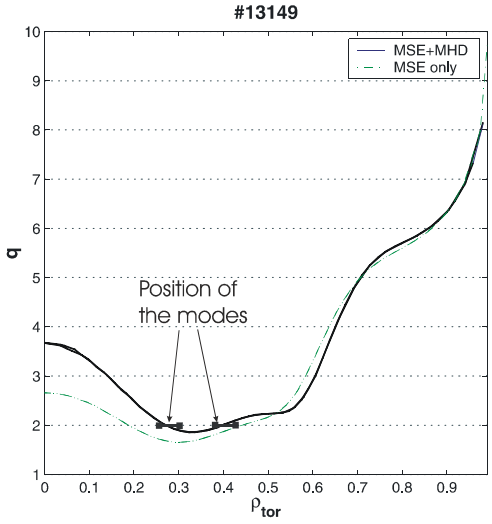

Figure 7.1: There are two different q-profiles (#13149). One is constructed using only the MSE measurements. The other applies also information about the position of the $q = 2$ surfaces derived from the MHD analysis.

The other applies also information about the position of the $q = 2$ surfaces derived from the MHD analysis (two $(2, 1)$ modes). Indeed, the inclusion the MHD information essentially influences on the q-profile. Such improvements of the equilibrium are intensively used and can be applied also for the old discharges without MSE measurements[1].

These betterment of the equilibrium reconstruction can be extended further. Using the measured displacement eigenfunction (SXR, ECE), it is possible to calculate the perturbation current. As the perturbation current following from this displacement and that derived from the Mirnov measurements have to agree, one finds information of the plasma equilibrium, mainly determining the magnetic shear at the rational surface. This is the subject of a further improvement of the code.

[1]Operation of the MSE diagnostic on ASDEX Upgrade was started from the discharge #10800 (7 channels) and was improved from the discharge #11800 (10 channels).

Chapter 8

Summary and Conclusions

The tokamak operation often is restricted by the growth of large scale MHD instabilities. They may lead to restrictions in operation regimes or even to disruptions (dramatic events in which the plasma confinement is suddenly destroyed). For their avoidance, it is of special importance to understand the reasons for their appearance. This can be gained either directly from the spatial structure and the time behaviour of the instabilities or from a comparison of the mode structure with theory. Unfortunately, for the complicated mode structures, the already available tools (tomographic reconstruction etc.) often cannot resolve the mode structure.

In this thesis, a new combined method for an investigation of the MHD activities in fusion experiments has been developed. The main advantages of this approach are the simultaneous use of several diagnostics (magnetic probes, soft X-ray cameras, electron cyclotron emission measurements and motional Stark effect measurements) and the possibility for a direct comparison of theory predictions with the experimental observations. This method has been implemented into the MHD Interpretation Code (MHD-IC). The code simulates the experimental observations related to a given plasma perturbation for the diagnostics mentioned above, accounting for real plasma geometry and for measured plasma parameters. Then the calculated values are compared with the corresponding experimental data. This algorithm simplifies the identification of the mode structures. In addition this procedure allows for a direct comparison with theory. As all available diagnostics are used simultaneously in the code, even the interpretation of weak MHD activity becomes possible. The developed method is much more powerful than the previously developed MIC code [16] which is restricted only to the magnetic

measurements. Moreover, the assumed profile of the perturbation current in the MIC code was too simplified to allow for reliable conclusions. As shown in chapter 3.2, the use of a realistic current profile is necessary and allows for a successful interpretation of the magnetic measurements. To demonstrate the power of the developed method it has been applied to different types of instabilities in various operation regimes of ASDEX Upgrade tokamak.

Thus, for example in chapter 5.2, fishbone instability was investigated in discharges with different angles of neutral beam injection and for different β_N values in conventional tokamak scenario. This fishbone instability occurs as a result of the resonance between the rotation of trapped fast particles from the injected beam and the toroidal wave velocity of the instability. It was demonstrated that the eigenfunctions have the form of ideal $(1,1)$ kink modes for low β_N values ($\beta_N \leqslant 1.7 - 1.8$) and get a resistive character for higher β_N values and thus higher driving forces. This result confirms the previous investigations [59] that fishbones can give a much stronger effect on the plasma parameters than expected from an ideal instability.

The main analysis efforts were focused however on more demanding examples of the more complicated mode structure in advanced tokamak scenarios. Unfortunately, the accuracy of standard techniques like tomographic reconstruction often is not sufficient to resolve the mode structures in these cases. It has been shown that our combined method of the analysis using the MHD-IC code however is able to give detailed information about the mode structure even in these more complicated cases.

The double tearing mode (DTM) is one of the characteristic types of MHD activity in advanced tokamak scenario. This mode can appear when two tearing modes with the same helicities (m,n) are coupled. As shown in chapter 6.1, the measured eigenfunction shows a strong coupling between the two rational surfaces, and agrees well with theoretical predictions. Another test of the applied method was the determination of the stability parameter Δ' as derived from the measured displacement eigenfunction. Comparing the growth rate resulting from this technique with the actual measured one as well as with that resulting from a theoretical stability analysis (using the CASTOR code) yields very good agreement. This example proves that even the details of the determined eigenfunction must be correct as the stability parameter Δ' is very sensitive to the actual shape of the perturbed vector potential at the rational surface.

The time evolution of MHD instabilities accompanying the formation of an internal transport barrier (ITB) was investigated in an advanced scenario

discharge in chapter 6.2. The displacement eigenfunction was reconstructed for several time points during this internal transport barrier formation. It was found that the MHD activity which accompanies the internal transport barrier formation (and probably triggers it [80]) locates around the minimum of the q-profile and consists of two coupled $(2, 1)$ modes.

A disruption is a dramatic event in a tokamak discharge in which the plasma confinement is suddenly destroyed. Thus, it is of particular interest to investigate reasons for the disruptions which often occur in advanced tokamak scenarios. The MHD activity causing a disruption was investigated in typical reversed shear discharges on ASDEX Upgrade in chapter 6.3. Detailed analysis demonstrates that there are two MHD modes which lead to disruption: an external kink mode with a maximum amplitude up to $0.3m - 0.5m$ during the disruption (#15117) and an internal $(3, 1)$ tearing mode with a maximum amplitude about $0.15m - 0.2m$ during disruption $(\#15236, \#15271)$. This analysis show that the external kink mode leads to disruptions when q-value at the plasma edge is small. Higher q-values provide a higher magnetic shear and can stabilize the external kink mode. In this case disruptions can occur due to the internal $(3, 1)$ tearing mode.

Additional benefits which can be gained from the MHD analysis are discussed in chapter 7. The structure and the position of the observed MHD phenomena have been used to improve the equilibrium reconstruction. In a previous paper, the position of the $q = 1$ surface for the equilibrium reconstruction was obtained via detection of the $(1, 1)$ kink mode from SXR data [91]. Our analysis is applied to improve the equilibrium reconstruction using arbitrary (m, n) mode structures. Since the safety factor $q = m/n$, and the MHD analysis provides information about the positions of MHD modes, we have a set of points for q-profile. For instance, this improvement of the equilibrium reconstruction was shown in chapters 7 and 6.1. This betterment is especially important in the plasma core region where the large error bars of the motional Stark effect measurements (MSE) do not allow for an accurate determination of the q-profile. Until now this type of analysis is the only opportunity to determine the position of the inner rational surface when electron cyclotron measurements (ECE) do not exist in the core region due to the cut-off density restriction. This is important to identify the reversed shear q-profiles in advanced tokamak scenario.

Further work

Future work will be focused on further improvements of the method and the investigation of new MHD phenomena. The first effect which will be implemented in the code is the toroidal coupling of (m, n) mode to $(m \pm 1, n)$ modes for a more accurate description of the eigenfunction. This part of the code is under development right now.

The next improvement will be related to the perturbation current. As was mentioned before, the measured displacement eigenfunction (SXR, ECE) completely describes the spatial structure of the MHD instability. As the perturbation current following from this displacement and that derived from the Mirnov measurements have to agree, one can find important information of the plasma equilibrium, mainly determining the magnetic shear at the rational surface.

Appendix A

ASDEX Upgrade parameters

Major plasma radius	R_0	$1.65m$
Minor plasma radius	a	$0.5m$
Plasma height	b	$0.8m$
Plasma elongation	$s = b/a$	1.6
Plasma aspect ratio	A	3.3
Plasma volume	V_{plasma}	$13m^3$
Total mass of the plasma protons		$2 \cdot 10^{21} = 3.3mg$
Plasma current	I_{plasma}	$2\ MA$
Discharge duration	t_D	$10s$
Plasma density	n_e	$\leq 3 \cdot 10^{20} m^{-3}$
Average plasma temperature	$T_i = T_e$	$5keV$
Heating power	$P\,[MW]$	$20_{(\text{NBI})}$, $5.7_{(\text{ICRH})}$, $1.6_{(\text{ECRH})}$

Cross-section of the ASDEX[1] Upgrade tokamak are shown in Fig.1.2.

[1] ASDEX means Axial Symmetric Divertor EXperiment.

Appendix B

Perturbation flux from a "step current" model

In this appendix we calculate a perturbation flux from a "step current" assumption and compare it with a perturbation flux from the tearing mode equation in cylindrical geometry.

The current perturbation due to a tearing mode is usually localized around the corresponding rational surface. The "step current" approximation assumes that the perturbation current flows only inside a thin cylinder (see Fig.B.1) and its value depends only on the poloidal angle

$$j = j_0 \cos(m\theta), \tag{B.1}$$

where m is the poloidal mode number. To be precise, we consider that the cylinder consists of small equal wires. Each of the wire has its own current according to Eq.B.1. The magnetic potential A_z for a single wire is:

$$A_z = -\frac{\mu_0 I}{2\pi} \ln \frac{r_*}{a} \ , \tag{B.2}$$

where r_* represents the distance to the wire and I is the current in the wire (see Fig.B.1). The magnetic potential of the cylinder results from integration over the poloidal angle:

$$\psi(r) = \frac{\mu_o}{2\pi} \int_0^{2\pi} j_o cos(m\theta) 2r_0 a \ln\left(\frac{\sqrt{r_0^2 + r^2 - 2rr_0 \cos(\alpha - \theta)}}{a}\right) d\theta \ . \tag{B.3}$$

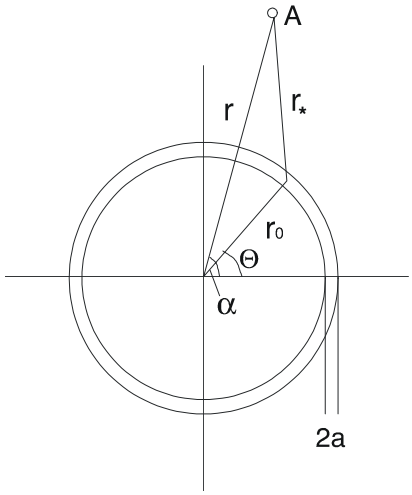

Figure B.1: "Step current" model. Perturbation current exists only in the narrow region and has angle variation proportional to $cos(m\theta)$.

In our case $\psi = -A_z$ and ${r_*}^2 = {r_0}^2 + r^2 - 2r_0 r\cos(\alpha - \theta)$. From B.3 it follows:

$$\psi(r) = \frac{\mu_o}{2\pi} j_o r_0 a \Big(2\int_0^{2\pi} \cos\ (m\theta)\ln(\frac{r}{a})d\theta + \int_0^{2\pi} \cos(m\theta)\ln(1+(\frac{r_0}{r})^2 - 2(\frac{r_0}{r})\cos(\alpha-\theta))d\theta\Big) \qquad \text{(B.4)}$$

The first integral is always equal to zero. Making the substitution $\gamma = \dfrac{r_0}{r}$ for the second integral [92]:

$$I = \int_0^{2\pi} \cos(m\theta)\ln(1+\gamma^2 - 2\gamma\cos\theta)d\theta = \qquad \text{(B.5)}$$

$$= \begin{cases} -2\pi\dfrac{\gamma^m}{m} & \text{if } \gamma^2 < 1 \text{ - outside region} \\ -2\pi\dfrac{\gamma^{-m}}{m} & \text{if } \gamma^2 > 1 \text{ - inside region} \end{cases} . \qquad \text{(B.6)}$$

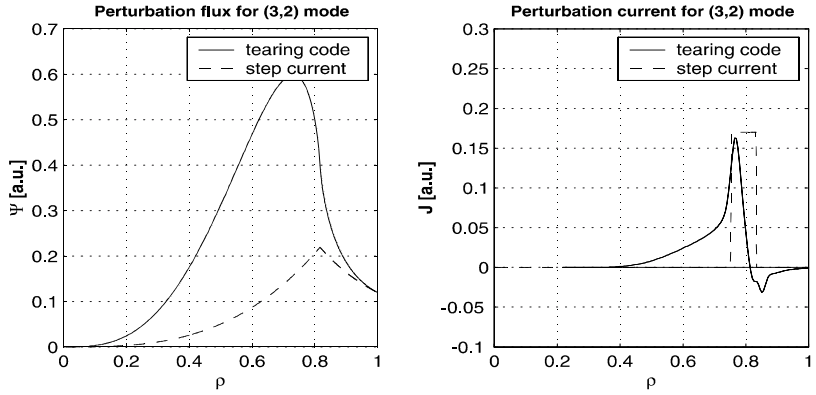

Figure B.2: Perturbation fluxes and perturbation currents for a $(3, 2)$ mode resulting from the tearing mode equation and from a "step function" assumption ($r_{res} = 0.81$). One can see the significant difference between the "step current" assumption and the tearing mode calculations.

Consequently, the resulting flux is the following:

$$\psi = \begin{cases} -\frac{\mu_0}{m} j_0 r_0 a (\frac{r_0}{r})^m & \text{outer region} \\ -\frac{\mu_o}{m} j_0 r_0 a (\frac{r_0}{r})^{-m} & \text{inner region} \end{cases} . \tag{B.7}$$

We demonstrate the difference between this assumption and a real perturbation current shape assuming that the perturbation flux at the plasma edge being the same. The perturbation fluxes from Eq.B.7 and from the solution of the tearing mode equation in cylindrical geometry have been evaluated for a $(3, 2)$ tearing mode. For a realistic current profile these fluxes as well as the perturbation currents are substantially different (see Fig.B.2).

The discontinuity Δ' of the flux function corresponds to the stability of the tearing mode [93]. This parameter is defined as: $\Delta' = (\psi'_+ - \psi'_-)/\psi(r_0)$, where ψ is the perturbation flux of the tearing mode. Instability occurs for $\Delta' > 0$. For the "step current" model this value is fixed and always smaller than zero: $\Delta' = -2m/r_0$. A real perturbation current has unequal positive and negative parts [94, 95]. Consequently, the "step current" model represents only stable tearing modes when the negative (or positive) part of the perturbation current is negligible. This yields that more careful treatment is necessary to interpret the magnetic measurements.

Appendix C

CASTOR and XTOR codes

In this section we briefly describe the CASTOR and XTOR codes. These codes represent two typical approximations applied to the MHD equations (1.3 - 1.8). The CASTOR code solves the linearized MHD equations and assumes the amplitude of the perturbations to be much smaller than the corresponding unperturbed quantities. The XTOR code solves the MHD equation directly. The results from both codes have been used in this work.

C.1 The CASTOR code

The CASTOR code was developed by W.Kerner and J.P.Goedbloed [96, 29]. Assuming the expansion $\vec{u}\left(\vec{x},t\right) = \vec{u}_0\left(\vec{x}\right) + \mathrm{Re}\{e^{\lambda t}\vec{u}_1\left(\vec{x}\right)\}$ for all variables in Eqs.(1.3 - 1.8) one can obtain the system of linearized resistive MHD equations [97]:

$$\begin{aligned}
\lambda\rho_1 &= -\vec{v}_0\cdot\nabla\rho_1 - \rho_1\nabla\cdot\vec{v}_0 - \vec{v}_1\cdot\nabla\rho_0 - \rho_0\nabla\cdot\vec{v}_1 \\
\lambda T_1 &= -\vec{v}_0\cdot\nabla T_1 - (\Gamma-1)T_1\nabla\cdot\vec{v}_0 - \vec{v}_1\cdot\nabla T_0 - (\Gamma-1)T_0\nabla\cdot\vec{v}_1 \\
\lambda\rho_0\vec{v}_1 &= -\rho_1\vec{v}_0\cdot\nabla\vec{v}_0 - \rho_0(\vec{v}_0\cdot\nabla\vec{v}_1 + \vec{v}_1\cdot\nabla\vec{v}_0) - \nabla\left(\rho_0 T_1 + \rho_1 T_0\right) \\
&\quad + \left(\nabla\times\vec{B}_0\times\vec{B}_1 + \nabla\times\vec{B}_1\times\vec{B}_0\right)/\mu_0 \\
\lambda\vec{B}_1 &= -\vec{v}_0\cdot\nabla\vec{B}_1 - \vec{B}_1\nabla\cdot\vec{v}_0 + \vec{B}_1\cdot\nabla\vec{v}_0 + \nabla\times\left(\vec{v}_1\times\vec{B}_0 - \eta\nabla\times\vec{B}_1/\mu_0\right) \\
\lambda p_1 &= -\vec{v}_0\cdot\nabla p_1 - \Gamma p_0\nabla\cdot\vec{v}_0 - \vec{v}_0\cdot\nabla p_1 - \Gamma p_0\nabla\cdot\vec{v}_1 \\
\lambda\rho_0\vec{v}_1 &= -\rho_0\left(\vec{v}_0\cdot\nabla\vec{v}_1 + \vec{v}_1\cdot\nabla\vec{v}_0\right) - \nabla\left(\rho_0 T_1 + \rho_1 T_0\right) \\
&\quad + \left(\nabla\times\vec{B}_0\times\vec{B}_1 + \nabla\times\vec{B}_1\times\vec{B}_0\right)/\mu_0
\end{aligned}$$

These equations are solved by the CASTOR code in a general toroidal geometry, where the equilibria are assumed to be axisymmetric. Consequently, the eigenfunctions are two dimensional.

C.2 The XTOR code

The XTOR [6, 7, 98] and CHEASE [30, 99] codes are applied to simulate MHD equilibrium and stability of tokamak plasmas. The CHEASE code calculates an equilibrium in toroidally symmetrical geometry with plasma cross-sections of arbitrary shape. XTOR uses the equilibria calculated by CHEASE to perform calculations of 3D MHD mode evolutions for a given number of toroidal and poloidal mode numbers including coupling between all of these modes. The XTOR code produces non-linear calculations involving the equilibrium $n = 0$ toroidal mode and employs for these calculations an efficient semi-implicit time-advance schemes [100]. This allows to carry full time simulations of various MHD phenomena in realistic tokamak plasmas.

Equations solved in the XTOR code are the following:

$$\begin{aligned} n\frac{\partial \vec{v}}{\partial t} &= ((\nabla \times \vec{B}) \times \vec{B} - \nabla p) - n(\vec{v} \cdot \nabla)\vec{v} + \nu \Delta \vec{v} \\ \frac{\partial \vec{B}}{\partial t} &= \nabla \times (\vec{v} \times \vec{B}) - \nabla \times (\eta \nabla \times \vec{B}) \end{aligned}$$

and

$$\begin{aligned} \frac{\partial T}{\partial t} &= -(\Gamma - 1)T\nabla \cdot \vec{v} - \vec{v} \cdot \nabla T + \nabla \cdot \chi_{\perp} \nabla T + \\ &\quad \vec{B} \cdot \nabla \left[\chi_{\parallel} \left(\vec{B} \cdot \nabla T \right) / B^2 \right] + H(\vec{r}) \\ \frac{\partial n}{\partial t} &= -n\nabla \cdot \vec{v} - \vec{v} \cdot \nabla n \end{aligned}$$

or

$$\begin{aligned} \frac{\partial p}{\partial t} &= -\Gamma p \nabla \cdot \vec{v} - \vec{v} \cdot \nabla p + \frac{1}{n} \nabla \cdot \chi_{\perp} n \nabla \left(\frac{p}{n} \right) + \\ &\quad \frac{1}{n} \vec{B} \cdot \nabla \left[\chi_{\parallel} n \left(\vec{B} \cdot \nabla \left(\frac{p}{n} \right) \right) / B^2 \right] + H(\vec{r}) \end{aligned}$$

where $H(\vec{r})$ is the heat source, $\chi_{\parallel}$ and $\chi_{\perp}$ are the parallel and the perpendicular transport coefficients respectively, and Γ is the adiabatic coefficient.

The user can choose either the pressure or separate density/temperature evaluation [100]. The current version of the code has been widely used in a variety of problems. The non-MHD effects were included lately in the code. Unfortunately, there are problems with the applied numerical scheme concerning these non-MHD effects.

The XTOR code was intensively used to simulate different types of MHD instabilities inside the plasma. The results of these numerical simulations are employed in the MHD-IC code as initial guesses for the displacement eigenfunction and the perturbation currents.

Appendix D

The MHD Interpretation Code

D.1 Applicability of the MHD-IC code

The MHD-IC code has been developed to investigate MHD activities in the ASDEX Upgrade tokamak in advanced and conventional tokamak scenarios, and for resistive and ideal modes.

The method allows to find the shape of the displacement eigenfunction even if the MHD activity is weak and this shape cannot be resolved by other methods (tomographic reconstruction etc.). Toroidal coupling to higher m-modes is not considered in the calculations so far.

In addition, the structure and the position of the MHD instabilities can be used to improve the equilibrium reconstruction of the plasma.

D.2 Installation and user guide

Introduction

The MHD-IC code is written in FORTRAN 90 and has about 13.000 lines. The code is constructed in a modular fashion which allows to change the programme easily. Results of MHD-IC calculations are stored in special ".dat" files and a set of MATLAB utilities has been developed to work with these results. The computation time for a single MHD-IC code run is about $6-7min.$ on an average SUN machine. Structure and approximations of the MHD-IC code were discussed in chapter three. In this section we describe how to install and use the MHD-IC code.

Installation

In order to install the code one should make the following steps:

- Create a directory for the code in the home directory, for example:

/codes/mhd_ic/

- Copy all files into this directory from the following subdirectory:
  ~vgi/codes/user_mhd_ic/

- Set a path to the directory and name of the operation system:

```
>setenv MHD_IC_HOME  ${HOME}/codes/mhd_ic
>setenv OBJECTCODE Solaris
```

- Finally, compile the MHD-IC code by typing:

```
>make
```

At the end an executable file named "mhd_ic.Solaris" will be created.

Input files

An input configuration file has name **inpXXX.cf**. The **XXX** represents a specific number of the input file. Each **X** has to be an integer between 0 and 9. In order to start the MHD-IC code, this input number is specified after the name of the executable file in the command line. For instance, if we have the input file "inp210.cf" type:

```
>mhd_ic.Solaris  210
```

Main parameters of the input files

These parameters should be specified in order to read shotfile information:

- Name of the experiment (1=AUGD, 2=AUGE, ...)
- Diagnostic (1=FPP, 2=EQU, 3=EQE)
- Shot number (12224, ...)
- Time (0.7, ...) in seconds
- Edition of the shotfile

Then we determine the plasma profiles and chose the type of MHD instability:

- Type of values for the plasma radius (1=ρ_{pol}, 2=ρ_{tor}).
- Use experimental profile for temperature and density (t=true, f=false)
- Type of instability (20=double tearing mode, 16=ideal $(1,1)$ kink, 161=resistive $(1,1)$ kink, 18=several uncoupled modes)
- Name of diagnostic for T_e profile (CEC,... the same as for jj-subroutines[1])
- Name of T_e profile (trad-a, ... the same as for jj-subroutines)
- Name of diagnostic for the density profile (CON=parabolic or the same as for jj-subroutines)
- Name of the density profile (ne, ... the same as for jj-subroutines)
- Rotation of the mode (should be true(=t) for simulation)
- Number of resonant surfaces

For each resonant surface one should specify following parameters:

- Poloidal mode number (m)
- Toroidal mode number (n)
- Frequency of the mode (only for several uncoupled modes, in other cases 1.0)
- Position of the resonant surface (ρ_{res} in flux coordinates, $\rho = 1$ on the plasma boundary)
- Width of the island (W)
- Phase (initial phase shift of the mode)
- Parameters for the perturbation current function J_{pert}

[1]These special subroutines were designed to read experimental profiles (author C.Fuchs). The latest version of a manual for these routines is available from WWW (http://www.ipp.mpg.de/common/jj/profile.html)

- first point of the current function (r_1 in Eq.3.7)
- first coefficient of the current function (α_1 in Eq.3.7)
- second coefficient of the current function (α_2 in Eq.3.7)

- Parameters of the temperature perturbation or the displacement eigenfunction $\xi_0(\rho)$ in Eq.3.1.
  - behaviour inside the island (b in Eq.3.2)
  - decrease outside the island (c in Eq.3.2)
  - relative amplitude of the peaks (d in Eq.3.2)
  - amplitude of temperature perturbation (as percentage of max. temperature)

IMPORTANT: *The ordering of the resonant surfaces should start from the most outside mode. All modes must be sorted in decreasing order of* ρ_{res}*!*

Data files

All information necessary for calculations are contained in special ".dat" files in subdirectory "data". For example, if one need to change the parameters of an SXR camera it can easily be done by changing information in one of these files.

Getting started

As far as you have the executable file and a correct input file you can start a calculation by typing

>mhd_ic.Solaris 210
>u
>ra=3

The last two commands are similar to the MIC code[32] and specify the type of the calculation for magnetic measurements. These commands choose a branch of calculations which include the influence of screening currents in internal vessel structures. At the end of the calculation all results will be written in ".dat" file in the "matlab_data" directory.

Modification of the code

It is possible to introduce various analytical functions with different number of parameters in order to describe an instability. Usually, the number of the parameters is big and not all of them are in the input file. Each user can

easily change the code and introduce a new displacement eigenfunction ξ_0 in Eq.3.1 (kink_SXR.f90) or current profile $J_{pert}(r)$(interp.f90). The faster way is to implement a new "case" construction with a new "type of the mode" number.

If one would like to read an equilibrium from a private shotfile it can be done by adding a new option in file "ggeo.f90". (Names of the input variables are written in "mic_io.f90".)

Matlab scripts

Since the FORTRAN 90 language is not adapted well for graphics, a set of MATLAB[2] scripts were developed to visualize the MHD-IC code results. These scripts can also work directly with experimental data. Two of these scripts are described here. Before using them one should change paths to the home directory in the source files ("vubor.m" and "sxr_vis.m"). These scripts read all information about plasma equilibrium and simulated MHD activity from ".dat" files in the "\matlab_data" subdirectory of the current working directory. Thus, one can also use the other software to analyse these data. In order to choose between ρ_{pol} and ρ_{tor} one should specified it in the input file of the MHD-IC code.

The first script "vubor" has been developed to plot profiles ($j_{pert}(\rho)$, $q(\rho)$, $\xi(\rho)$, ..), SXR lines of sight, perturbation fluxes and so on. The most important options allow to plot $\xi(\rho)$ (option 24) and to compare amplitude of the magnetic measurements with experimental values (option 25). The experimental value of the amplitude should be written in a file before calculations. It can be done using the "mtr" program (author M.Maraschek) existing on all Unix machines (Read data-> Calc.FFT-> Spectrum-> Back FFT and Save).

The second script ("sxr_vis") gives a possibility to read experimental data from the SXR and the ECE diagnostics on the ASDEX Upgrade and compare these date with MHD-IC simulations. The most important options are following:

- Calculation of the FFT transform for a simulated SXR signal (option 10)

[2]In order to start the MATLAB one should type in the command line:
>matlab
>addipplib

- Calculation of the FFT transform for an experimental SXR signal and comparison with the simulated one (option 8)
- Calculation of the SVD eigenvectors for the experimental SXR signal and comparison with the simulated one (option 7)
- Calculation of $\xi(\rho)$ and $\xi(R)$ from the experimental ECE signals and comparison with the simulated displacement (options 15,17)
- Plot of the FFT phase of the ECE signals (option 18)

Bibliography

[1] J. D. Lawson. *Proc. Roy. Soc. B*, 70:6, 1958.

[2] I.E.Tamm and A.D.Sakharov. In *Plasma Physics and the Problem of Controlled Thermonuclear Reactions Vol.1*, pages 1–47. Pergamon, Oxford, 1961.

[3] J. Wesson. *Tokamaks*. Clarendon Press - Oxford, 1997.

[4] D. Biskamp. *Nonlinear Magnetohydrodynamics*. Cambridge University Press, 1992.

[5] J. Freidberg. *Ideal Magnetohydrodynamics*. Plenum Press New York, 1987.

[6] K. Lerbingen and J. F. Luciani. A new semi-implicit method for MHD computations. *Journal of Computational Physics*, 97:444–459, 1991.

[7] H. Lütjens and J. F. Luciani. Stability thresholds for ballooning modes driven by high β internal kinks. *Phys. Plasmas*, 3:4192–4194, 1997.

[8] G. Bateman. *MHD Instabilities*. MIT Press, Cambridge, MA, 1978.

[9] A.I.Morozov and L.S.Solovev. The structure of magnetic fields. In *Reviews of Plasma Physics Vol.2*. Consultants Bureau New York, 1966.

[10] V.D.Shafranov. Plasma equillibrium in a magnetic field. In *Reviews of Plasma Physics Vol.2*. Consultants Bureau New York, 1966.

[11] R.D.Hazeltine and J.D.Meiss. *Plasma Confinement*. Addison-Wesley Publishing Company, 1992.

[12] W.M.Mancheimer and C.L.Davies. *MHD Instabilities in Simple Plasma Configuration*. Naval Research Laboratory, Washington, D.C., 1984.

[13] S. Mirnov and I. Semenov. Investigation of instabilities of plasma column in "Tokamak-3" device by correlation techniques. *At. Energ. (USSR)*, 30, 1971.

[14] O.Klüber, H.Zohm, H.Bruhns, J.Gernhardt, A.Kallenbach, and H.Zehrfeld. MHD mode structure and propagation in the ASDEX tokamak. *Nuclear Fusion*, 31:907–926, 1991.

[15] J.Kim, D.Edgell, J.Greene, E.Strait, and M.Chance. MHD mode identification of tokamak plasmas from Mirnov signals. *Plasma Phys. Contr. Fus.*, 41:1399–1420, 1999.

[16] M. Schittenhelm, H. Zohm, and ASDEX Upgrade team. Analysis of coupled MHD modes with mirnov probes in ASDEX Upgrade. *Nucl. Fusion*, 37:1255–1270, 1997.

[17] V. Pustovitov. Magnetic diagnostics: General principles and the problem of reconstruction of plasma current and pressure profiles in toroidal system. *Nuclear Fusion*, 41(6):721, 2001.

[18] S. Goeler, W. Stodiek, and N. Sauthoff. *Phys. Rev. Letts.*, 33:1201, 1974.

[19] M.Bessenrodt-Weberpals, J.Fuchs, M.Sokoll, and ASDEX Upgrade Team. Soft X-Ray Diagnostics for ASDEX Upgrade. Report IPP 1/290, Max-Planck-Institut für Plasmaphysik, Garching bei München, August 1995.

[20] M. Sokoll. MHD-instabilitäten in magnetisch eingeschlossen plasmen und ihre tomographische rekonstruktion im röntgenlicht. Report IPP 1/309, Max-Planck-Institut für Plasmaphysik, Garching bei München, April 1997.

[21] M.Bessenrodt-Weberpals, H. de Blank, M. Maraschek, P. McCarthy, M. Sokoll, K. Asmussen, and ASDEX Upgrade Team. MHD activity as seen in soft X-ray radiation. *Plasma Phys. Control. Fusion*, 38:1543–1559, 1996.

[22] R.S.Granetz and P.Smeulders. X-ray tomography on JET. *Nuclear Fusion*, 28:457, 1988.

[23] M. Bornatici, R. Cano, O. de Barbieri, and F. Engelmann. *Nuclear Fusion*, 23:1153, 1983.

[24] W.Suttrop and A.G.Peeters. Practical limitations to plasma edge electron temperature measurements by radiometry of electron cyclotron emission. IPP Report 1/306, 1997.

[25] R.C.Wolf et al. Motional stark effect polarimetry for the determination of the ASDEX Upgrade current density profile. In *Abst. 24 EPS*, page 460, 1997.

[26] R.Wolf. MSE diagnostic (ASDEX Upgrade Database).

[27] W.Schneider, P.McCarthy, K.Lackner, O.Gruber, K.Behler, P.Martin, and R.Merkel. ASDEX Upgrade MHD Equilibria Reconstruction on Distributed Workstations. *Fusion Engineering and Design*, 48:127–134, 2000.

[28] P.J.Mc Carthy, R.C. Wolf, J. Hobirk, H. Meister, and W.Schneider. Current profile identification on ASDEX Upgrade via motional stark effect and the CLISTE interpretive equilibrium code. In *27th EPS Conf, Budapest, Europhysics Conference Abstract*, volume 24B, pages 440–443, 12-16 June 2000.

[29] W. Kerner, J. Goedbloed, G. Huysmans, S. Poedts, and E. Schwarz. CASTOR: Normal-mode analysis of resistive MHD plasmas. *J. Comp. Phys.*, 142:271–303, 1998.

[30] H. Lütjens, A. Bondeson, and A. Roy. Axisymmetric MHD equilibrium solver with bicubic hermite elements. *Comput. Phys. Comm.*, 69:287–298, 1992.

[31] P.M.Carthy, R.Wolf, J.Hobirk, H.Meister, and W.Schneider. Current profile identification on ASDEX Upgrade via Motional Stark Effect and the CLISHTE interpretive equilibrium code. In *Abst. 27th EPS 2000*, pages 440–443, 2000.

[32] M. Schittenhelm. Investigation of tearing modes in asymmetric elongated plasmas in the ASDEX Upgrade tokamak. Report IPP 1/289, Max-Planck-Institut für Plasmaphysik, Garching bei München, Juni 1995.

[33] R. Bank. *PLTMG: A Software Package for Solving Elliptic Partial Differential Equation*. Society for Industrial and Applied Mathematics, Philadelphia, 1990.

[34] W.D.D'haeseleer, W.N.G.Hitchon, J.D.Callen, and J.L.Shohet. *Flux Coordinates and Magnetic Field Structure (A Gide to a Fundamental Tool of Plasma Theory)*. Springer-Verlag, 1991.

[35] Q.Yu. Private communications (numerical simulations of tearing modes in cylindrical geometry).

[36] I.H. Hutchinson. *Principles of Plasma Diagnostics*. Cambridge University Press, 1987.

[37] R. Fitzpatrick. Helical temperature perturbations associated with tearing modes in tokamak plasmas. *Phys. Plasmas*, 2:825–838, 1995.

[38] G.A.Korn and T.M.Korn. *Mathematical handbook for scientists and engineers*. McGraw Hill Book Company, INC, 1961.

[39] R. Schaback and H. Werner. *Numerische Mathematik*. Berlin: Springer, 1992.

[40] J. Dongarra, J. Bunch, C. Moler, and G. Stewart. *LINPACK Users' Guide*. SIAM, Philadelphia, 1979.

[41] D. Belsley. *Conditional Diagnostics: Collinearity and Weak Data in Regression*. John Wiley and Sons, 1989.

[42] P.Franz, L.Marrellia, A.Murari, G.Spizzo, and P.Martin. Soft X ray tomographic imaging in the RFX reversed field pinch. *Nuclear Fusion*, 41:695, 2001.

[43] M. Anton et al. X-ray tomography on TCV tokamak. *Plasma Phys. Control. Fusion*, 38:1849, 1996.

[44] M. Sokoll. Interpretation and tomography of SXR data with the codes VISO and DIRO. Report IPP 1/310, Max-Planck-Institut für Plasmaphysik, Garching bei München, July 1997.

[45] G.Fuchs, Y.Miura, and M.Mori. Soft x-ray tomography on tokamaks using flux coordinates. *Plasma Phys. Control. Fusion*, 36:307, 1994.

[46] A. Oomens. Advanced tokamak concepts. *Transacions of fusion technology*, page 385, 1998.

[47] A.G.Peeters. The bootstrap current and its consequences. *Plasma Phys. Control. Fusion*, 42:B231, 2000.

[48] E.J.Strait et al. Enhanced Confinement and Stability in DIII-D Discharges with Reversed Magnetic Shear. *Phys. Rev. Let.*, 75(24):4421, 1995.

[49] F. Levinton et al. Improved confinement with reversed magnetic shear in TFTR. *Physical Review Letters*, 75:4417–4420, 1995.

[50] J.M.Greene and M.S.Chance. *Nuclear Fusion*, 21:453, 1981.

[51] B. W. Rice et al. Demonstration of high-performance negative central magnetic shear discharges in the DIII-D tokamak. *Phys. Plasmas*, 3(5):1983, May 1996.

[52] T. Fujita et al. Quasisteady high-confinement reversed shear plasma with large bootstrap current fraction under full noninductive current drive condition in JT-60U. *Physical Review Letters*, 87(8):8501, August 2001.

[53] C.M.Greenfield et al. Quiescent double barrier regime in the DIII-D tokamak. *Physical Review Letters*, 86(20):4544, May 2001.

[54] O.Gruber, R.Wolf, H.Bosch, S.Günter, P.McCarthy, K.Lackner, M.Maraschek, H.Meister, G.Pereverzev, A.Stäbler, W.Treutterer, and ASDEX Upgrade Team. Steady state H mode and $T_e \approx T_i$ operation with internal transport barriers in ASDEX Upgrade. *Nuclear Fusion*, 40(6):1145–1155, 2000.

[55] S. Günter et al. Simultaneous attainment of high electron and ion temperatures in discharges with internal transport barriers in ASDEX Upgrade. *Physical Review Letters*, 84(14):3097, April 2000.

[56] E.Joffrin et al. q=1 advanced tokamak experiments in JET and comparison with ASDEX Upgrade. *Plasma Phys. Control. Fusion*, 44:1203, 2002.

[57] S. Günter, S. Schade, M. Maraschek, S. Pinches, E. Strumberger, R. Wolf, Q. Yu, and ASDEX Upgrade team. MHD phenomena in reversed shear discharges on ASDEX Upgrade. *Nuclear Fusion*, 40:1541–1548, 2000.

[58] T. Kass, H.-S. Bosch, F. Hoenen, K. Lackner, M. Maraschek, H. Zohm, and ASDEX Upgrade team. The fishbone instability in ASDEX Upgrade. *Nuclear Fusion*, 38:807–819, 1998.

[59] S. Günter, A. Gude, K. Lackner, M. Maraschek, S. Pinches, S. Sesnic, R. Wolf, and ASDEX Upgrade team. Influence of fishbones on the background plasma. *Nuclear Fusion*, 39:1535–1539, 1999.

[60] M. Rosenbluth, R. Dagazian, and P. Rutherford. Nonlinear properties of the internal $m = 1$ kink instability in the cylindrical tokamak. *Phys. Fluids*, 16:1894–1902, 1973.

[61] M. Rosenbluth, D. Monticello, H. Strauss, and R. White. Numerical studies of nonlinear evolution of kink modes in tokamaks. *Phys. Fluids*, 19:1987–1996, 1976.

[62] H. de Blank and T. Schep. Theory of $m = 1$ kink mode in toroidal plasma. *Phys. Fluids B*, 3:1136–1151, 1991.

[63] R.Betti and J.P.Freidberg. Destabilization of the internal kink by energetic circulating ions. *Physical Review Letters*, 70(22):3428, May 1993.

[64] Shaojie Wang. Destabilization of internal kink modes at high frequency by energetic circulating ions. *Physical Review Letters*, 86:5286, June 2001.

[65] W.Heidbrink and G.Sageer. The fishbone instability in the DIII-D tokamak. *Nuclear Fusion*, page 1015, 1990.

[66] L.Chen, R.White, and M.Rosenbluth. Excitation of internal kink modes by trapped energetic beam ions. *Phis.Rev.Lett.*, 52(13):1122, March 1984.

[67] M.F.Nave, D.J.Campbell, E.Joffrin, F.B.Marcus, G.Sadler, P.Smeulders, and K.Thomsen. Fishbone activity in JET. *Nuclear Fusion*, 31(4):697, 1991.

[68] P. L. Pritchett, Y. C. Lee, and J. F. Drake. Linear analysis of the double-tearing mode. *Phys. Fluids*, 23:1368–1374, 1980.

[69] L. Ofman. Double tearing instability with shear flow. *Phys. Fluids B*, 4:2751–2757, 1992.

[70] M. Persson, R. L. Dewar, and E. K. Maschke. Nonlinear self-reinforced growth of tearing modes with multiple rational surfaces. *Phys. Fluids B*, 5:3844–3846, 1993.

[71] Q.Yu. Nonlinear evolution of neoclassical double tearing mode. *Physics of Plasma*, 4:1047, April 1997.

[72] Q. Yu and S. Günter. Numerical modelling of neoclassical double tearing modes. *Nucl. Fusion*, 39:487–494, 1999.

[73] Y.Ishii, M.Azumi, G.Kurita, and T.Tuda. Nonlinear evolution of double tearing modes. *Physics of Plasmas*, 7(11):4477, 2000.

[74] S. Günter, A. Gude, J. Hobirk, M. Maraschek, S. Saarlema, S. Schade, R. Wolf, and ASDEX Upgrade team. MHD phenomena in advanced scenarios on ASDEX Upgrade and the influence of localized electron heating and current drive. *Nuclear Fusion*, 41:1283–1290, 2001.

[75] R.B.White, D.A.Monticello, M.N.Rosenbluth, and B.V.Waddell. *Phys. Fluids*, 20:800, 1977.

[76] R.White. *Theory of Tokamak Plasmas.* North-Holland, 1989.

[77] E.Fredrickson, M.Bell, R.V.Budny, and E.Synakowski. Nonlinear evolution of double tearing modes in tokamaks. *Physics of Plasmas*, 7:4112, October 2000.

[78] E.Strumberger, H.Zehrfeld, and S.Günter. Stability studies of ideal plasma flow equilibria. In *28th EPS Conf. Madeira*, 2001.

[79] H.P.Zehrfeld. Resistive equilibrium states of axisymmetric plasmas with compressible viscous fluid flow. In *26th EPS Conference on Controlled Fusion*, 1999.

[80] S. Günter et al. MHD phenomena as trigger for the formation of internal transport barriers on ASDEX Upgrade. In *EPS 2001*, page 20, 2001. (Submitted to Nuclear Fusion).

[81] F.C.Schüller. Disruptions in tokamaks. *Plasma Phys. Control. Fusion*, 37:A135, 1995.

[82] J.A.Wesson et. al. Disruption in JET. *Nuclear Fusion*, 29(4):641–666, 1989.

[83] G.T.Huysmans et al. MHD stability of optimized shear discharges in JET. *Nuclear Fusion*, 39(11):1489–1507, 1999.

[84] M.Greenwald. Density limits in toroidal plasmas. *Plasma Phys. Control. Fusion*, 44:R27, 2002.

[85] H.Zohm et al. MHD Stability and Disruption Physics in ASDEX Upgrade. *Plasma Phys. Control. Fusion*, 37:A313, 1995.

[86] E.J.Strait et al. In *Controlled Fusion and Plasma Physics, Proc. 18th Eur. Physical Society Conf. (Berlin)*, page 105, 1991. vol 15C, part II.

[87] S.Itoh, K.Itoh, H.Zushi, and A.Fukuyama. Physics of collapse events in toroidal plasmas. *Plasma Phys. Control. Fusion*, 40:879, 1998.

[88] J.D.Callen, C.C.Hegna, B.W.Rice, E.J.Strait, and A.D.Turnbull. Growth of ideal magnetohydrodynamic modes driven slowly through their instability threshold: Application to disruption precursor. *Physics of Plasmas*, 6(8):2963, 1999.

[89] G.T.A. Huysmans. External resistive modes in tokamaks, 1991. Ph.D.thesis, Vrije University of Amsterdam.

[90] M. Rosenbluth and R. Sagdeev. *Handbook of Plasma Physics*, volume 1. North-Holland Publishing Company, 1983.

[91] M.Bessenrodt-Weberpals, H. de Blank, P. McCarthy, M. Sokoll, K. Asmussen, ASDEX Upgrade Team, and NI Team. Analysis of rotating $(n = 1, m = 1)$ modes as seen in soft X-ray radiation and its application to current profile identification. In *EPS95*, page 133, 1995.

[92] I.S.Gradshteyn and Y.U.Ryzhik. *Table of Integrals, Series, and Products*. ACADEMIC PRESS New York and London, 1965.

[93] H. P. Furth, P. H. Rutherford, and H. Selberg. Tearing mode in the cylindrical tokamak. *Phys. Fluids*, 16:1054–1063, 1973.

[94] D.Biskamp. Nonlinear behavior of tearing modes, January 1980. IPP 6/192.

[95] Nonlinear MHD simulations of tearing modes performed by the author with XTOR code in 2000-2002.

[96] W.Kerner. Large-scale complex eigenvalue problems. *J.Comp.Phys.*, 85:1, 1989.

[97] E. Strumberger. Description of the CASTOR code (notes).

[98] H.Lütjens, J.Luciani, and X.Garbet. Nonlinear three-dimensional MHD simulations of tearing modes in tokamak plasmas. *Plasma Phys. Control. Fusion*, 43:A339, 2000.

[99] H. Lütjens, A. Bondeson, and O. Sauter. The CHEASE code for toroidal MHD equilibria. *Computer Physics Communications*, 97:219–260, 1996.

[100] R. Arslanbekov. *CHEASE and XTOR User Manual*. Personal notes (IPP), 2000.

Appendix E

List of abbreviations

ASDEX	**A**xial **S**ymmetric **D**ivertor **EX**periment
DTM	**D**ouble **T**earing **M**ode
ECE	**E**lectron **C**yclotron **E**mission
FFT	**F**ast **F**ourier **T**ransformation
ITB	**I**nternal **T**ransport **B**arrier
MHD	**M**agneto-**h**ydro-**d**ynamics
MHD-IC	**MHD I**nterpretation **C**ode
MSE	**M**otional **S**tark **E**ffect
NBI	**N**eutral **B**eam **I**njection
SVD	**S**ingular **V**alue **D**ecomposition
SXR	**S**oft **X**-**r**ay

Acknowledgements

Fist of all I would like to thank Prof. Dr. S. Günter, Head of the Tokamak Division, for the opportunity to make this work under her supervision. I learned a lot from her during my work. I thank her for the permanent support of this work and for our discussions which help me much better understand the plasma physics.

I thank Dr. M.Maraschek for help with the MIC code which was the starting point of my research and for his friendly support during all this time.

I express my gratitude to Prof. Dr. R.Wilhelm, Head of the Technology Division, who also supervised me scientifically in Technical University of Munich.

Especially, I thank Dr. R.Arslanbekov, Dr. H.-P.Zehrfeld, Dr. E.Strumberger for their help with computational simulations using XTOR, DIVA, HELENA and CASTOR codes. Their advices and support allowed me efficiently use these MHD codes.

I thank Dr. J.Hobrik and D.Merkl for the MSE measurements and equilibrium reconstructions based on these measurements which were used in my calculations.

I thank Dr. P.McCarthy and Dr. P.Martin. They helped me to install and use equilibrium code CLISTE which allows to construct equilibrium reconstructions of the experiments.

Also, I thank Prof. Dr. H.Zohm, Head of the Experimental Division II, Dr. W.Suttrop, Dr. S.Sesnic, A.Mück, A.Keller for their work with the ECE and SXR diagnostics and their interest in my results. Experimental data from these diagnostics were intensively used in my code as the main source of experimental information about MHD instabilities.

I thank Dr.W.Schneider for his answers to my questions about equilibrium database and Dr.A.Peeters for his advices and help with ITB discharges.

In addition, I thank Dr. S.Pinches, Dr. G.Pautasso, Dr. C.V.Atanasiu, R.Kochergov, V.Bobkov, S.Riondato, P.Lauber, E.Quigley and especially Dr. Q.Yu for their help and discussions on all physical questions.

During my PhD project I worked together with many people from the ASDEX Upgrade tokamak in Max-Planck-Institute of Plasma Physics and I would like to thank all of them for their friendship and help during all this time. It was a pleasure for me to work on ASDEX Upgrade tokamak.